CHARACTERIZATION OF ENGINEERED COMPLEX CATHODE MATERIALS FOR LI-ION BATTERIES

Characterization of Engineered Complex Cathode Materials for Li-ion Batteries

By

NAFISEH ZAKER, BSc., MSc.

A Thesis

Submitted to the School of Graduate Studies in Partial Fulfillment of the Requirements

for the Degree Doctor of Philosophy

McMaster University

DOCTOR OF PHILOSOPHY (2023) McMaster University

(Materials Science and Engineering) Hamilton, Ontario

TITLE: Characterization of Engineered Complex Cathode Materials for Li-ion Batteries

AUTHOR: Nafiseh Zaker

B.Sc. in Materials Science and Engineering (Iran University of Science and Technology)

M.Sc. in Materials Science and Engineering (Sharif University of Technology)

SUPERVISOR: Dr. G. A. Botton

NUMBER OF PAGES: xviii, 164

Abstract

Lithium-ion batteries have become a vital part of our modern life and are anticipated to play an essential role in substituting combustion engines in automotive applications and storing renewable energy sources, thus leading to a more sustainable future for the planet. The impact of this technology was highlighted in 2019 when the Nobel Prize in chemistry was given for the development of Li-ion batteries. Although several milestones have been achieved in terms of Li-ion battery development throughout the years, in-depth studies are still required to either modify the existing materials or introduce new materials in order to overcome the limitations in capacity, durability, cost, and safety of such materials. The main components in Li-ion batteries are categorized into cathode, anode, electrolyte, and membrane, which can all affect the batteries' performance in the matter of power and energy density. Studying cathode structures and understanding their internal reactions are particularly important since this component dictates the cost and constraints of the energy density in the Li-ion batteries.

One of the most feasible strategies to enhance the energy density of Li-ion batteries is to use layered, Ni-rich cathode materials. Higher nickel content, however, causes several problems in terms of cyclic life, thermal stability, and safety which should be properly addressed. Several methods, including doping, core-shell structures, and coating, have been utilized to stabilize (chemically and mechanically) the high-nickel layered oxide cathodes and boost their performance. This thesis aims to understand the microstructure of such engineered complex cathode materials. This thesis seeks to provide valuable contributions by comprehensively understanding, especially two enhancement techniques,

namely doping and solid-state coating, and establishing a link between the composition, structure, performance, and properties of these complex materials.

In this regard, this project aims to characterize these engineered complex materials using the most advanced electron microscopy and synchrotron-based techniques to uncover the fundamental underlying reasons for the enhanced performance or degradation parameters in these complex cathode structures. This study shows that introducing a high valence W cation inside the $LiNiO_2$ (LNO) secondary particles results in new W-variants with a heterogeneous concentration on the top surface as well as through grain boundaries of the host secondary particles. These W-rich regions play a reinforcing role in grain boundaries and protect the outer surface of LNO particles. However, synthesis defects, such as porosities, could deteriorate these advantages by increasing the electrolyte infiltration inside the cathode particles. It is also demonstrated that the degradation process can be studied through the changes in electron energy loss near-edge structure spectra. The investigation of a coating approach on $LiNi_{0.8}Co_{0.15}Al_{0.05}O_2$ (NCA) materials through the mechanofusion process illustrates more microscopic-scale details regarding the thickness unevenness of the coating and some degree of physical intermixing between the core (NCA) and coating (LFP and alumina) precursors. In addition to good physical contact between the core and coating materials, further analysis at higher resolution reveals some level of structural alternations through the formation of nanoscale grains and defective areas near the top surface of the secondary particles following the mechanofusion coating process.

To

My parents, Nahid and Mahmoud

I owe you everything

The love of my life, Ali

&

All the brave Iranian women fighting for their freedom

Acknowledgments

First and foremost, l would like to express my most profound appreciation to my mentor and supervisor, Prof. Gianluigi Botton, for his endless support and guidance with his immense knowledge, through all the ups and downs in my Ph.D. journey. I will always be honored to be one of his students and study under his supervision. I consider myself beyond fortunate to have such a patient, kind, humble and erudite supervisor.

I would like to extend my sincere thanks to my supervisory committee members, Prof. Gillian Goward and Prof. Joseph Kish, for their insightful and encouraging guidance and discussions throughout all these years. This research would not have been possible without their support. I am incredibly grateful for collaborating with Prof. Jeff Dahn and his professional group, who provided all the samples for this project. I am also thankful for our helpful meetings and discussions with Dr. Jim Britten.

I consider myself lucky to have extensive experience and be trained in very high-tech instruments, from various electron microscopies in CCEM to synchrotron-based techniques at CLS. I am deeply indebted to the staff members who trained me, generously supported me, and helped me with my project. Many thanks to Dr. Natalie Hamada, Travis Casagrande, Dr. Hui Yuan, Dr. Carmen Andrei, Chris Butcher, Jhoynner Martinez, Dr. Brian Langelier, Dr. Samantha Stambula, and Andy Duft from CCEM. I am also grateful for Dr. Beatriz Diaz Moreno, Dr. Jeol Reid, Dr. Graham King, Dr. Adam Leontowich, and Dr. Al Rahemtulla from CLS. Special thanks to Dr. Ning Chen for his enormous help and open-handedly support.

I am fortunate to have such kind and supportive colleagues in Botton's group at McMaster University. Thank you for making such a pleasant and memorable time in our Teatimes, lecture rehearsals, and scientific discussions. I am grateful to our senior group members, Dr. Alex Pofelski and Dr. Isobel Bicket, for their technical and emotional support. Many thanks to my battery-buddy Jingyi Qu, Milenka Andelic, Shayan Mousavi, Peter Neathway, and my former colleagues Dr. Hanshuo Liu, Amin Hashemi, Viktor Kapetanovic, Eric Daigle, and all the present and past members of A406 office.

In the end, l wanted to express my innermost gratitude to my dear family, especially my parents, my in-laws, my dearest sister Narges, my beloved brother-in-law Sepehr and my lovely auntie Elaheh, so close yet so far, for their unconditional loves and spiritual supports who always motivate me through this Ph.D. path. Lastly, the most important person in my life, my better half, my dear friend, and my husband, soon to be Dr. Ali; without him, l could not have undertaken this journey. I am always indebted to my family, and words can not express my deep appreciation.

Contents

Page

List of Figures

List of Tables

Chapter 1

Introduction

1.1 Lithium-ion battery

A battery is an instrument that is used in order to either generate or restore electric energy based on its energy converting capabilities through electrochemical reactions. Since the battery's work is based on electrochemical reactions, it is not limited by the Carnot cycle, determined by thermodynamics' second law. Therefore, they can reach higher efficiencies in terms of energy conversion [1]. To classify and compare different battery technologies, several characteristic terms should be considered, which are listed as follows:

- ✓ The volumetric power density and specific power density (the gravimetric power density) define how quickly that energy can be provided. Having higher values regarding these parameters denotes the presence of lower amounts of electric resistances and energy losses.
- ✓ The volumetric energy density and gravimetric energy density (the specific energy density), describe the total energy that can be obtained from the battery.
- ✓ Energy efficiency is a parameter that can be described as the ratio of the discharging to charging energy.
- ✓ The calendar lifetime is used to define the life span of non-used or very marginally used batteries until their failure.
- ✓ The cyclic lifetime, unlike the previous one, illustrates the number of cycles that a battery can tolerate before its failure, which depends on the C-rate, depth of discharge (DOD), and the average of the state of charge (SOC). It is worth mentioning that C-rate is a parameter that defines how fast the entire capacity of the battery will be discharged or charged in

comparison with its maximum capacity and its value is inversely proportional to time.

In order to compare the performance of different energy storage devices, a Ragone plot is used. In this plot, as illustrated in Figure 1-1 for different battery technologies, the specific energy (Wh/kg) and the specific power (W/kg) are displayed in the horizontal and vertical axis, respectively. It is noteworthy that the practical value of specific energy density is considered about 25–50% of the theoretical amount, which is computed from the electrochemical reaction [2].

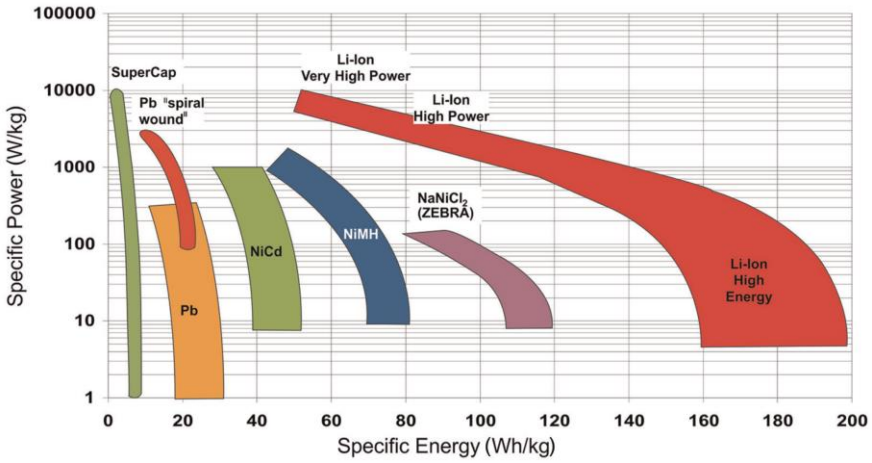

Figure 1-1 Ragone plot of several battery systems which are used for the vehicle industry. SuperCap, Pb, and ZEBRA mean supercapacitor, lead, and Zero Emission Battery Research Activities, respectively [2]. Reused with permission from the copyright owner.

According to the Ragone plot, Li-ion batteries (LIBs) have proven to be one of the most proper candidates for vehicle applications because of their high amount of specific energy as well as their long cyclic life [3,4].

Lithium-ion batteries can be categorized into two main groups: primary (single-use) and secondary (rechargeable). A rechargeable Li-ion battery has four main components:

cathode, anode, electrolyte, and electrolyte-permeable separator. Besides the similarities between traditional galvanic cells and LIBs, battery scientists should deal with more complex heterogeneous redox reactions inside LIBs. Since these reactions are usually complemented by mass diffusion in the solid-state or alterations in the local structure, chemical composition, and volume (contraction or expansion) in the electrodes [5,6]. Figure 1-2 shows schematics of Li-ion battery configuration. As is apparent, during the charging process, Li ions are extracted from the cathode (delithiation) and then inserted into the anode, and during the discharging procedure, the reverse reaction occurs.

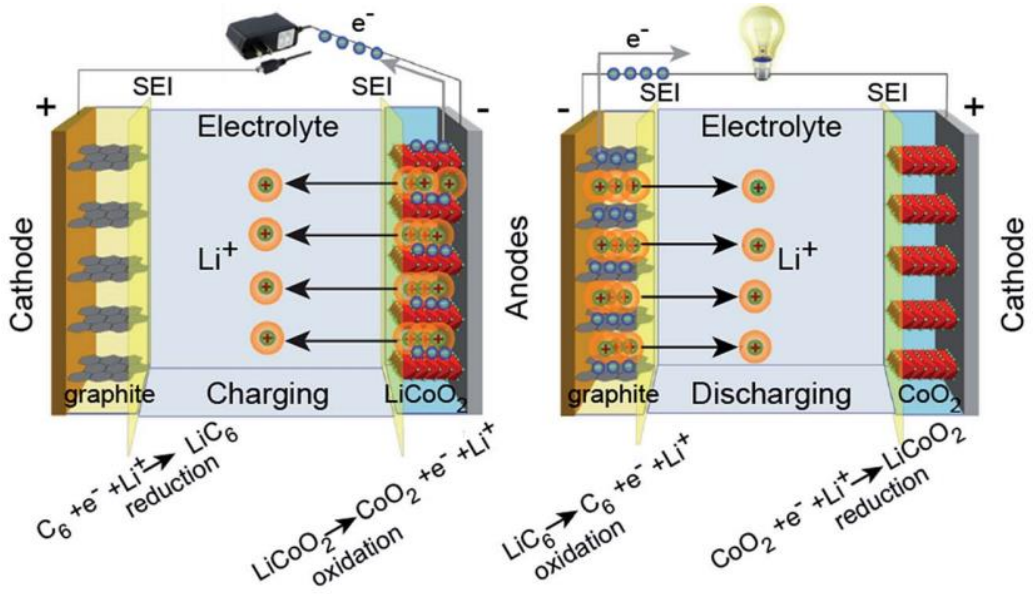

Figure 1-2 Schematic of charging and discharging procedure in the first commercial Li-ion battery (with $LiCoO_2$ as the cathode and graphite as the anode) [7]. Reused with permission from the copyright owner.

The charging reaction can be described as follows:

$$LiMO_2 \rightarrow Li^+ + e^- + MO_2 \qquad \text{(cathode)}$$

$$Li^+ + e^- + C_6 \rightarrow LiC_6 \qquad \text{(anode)}$$

By using thermodynamic approaches, some of the most significant performance parameters of a battery can be calculated. One of the most important terms to estimate the energy density of the batteries is the operating voltage or the open-circuit voltage (OCV). This parameter comes from the voltage differences in-between the cathode and anode of a battery and can be calculated according to the different amounts of the electrochemical potential of electrons in the anode ($\eta_{e^-}^{anode}$) and cathode ($\eta_{e^-}^{cathode}$):

$$V = -\frac{\eta_{e^-}^{cathode} - \eta_{e^-}^{anode}}{e} \quad (1.1)$$

By inserting the chemical potential of Li in the anode and cathode, $\mu_{Li}^{X} = \eta_{e^-}^{X} + \eta_{Li^+}^{X}$, in which X = anode and cathode, respectively, the following equation is obtained:

$$V = -\frac{(\mu_{Li}^{cathode} - \mu_{Li}^{anode}) - (\eta_{Li^+}^{cathode} - \eta_{Li^+}^{anode})}{e} \quad (1.2)$$

Here, $\eta_{Li^+}^{cathode}$ and $\eta_{Li^+}^{anode}$ represent the Li-ion electrochemical potentials in the electrodes. Since, at equilibrium, these two parameters are equal, the voltage equation is simplified as follows:

$$V = -\frac{(\mu_{Li}^{cathode} - \mu_{Li}^{anode})}{zF} \quad (1.3)$$

Where F stands for the Faraday constant, and z signifies the number of transferred charges. By considering the alternation in the Gibbs free energy of the cathode and anode materials as a function of Li-ion concentration, $\mu_{Li} = \frac{dG}{dN_{Li}}$, and Nernst equation, the average voltage can be calculated based on changes in Gibbs free energy in a limited amount of cathode and anode reactions [8]:

$$\bar{V} = -\frac{\Delta G_r}{zF} \quad (1.4)$$

The OCV is restricted by the electrolyte energy "window" (E_g), which is the energy difference in-between LUMO and HOMO (lowest unoccupied molecular orbitals and highest occupied molecular orbitals) of a liquid electrolyte or the gap of energy between the top and bottom level of valence and conduction bands, respectively, inside a solid electrolyte, as illustrated in Figure 1-3(a). Accordingly, the formation of a passivation layer (SEI) in both the anode and cathode is necessary to prevent electrolyte reduction and oxidation, respectively. This is due to the fact that the locations of μ_A and μ_C are above and below the electrolyte LUMO and HOMO, respectively. In other words, the electrolyte will be stable if only its LUMO and HOMO are placed higher and lower than the anode's and cathode's Fermi energy levels, correspondingly [9]. It should be considered that the lowest level of μ_C is limited by the top anion-p bands energy level in the cathode as well.

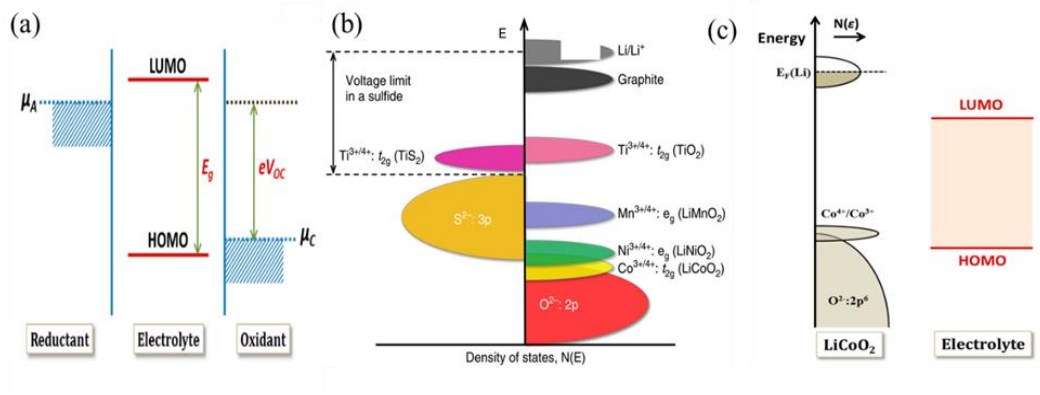

Figure 1-3 Relative electronic energy levels of the LIB's components along with the electrolyte window Eg: (a) in a liquid-based electrolyte; (b) Relative locations of the redox energies concerning the top energy level of the anion's p bands and (c) relative energy level places of μ_A (Li as the anode) and μ_C ($LiCoO_2$ as the cathode) inside a carbonate-based electrolyte [10,11]. Reused with permission from the copyright owners.

As it is illustrated in Figure 1-3(b), the difference between the top energy level of the anion-p band and the Li anode's μ_A, inside the sulfide-based cathode materials (the layered

sulfides $LiMS_2$ with S-3p bands) is much lower than in the layered oxides ($LiMO_2$ with O-2p bands) and is about ~2.5 eV and ~4.0 eV, respectively. This was the primary idea which led to the use of oxide host structures instead of sulfide-based cathodes, aiming to increase the cell voltage and the energy density. In a practical situation, Figure 1-3(c), when the top energy level of the O-2p bands is lower than the organic liquid carbonate electrolyte's HOMO (4.3 eV lower than the Li anode's μ_A), oxygen is released or proton insertions will occur during the delithiation of the cathode $Li_{1-x}CoO_2$ (more than x = 0.5) [10,11].

1.2 Overpotentials in Lithium-Ion Batteries

During the charging and discharging procedure, by applying a current inside the LIB, the equilibrium voltage or open cell voltage is changed due to the battery's diffusion or electronic and ionic resistance, which is called the cell overpotential η. The value of this parameter can be measured by considering the main causes of overpotentials (some of them are shown in Figure 1-4), such as the contact resistance (according to the resistance of electrodes at the current collector interface), the ohmic overpotential (which results from the electronic conductivity of the electrodes and current collector as well as the electrolyte ionic conductivity), the diffusion overpotential (defined by lithium-ion intercalation process or diffusion, particularly near the electrode interface with the electrolyte and the solid-state diffusion in the electrode structures) and the charge transfer overpotential (owing to the amount of required activation energy to transfer charge in between the electrodes and electrolyte) [12]. The following equation describes the effect of all the overpotentials components:

$$\eta = \eta_{contact} + \eta_{ohmic} + \eta_{diff} + \eta_{ct} \quad (1.5)$$

By considering equation (1.5), the closed-circuit voltage (CCV) of the LIBs can be calculated below, in which the q symbolizes the state of charge [10].

$$V_{discharge} = V_{oc} - \eta(q, I_{discharge}) \quad (1.6)$$

$$V_{charge} = V_{oc} + \eta(q, I_{charge}) \quad (1.7)$$

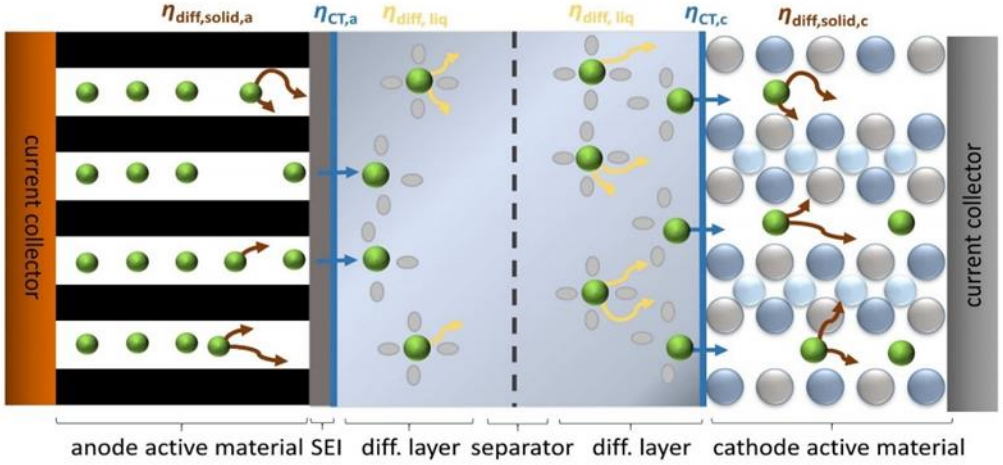

Figure 1-4 Representation of the main overpotential parameters in a lithium-ion battery which are responsible for nonlinear behavior of I and η [12]. Reused with permission from the copyright owner.

It is worth noting that the relationship between I (current) and η is approximately linear at low current ranges and then becomes nonlinear by further increasing the current to moderate and higher levels. The linear part is mostly caused by the contact and the ohmic overpotential, while the diffusion and charge transfer processes contribute to the appearance of the nonlinear region. These limitations which are caused by kinetics, reduce the theoretical value of specific energy (based on thermodynamic calculations) via increasing V_{charge} or lowering $V_{discharge,}$ which sequentially decreases the specific capacity [13].

1.3 Cathode materials for Li-ion batteries

The cathode is one of the crucial components inside the lithium-ion cell, which limits the cell's specific energy and dictates the material cost, leading to extensive research regarding its structure and internal reactions. As mentioned earlier, choosing the oxide cathodes over the sulfide ones paves the way to reach the lower level of energy bands of the cathode, accompanied by higher oxidation states of transition-metal ions, which all help to enhance cell voltage and energy density. The oxide cathodes can be classified into three main crystallographic structure groups: layered oxides, spinel oxides, and olivine or polyanion oxides [11]. Recently, a new tavorite structure was synthesized, which has low activation energies and a one-dimensional diffusion pathway for Li^+ that improve the fast charging of this material compared to the tiny olivine particles [14,15]. Figure 1-5 depicts a schematic view of these four different crystal structures.

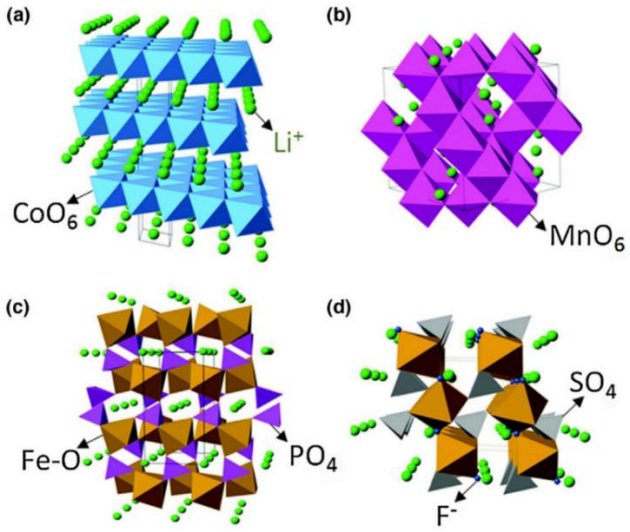

Figure 1-5 Schematic structure of (a) layered oxide ($LiCoO_2$), (b) spinel oxide ($LiMn_2O_4$), (c) polyanion oxide ($LiFePO_4$), and (d) tavorite ($LiFeSO_4F$) [14]. Reused with permission from the copyright owner.

The first category is the layered oxides ($LiMO_2$ (M= Co, Ni)), which is referred to as layered α-$NaFeO_2$ with $R\bar{3}m$ space group (No. 166), in which Li and Transition Metal (TM) ions are in the octahedral sites. This structure has stacking layers with an ABCABC sequence and oxygen anions in close-packed cubic positioning. This structure offers two-dimensional diffusion paths for Li-ion by passing through an empty neighboring tetrahedral in-between two octahedral sites (O-T-O). $LiCoO_2$ is the first oxide cathode that became commercial consisting of the trivalent Co^{3+} ions with a low-spin electronic configuration state of $t_{2g}^6\ e_g^0$ and the monovalent Li^+. During the charging process, metallic properties are observed in the cathode ($Li_{1-x}CoO_2$), because of having holes in the low-spin band (t_{2g}^{6-x}) of Co with a higher oxidation level ($Co^{3+/4+}$). Nevertheless, because of the overlap between the top level of the 2p band in the oxygen anion and the $Co^{3+/4+}$ band, the LCO structure will be unstable over 50% charging, accompanied by oxygen release. To solve this problem, different transition metals were examined, but some of them, such as Fe, Mn, and V experienced structural transformations through cycling [11,14,16].

$LiNiO_2$ (LNO) is another layered oxide with the same structure as LCO and a lower price due to the higher availability of Ni in comparison with Co, which offers a high theoretical capacity of 275 $mAhg^{-1}$. LNO shows repetitive structural changes (Hexagonal 1 → Monoclinic → Hexagonal 2 → Hexagonal 3 in charging) during the cycling. However, this material has a few shortcomings as follows: (1) its difficult synthesis to fully reach trivalent nickel ions (because of the Ni^{3+} instability at high temperatures and its tendency to reduce to Ni^{2+}); (2) the presence of cation mixing in the lithium plane as a result of the radial size similarity between Li^+ and Ni^{2+} ions; (3) Jahn-Teller distortion due to the presence of the single e_g electron in the low spin of trivalent Ni ion with an electronic configuration of d^7 equal to $t_{2g}^6\ e_g^1$; (4) converting into irreversible phase evolutions (from layered structure to

electrochemical inactive Fm(-)3m phase) triggered by diffusing enough Ni in the Li layers, during cycling; (5) the high-temperature instability and safety hazards due to the presence of residual Ni^{4+} at the surface at the end of charging [11,16–18].

Substituting Co with Ni and Mn, to reduce the cost and overcome the capacity limitation of LCO, introduced another family group of layered oxides under the name of $LiNi_{1-y-z}Mn_yCo_zO_2$ (NMC). In this structure, each TM ion comes with some pros and cons. For example, from the chemical stability point of view, which triggers releasing of oxygen, Mn is much more stable than Co due to not having any overlap between the $Mn^{3+/4+}$ band and the 2p band of oxygen anion. Still, Mn shows more structural instability than Co, because of having a smaller amount of octahedral-site stabilization energy (OSSE), which eases the TM ion's diffusion from one octahedral site to the next lithium octahedral sites by hopping through adjacent tetrahedral sites. Since Ni showed average properties in five major criteria (electrical conductivity, structural stability, abundance, chemical stability, and environmental friendliness) in comparison with Co and Mn, the tendency to use a higher amount of Ni has gradually increased in the industry [11,19].

Another well-known layered structure is $LiNi_{1-x-y}Co_xAl_yO_2$ (NCA), which shows long-term calendar life and high capacity due to the introduction of Al^{3+} in this structure. Having strong Al-oxygen bonds generates a more robust crystal structure and prevents the dissolution of TM ions. This permanence also helps its air stability, which is important for major production in electric vehicle industries. However, NCA suffers from generating many micro-cracks in its structure during cycling and high sensitivity to a wide operating range in the depth of discharge (ΔDOD) [11,20].

LiM_2O_4 is considered as spinel oxide only when M = Mn, V, and Ti, due to the difficult stabilization of M element with high oxidation states $M^{3+/4+}$. The most famous one in this second oxide group is the spinel $LiMn_2O_4$ (LMO). LMO belongs to the $Fd\bar{3}m$ space group, with $Mn^{3+/4+}$, $Li^{+,}$ and oxygen anions in the 16d octahedral sites, the 8a tetrahedral sites, and the 32e sites (cubic close-packed arrangement), of the spinel structure, respectively. This framework exhibits 3-dimensional diffusion channels for Li^+ via 8a-16c-8a, in which the 16c position is an empty octahedral site. However, inserting an additional Li into the empty sites of 16c octahedral instead of the 8a tetrahedral site will induce sudden displacement in the structure and reduce the operating voltage by about 1V. Furthermore, the presence of Mn^{3+} (t_{2g}^6 e_g^1) which is Jahn-Teller active, in the mentioned structure, $[Li_2]_{16c}[Mn_2]_{16d}O_4$, induces the phase transition from cubic to tetragonal phase along with a high amount of volume alternations. Another crucial concern about the LMO with spinel structure is the manganese dissolution (due to the trace of acidity in the electrolyte), which not only damages the cathode lattice but also contaminates the graphite anode and reduces the cyclability of the LIBs [11,16].

Olivine or polyanion oxide is the third group of the oxide-based cathode. In this crystal, the presence of large $(XO_4)^{3-}$ (X = W, As, P, Mo, S, Si) polyanions not only alleviate their structures but also boost the redox potential of the cathodes. Due to the characteristics changing in the bonding between Fe and O, the operating voltage of $Fe_2(XO_4)_3$ (X = S, Mo, and W) structure with polyanion oxides is higher than the simple Fe_2O_3. Through the presence of the more covalent nature of the Mo–O or W–O bond, the covalency band between Fe and O becomes weaker, the redox energy of $Fe^{2+/3+}$ is reduced, and subsequently, the operating voltage is enhanced. One of the well-known materials in this group is $LiFePO_4$ (LFP), which has good thermal stability and a lower price with an

orthorhombic crystalline system. LFP has a slightly distorted hexagonal close-packed (HCP) oxygen framework, with P^{5+} ions in the tetrahedral sites along with Fe^{2+} and Li^{+} ions in octahedral sites. The main drawbacks of the LFP are a low amount of electrical and ionic conductivities, as well as a comparatively low amount of average voltage [11,14,16].

In a comparison between these three main classes of oxide-based cathodes, the spinel and layered categories exhibit high density with compact crystal structure and good electronic conductivity, while these properties are the polyanion oxide class's drawbacks. On the other hand, the polyanion oxides group has a high level of thermal stability than those first groups, making it safer. The layered oxides category is more demanding between the first two classes because of their extensive variety of compositions. The main purpose in this field is to reach the highest possible energy density to fulfill modern life demands, specifically in the electric vehicle industry [11].

1.4 Engineered complex cathode materials

There are so many efforts to boost the energy density of LIBs, such as raising the operating voltage by tailoring the composition of the electrolyte or adding different additives, and increasing storage capacities of the electrodes (by using conversion-reaction cathodes and anodes or lithium-rich layered oxides, $Li_{1+x}(Ni_{1-y-z}Mn_yCo_z)_{1-x}O_2$). A new approach focuses on increasing the amount of nickel in the layered oxide structures, which is believed to be a dominant expeditious technology. However, higher nickel content causes some serious problems which should be addressed, such as the high reactivity of Ni-enriched cathodes (which causes active material consumption and capacity reduction, gas release, and thermal stability reduction), cation mixing, and microcracks formation [19,21].

The recurring occurrence of the H2 → H3 (2 different hexagonal phases) phase transition induces cyclic internal stresses in the structure, causing stress-induced microcracks. These microcracks deteriorate the mechanical integrity of the cathode and its passivation layer (the Solid Electrolyte Interphase) and provide microchannels for electrolyte infiltration into the particle core [20–22]. To overcome these problems, several methods, including doping, core-shell structures, or coating, can be utilized to stabilize the high-nickel layered oxide cathodes and enhance their performance.

Atomic doping is one of the most effective bulk modification strategies, which introduces some substituted atoms inside the host crystal structure to enhance the battery performance by various mechanisms, which are not yet fully understood for some dopants. Various studies have been conducted using small amounts of different elements (zirconium, magnesium, aluminum, tungsten, molybdenum, etc.) within the Ni-rich cathode structures. The major effects of cation doping can be summarized as follows:

I. Increasing the retained capacity and structural stability because of the stronger bonding between metal and oxygen and preventing oxygen release or inhibiting the collapse of the Li interlayer in the charging process and cation mixing [11,17,21,23];
II. increasing the electrochemical activity and stability by balancing electrostatic repulsion as a result of the presence of high-valent foreign cations that contributes to the charge compensation [23,24];
III. facilitate the Li-ion diffusion by increasing the Li layer distance or reducing the energy barrier regarding Li-ion diffusion alongside the surface with high dopant concentration [17,25];
IV. suppressing unwanted structural transformation from layered structure to either spinel or rock salt phase (electrochemically inactive) [23,25];
V. changing the electronic structure of the material (including a combination of these effects) [23].

However, in the anion doping approach, O^{2-} is exchanged by other anions (namely S^{2-}, Cl^{-}, F^{-}) to energetically reinforce the binding in-between the higher electronegative anions and the TM cations. Therefore, the performance of the Ni-enriched cathode materials, such as rate capability, retention capacity, its surface resistivity toward HF attacks, will be improved [17,25,26].

Coating is the surface modification approach in which different materials, including metal oxides (TiO_2, Al_2O_3, Li_2TiO_3, ZrO_2, etc.), phosphates ($LiFePO_4$ (LFP), $LiTi_2(PO_4)_3$, etc.), metal fluorides and carbon have been applied to enhance the electrochemical performance of Ni-rich cathode materials. Coatings mostly play a protection layer role in suppressing parasitic reactions due to the direct contact of the electrolyte with the highly active material in the cathode's surface (reduces the extremely reactive Ni^{4+} on the surface). Moreover, they also bring other benefits, such as reducing the cathode surface corrosion when it faces HF in the oxide-based coating as well as making a steadier buffer film in the formation step (initial cycles) due to the more thermodynamic stability of phosphate- and fluoride-based coatings. However, most coatings suffer from the rate capability (rapid rates for charge and discharge), due to their intrinsic insulator behavior and insufficient prevention from microcrack formation, especially in the ultra-rich Ni cathodes (more than 80% Ni). Coating resistivity will be improved by adding conductive materials such as polymer-based and carbon coatings or utilizing $FePO_4$, which reduces the activation energy required for the transferring charge [17,25–27].

In the coating approach, it is essential to optimize the coating uniformity and thickness. Using dry coating methods (such as ball-milling) generate an uneven coating, although, in wet approaches, the coating becomes more uniform along with some impurity formations via the leaching of Li from the Ni-rich structure and the reaction between trivalent Ni ions

and liquid medium. Although chemical vapor deposition (CVD) and atomic layer deposition (ALD) approaches can be utilized to make high-quality coating layers, they are not economically favorable [25,26].

Core-Shell or Concentration Gradient structures are exploited to modify the cathode surfaces by reducing the Ni content at the surface (which is the main reason for thermal instability and side reactions with the electrolyte). In this category, the concentration gradient of Ni changes from core to the surface in a gradual (full concentration gradient structures), instant (core-shell structures), or moderate (multilayer-core-shell) manner. The main differences between the coated cathode and the core-shell structure are having lithium ion conductive, and thicker film with a similar crystal structure in the core-shell method. The quality of final core-shell structures depends on optimizing the synthesis procedure by considering core and shell composition and avoiding Ni depletion as well as shell elements diffusion during the process, heat treatment and lithiation time and temperature, and also the final size of the particles and thickness of the shell [25,28,29].

Figure 1-6 summarizes these three main improvement approaches to making engineered complex cathode materials.

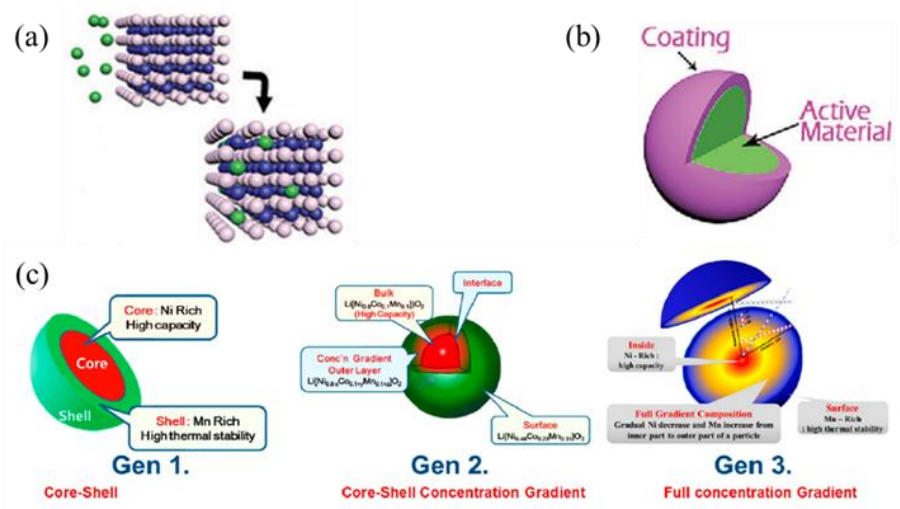

Figure 1-6 Representation of different engineering complex structures from (a) Doping, (b) Coating [30], and (c) Core-shell approaches [28]. Reused with permission from the copyright owners.

1.5 Li-ion diffusion Behavior

The systematic behavior of Li-ion reacting with electrode structures, or in other words, the lithiation/de-lithiation process, can be classified into three main groups:

I. Intercalation reactions (in which Li ions enter the host structure with low volume change and more stable structure but having low capacity due to the limiting number of accommodation locations or the limiting number of one electron storage per each metallic ion);

II. Conversion reactions (in which, through the lithiation process, the electrode materials transform into Li_2O and its metallic form and the reverse reaction occurs during delithiation. Although they deliver a high amount of specific capacity since several electrons are involved in the conversion reaction for a single M atom, they suffer from high volume change, alternation in electron conductivity, low kinetics rate, and huge

hysteresis in potential due to the presence of an energy barrier required for the M–O bond breaking);

III. Alloy reactions (the alloy materials provide high specific energy density because of their capability for storing several Li-ions, however, they suffer from large volume alternation, low kinetics rate, and poor cyclability).

Figure 1-7 depicts a schematic representation of each three common reaction mechanisms with their main advantages and disadvantages [30].

Several mathematical models can be applied to describe the lithium-ion diffusion process for instance: a shrinking-core model, a core-shell model, and a mosaic model [31,32]. To validate any of these models, using operando synchrotron high-energy X-ray diffraction (XRD) or high-resolution transmission electron microscopy and electron energy loss spectroscopy (HRTEM and EELS) could be helpful [31,33].

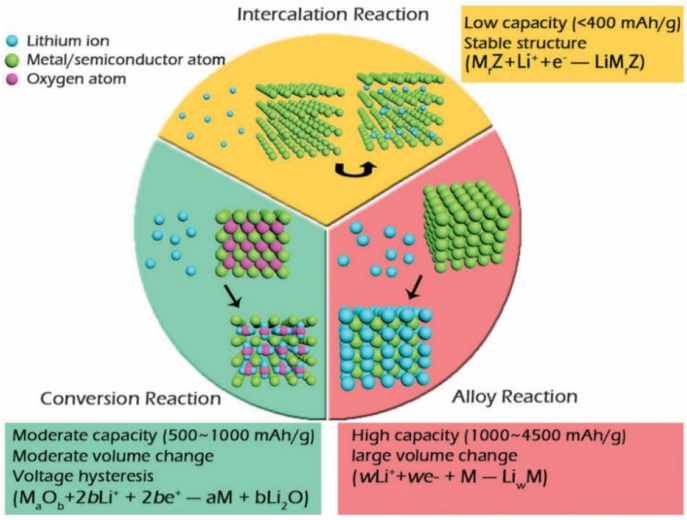

Figure 1-7 The three common reaction behaviors occur between Li-ion and electrodes [30]. Reused with permission from the copyright owner.

1.6 Cathode characterization techniques

Li-ion batteries are utilized in a wide range of applications, from phones to electric vehicles, and there are an increasing number of demands to improve LIB performance and safety. A fundamental understanding of LIBs and a full evaluation of the battery materials are necessary to fulfill these demands, which can be accomplished using advanced analysis techniques. In this regard, various powerful techniques have been used in the LIB field, such as scanning electron microscopy (SEM), scanning/transmission electron microscopy (S/TEM), energy dispersive X-ray spectroscopy (EDXS), electron energy loss spectroscopy (EELS), X-ray absorption fine structure (XAFS), X-ray diffraction (XRD) and pair distribution function (PDF). Some of the higher-end techniques will be briefly introduced in the following sections. These techniques can be divided into two main groups: electron-based and X-ray based. Commonly, electron microscopy techniques can be used when a high spatial resolution in a tiny area (nanometer scale) is required, and X-ray techniques will be useful in a wider range (revealing average properties) and the detection of heavier elements.

1.6.1 STEM

The transmission electron microscope is one of the most powerful instruments with a wide range of high spatial resolution, which can be used in either quantitative or qualitative analysis. This instrument is equipped with high-resolution transmission mode (HRTEM), scanning TEM (STEM) with annular bright field (ABF), annular dark field (ADF), and high-angle annular dark field (HAADF) detectors, as well as electron energy loss spectrometer (EELS) and energy dispersive X-ray (EDX) spectroscopy. These options empower TEM to detect chemical and structural information on an atomic resolution scale, and the resolution can be even further enhanced by a spherical aberration corrector

attachment (Cs corrector) into the STEM (sub-Ångstrom detail). In general, the bright-field detector is mainly used for imaging light elements in the structure, and dark-field images, which are complementary to ABF images, have information about the location of the heavy elements inside the structure. The best advantage of using HAADF in STEM over HRTEM, is its simple and direct interpretation of atomic number or Z-contrast in HAADF images (nearly proportionate of Z^2). In HAADF imaging, in contrast to ADF imaging, Bragg-scattered electrons are not participating in the formation of the images due to the very high-angle scattered electron collection (above 50 mrad). However, image interpretation is not directly possible in HRTEM without simulations because of the phase-contrast bases of HRTEM image, which are altered by image lens aberrations (spherical aberration, astigmatism, and defocus) [24,25] and dynamical scattering of the electron beam as it propagates in the sample [34–37]. Figure 1-8 illustrates the location and the collection angle range of each detector in the STEM.

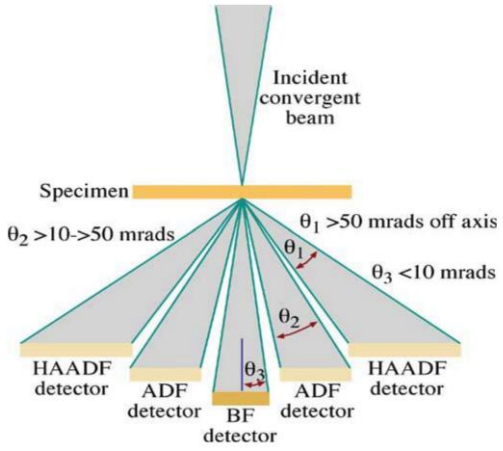

Figure 1-8 Schematic of different detectors' locations in STEM mode [34]. Reprinted with permission from the copyright owner.

HAADF-STEM can also be used to study the antisite defects (differentiating between two octahedral sites) with the aim of studying the structural stability of the crystal in an atomic-

level resolution instead of using macroscopic diffraction methods. This visualization is possible, for instance, when some heavier atoms, like Fe or Co, occupy Li columns in LFP or $LiCoPO_4$ crystals and make Li locations appear in HAADF images [38,39].

With the purpose of understanding the structural changes in Li-rich cathode materials (with high energy density due to the occurring anionic redox processes reversibly), there are some efforts to directly measure oxygen sublattice distortion by utilizing ABF STEM. However, the precise measurement of the anion distortions is tricky because of some challenging issues, including (1) ABF-STEM images sensitivity to the sample thickness and the contribution of the surface especially in the presence of different phases from bulk; (2) the close location of the oxygen columns to each other (in case of having two perpendicular projection of axial and equatorial) as well as having TMs (heavy elements) in between the oxygen column locations [40].

Nevertheless, by using a fast, pixelated detector and acquiring four-dimensional scanning transmission electron microscopy (4D-STEM) data (i.e. a 2-dimensional diffraction pattern at every pixel of a 2-dimensional image), capturing all of the elements inside the cathode structure, even light elements such as lithium, inside $LiNiO_2$, could be possible. Studies showed that the contrast of the Li atoms was improved, especially in thicker TEM samples, using enhanced ABF (e-ABF) imaging instead of ABF (with angles from 8 to 16 mrad), which is achieved by subtracting Medium-angle-BF (with angles of 0 and 8 mrad) from the regular ABF. Figure 1-9 illustrates the improvement of e-ABF images by increasing the sample thickness as well as their both (ABF and e-ABF) good sensitivity to exhibit Li and O atoms [41,42].

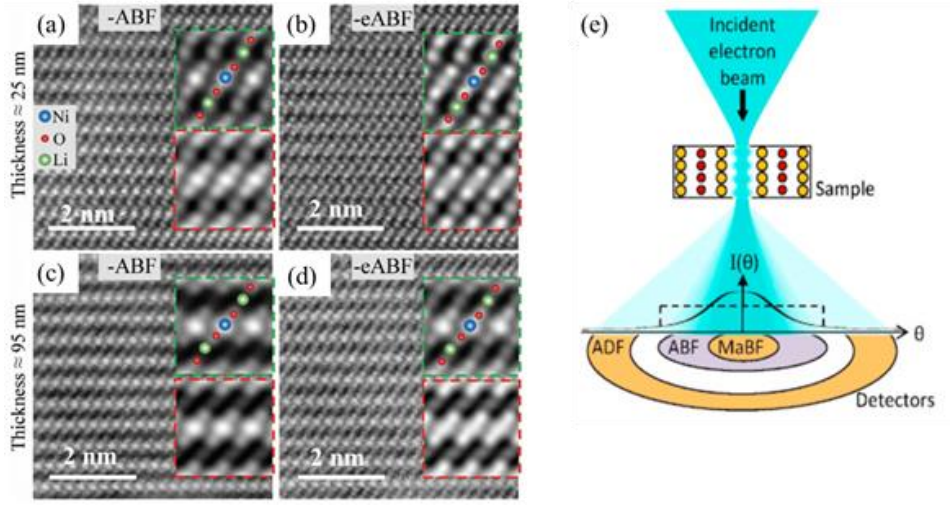

Figure 1-9 High-resolution ABF and enhanced-ABF images from [100] zone axis of $LiNiO_2$ with a thickness (a) and (b) about 25 nm and (c) and (d) about 95 nm. With magnified averaged images from the experiment (green-frame) and simulation (red-frame) [41]; (e) A schematic of the MaBF detector location in high-resolution STEM [42]. Reprinted with permission from the copyright owners.

Besides imaging, the 4D-STEM technique can also be used for strain measurements on the nanoscale. In this method, like nanobeam electron diffraction (NBED), the strain is calculated in reciprocal space since alternations in the values of the structural lattice will be reflected as position shifting in diffracted disc regarding the undiffracted disc in the diffraction pattern center [43,44]. Appendix I, shows an example regarding this calculation.

ADF images can reveal the differences between the two disparate crystallographic structures. In this regard, the chosen zone axis for analysis should show different features or at least different ratios in the same feature (like different ratios for diagonal distance in the diamond shape of $LiMn_2O_4$). By decreasing the detection angle, ADF can show sufficient contrast for O sites. Figure 1-10 depicts the location of the Mn and O by reducing the collection angles [45].

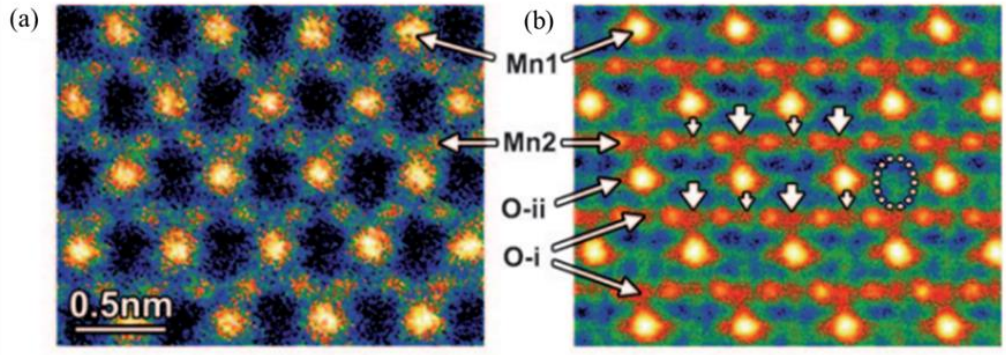

Figure 1-10 ADF images from $Li_{1-x}Mn_2O_{4-\delta}$ materials with tetragonal crystal aligned in [100] direction, based on different collection angles: (a) 92–228 mrad and (b) 52–140 mrad. The contrast level in (b) regarding oxygen is not uniform, which is illustrated with short and large arrows [45]. Reprinted with permission from the copyright owner.

With the intention of studying the degradation mechanism in Ni-rich cathode materials, HAADF images can be extensively used to observe the differences between layered structure and degraded structure (rock-salt-type structure) near the surface or grain boundaries. As seen in Figure 1-11, Li layers can be determined owing to the presence of heavier elements (TM) in the Li layers. According to the Li layers' contrast level up from the core to the grain boundary, the structure progressively deviates from the layered structure to the moderately layered structure and then reaches the disordered rock-salt structure. It is worth mentioning that the thickness of this disordered rock-salt structure (with a higher amount of TM atoms in Li sites) increases with the number of cycles [46,47].

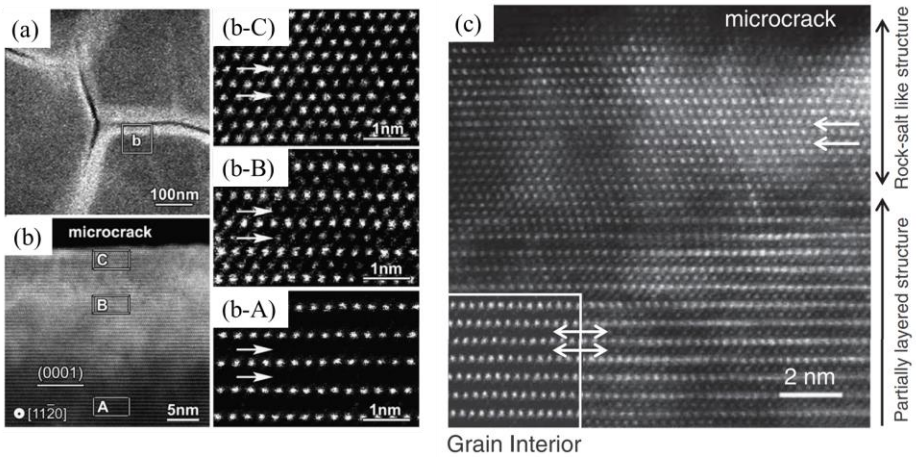

Figure 1-11 HAADF-STEM images of $LiNi_{0.8}Co_{0.15}Al_{0.05}O_2$ after one cycle in (a) and (b) [46], and after 10 cycles in (c) [47]. Li layers are revealed with double-headed arrows and single-headed arrows. Reused with permission from the copyright owners.

1.6.2 EELS

Electron energy-loss spectroscopy (EELS) is one of the most powerful tools inside the TEM, placed either at the end of the TEM column or in its projector lens system (post- and in-column filters). This technique is capable of delivering valuable information with a high spatial resolution (Ångstrom level) about the chemical state, local electronic structure, phase recognition, local changes in bonding environment, valance and ionicity, and radial distribution function. EELS analysis is much more appropriate than EDXS in detecting light atoms in the system because of the decreasing trend in the fluorescence yield (orders of magnitude) of light elements in comparison to the heavier ones, as well as having higher detector efficiency in EELS (due to small solid angle and X-ray absorption with a detector in EDXS). The energy loss spectrum generally can be divided into two main regions, Low-loss (from 0 ev to 50-100 ev) and Core-loss (above the low-loss region). The Core-loss energy range has two main modulations: the energy loss near edge structures (ELNES) and the extended energy loss fine structures (EXELFS). The ELNES part is assigned in up to

10-30 ev after the onset of ionization edge, and from 30-50 ev to several hundred electron volts is considered as EXELFS region. Information about phase and valance state as well as radial distribution function of materials (like XANES and EXAFS) are provided from ELNES and EXELFS regions, respectively [48,49].

In the field of LIBs, EELS has also been used for detecting Li since its K-edge is located in the low-loss region. However, the overlapping of $M_{2,3}$-edges and K-edge in TM elements and lithium, respectively, makes the analysis more complex, especially in a more realistic case of having polycrystalline structure and thickness variation in prepared TEM samples [41,50]. Multivariate curve resolution (MCR) is one way of separating mixed spectra in each position into a linear combination of different pure components by using least-squares fitting [50]. MCR can be used in the energy loss spectrum to investigate the local valance states and quantitative mapping of the TM ions and oxygen in the cathode active materials in real space [51]. Multiple linear least squares (MLLS) methode is another common fitting technique that fits reference spectra into the original dataset to calculate and extract each reference's amount and distribution in a spectrum image. It is also utilized for separating overlapping edges and for background improvement. Analyzing a large data cube like an EEL spectrum image (SI) with many variables, which are sometimes known or unknown, requires multivariate statistical analysis (MSA) to understand spectral data. One of the most common MSA approaches in the EELS field is principal component analysis (PCA). Through PCA, the dimension or the number of variables in the original data is reduced, and the spectral with a lower noise level without losing substantial information is obtained [52].

1.6.3 X-ray absorption fine structure (XAFS)

X-ray absorption is based on the ratio between the intensity of monochromatic X-rays after and before interacting with an examined sample. To see a sharp absorption edge, the energy of the incident X-ray beam should be equal to the electron energy bonding in a studied material's core level. In general, when the X-ray energy is close and higher than the binding energy, some of the sample's electrons might be removed from their ground quantum level (become excited by leaving holes in core levels), and two major mechanisms might happen. In the first one, the core hole is filled by another electron from the core level with higher energy, and the difference between these two levels will be revealed as fluorescence emission. This emission is the characteristic property of each element and can be utilized to detect the atoms. The second mechanism might happen if the energy difference between those two mentioned levels has enough energy to eject another electron into the continuum, called the Auger Effect. It should be noted that X-ray fluorescent and Auger emission are more dominantly taking place at higher X-ray energies (>2 keV), and soft X-ray regimes, respectively. It is worth to be noted that by absorbing X-ray energy, if the ejected photoelectron (with a wave property) from a tightly bound core-level has enough kinetic energy, it can escape into unoccupied states of the absorber element and interact with other electrons in the chemical neighborhood of the absorber atom. The photoelectron can scatter back from the local neighbor atoms' electrons into the absorber one and generate modulations in the extended part of absorber coefficient shape of the absorbing atom. Therefore, the XAFS can be classified into two main sections: the X-ray absorption near-edge structure (XANES) is visible from the threshold of the main absorption edge up to 30 eV, and the extended X-ray absorption fine-structure (EXAFS) which contains the oscillations which are resolved fairly after the absorption edge. The EXAFS is mostly

illustrated in terms of the wave number (meaning $\chi(k)$ as a function of k [$Å^{-1}$]) and also due to its fast decay, $\chi(k)$ is amplified by k^2 or k^3. The several frequencies, which are revealed as oscillations in $\chi(k)$, are related to the different coordination of neighboring shells and can be used in order to calculate the neighboring atoms' number, distances, and disordering. A synchrotron is mainly employed as an X-ray source in this technique and offers a full wavelength or energy range of X-ray with high intensity. This full wavelength range can be designated for a specific energy by using a monochromator (such as silicon) to reach high energy resolution (about 1 eV at 10 keV). XAFS measurement can be divided into two main categories: transmission measurements and fluorescence measurements. The first method is suitable for low-thickness and uniform samples, and the second is preferred for thicker or lower elemental concentrated samples [53,54]. It is worth noting that the EXAFS technique can illustrate the structural environment around the specific absorber element mostly up to 6 Å distance; however, to see all the bonding pair distances in the material structure, using another X-ray-based technique called pair distribution function (PDF), would be required [55,56].

XAFS analysis in LIBs can be used to calculate the capacity degradation and amount of inactive materials production based on the energy shifting in Ni K-edge as a function of different SOC and cycling effect, especially at high temperatures. As shown in Figure 1-12, the K-edge onset of Ni is shifted to higher energies by increasing the SOC, due to the oxidation of the Ni^{3+} ion to the Ni^{4+} ion. After applying 500 cycles at high temperatures, the K-edge onset of Ni was reduced to lower energies. The shifting at a fully charged state results from the reduced number of available Ni^{4+} due to the production of "inactive Ni ions" (Ni^{2+} and Ni^{3+}), which are not able to change their valence during cycling. At high

temperatures, since the Ni ion reduction happens with no Li intercalation (at the same SOC), oxygen release could cause capacity fading [57].

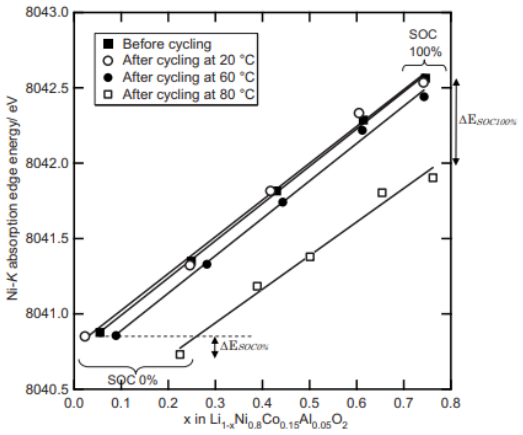

Figure 1-12 Shifting in the location of Ni K-edge energy from XANES spectra versus the SOC of NCA before and after the 500 cycles [57]. Reprinted with permission from the copyright owner.

1.7 Motivation

In light of global warming and increasing carbon dioxide emissions, there are enormous demands for using different kinds of green and sustainable energy sources along with finding high-energy storage devices. Some countries have planned the banning fossil fuel vehicles in imminent future, and in this regard, automotive industries are currently forced to manufacture electrified vehicles that can be adapted to these bans. To this end, Li-ion batteries have received significant attention and entered the electric vehicle industry because of their higher energy density in comparison with other rechargeable battery technologies. As addressed earlier, cathode materials have an important role in energy density restriction and the final material price determination of LIBs. Thus, it is essential to scrutinize cathode structures, their phase transformation, and side reactions to boost the life span of the batteries. Recent studies have utilized two main approaches, involving the

discovery of new materials or modifying the existing materials, which both aim to improve the performance and cyclic life of a lithium-ion battery. Despite several developments in both methods, most studies focused on the overall performance of the battery, whereas fundamentally analyzing the underlying phenomena which lead to enhanced performance or fast degradation of these batteries was mostly neglected. Therefore, this research aims to comprehensively study these engineered complex materials by using advanced electron microscopy techniques (SEM, TEM, STEM-EELS, P/FIB, and 4D-STEM) and high-resolution synchrotron-based X-ray analysis (XAFS, powder XRD, and PDF) to achieve a detailed understanding of which mechanisms and reactions are occurring inside the batteries as well as their effects on the final performance of the batteries, from the material perspective. The final results of this research will impact the cathode modification procedures, which will be exploited to enhance the LIBs performance that are manufactured by several companies.

1.8 Research objectives

The interest in engineered complex cathode materials has grown due to the role of these materials in providing higher quality in the performance of the LIBs. To fully benefit from these modern materials, it is essential to have a deep and fundamental understanding of the relationship between their performance and chemical/structural properties which provides the opportunity to comprehend the possible enhancement mechanisms and detrimental factors for capacity deterioration, particularly from the material point of view. Based on the literature review, several topics have been identified which are not explored comprehensively in this field and therefore require more scrutiny.

- Enquiring the inhomogeneous distribution of elements, especially in doped materials, from the surface to the bulk and the dopant position, which play essential roles in the performance of Li-ion batteries. Since in this research, W-doped Ni-rich cathode materials are being investigated, using EELS and HAADF-STEM along with EXAFS and XANES spectroscopies are required in order to acquire comprehensive information regarding the exact location of W, its phases and structures, as well as its valence and site preference in the doped host structure in pristine and cycled states.

- Exploration of possible mechanisms that are responsible for performance degradation and enhancement in engineered complex cathode materials. This analysis requires an in-depth study of the chemical and structural changes inside lithium-ion batteries before and after cycling. In this investigation, utilizing various advanced characterization techniques such as HRTEM, STEM-EELS, XRD, and XAFS analysis will be of utmost importance to achieve a better understanding. The electron-based examinations are chosen due to their capability to reveal information about alternation in electronic and crystal structure of modified cathode materials in both pristine and cycled states (to consider the effects of phase transitions and other side reactions), with high spatial resolution. On the other hand, X-ray-based analysis can illustrate the bulk effect of the modifying approaches in cathode structure, especially in the presence of heavy elements inside the structure.

- In coating approaches, it is necessary to scrutinize the final structure of the core and coating along with examining the possibility of having interdiffusion at the nano to micro-scales between core and coating materials. This procedure is

necessary for the purpose of optimizing the processing parameters and evaluating the effectiveness of these approaches to improve cell performance. SEM, EDX, STEM, selected area electron diffraction (SAED), convergent beam electron diffraction (CBED), and EELS can all be used to reveal valuable data regarding the uniformity of the coating, material distribution from the core to surface, and the crystal structure of each selected area.

- Since the main causes of micro-cracks generation, specifically in Ni-rich cathodes, are not clearly discussed and understood in the literature, developing a reliable method for strain measurement in cathode structures is one of the objectives of this study. Strain measurements analysis could be performed on both pristine and cycled states to understand the main reasons that contribute to the structural stability or degradation of the cathode as well as any changes that are induced by enhancement techniques in the cathode particles. In this measurement, peak width from synchrotron-based XRD data or shifting in PDF peaks could be utilized to precisely measure the structural strain. On the other hand, electron microscopy methods with high spatial resolution can be employed to calculate strain by using direct (from real space location of the atoms, which requires high quality HRTEM micrographs) and indirect (from reciprocal space, which can be obtained through 4D-STEM analysis) methodologies.

Ultimately this study will provide in-depth information on the underlying reasons that result in the higher performance or deterioration of the engineered complex cathode structures in a Li-ion battery. This work will be crucial for expanding the impact of Li-ion batteries, enabling wider use of electric vehicles, and reducing carbon emissions leading to climate change.

1.9 Thesis outline

Through this Ph.D. journey, three conferences, one workshop, and six published ISI papers in prominent journals have been the outcomes that resulted from our collaboration with Prof. Jeff Dahn from Dalhousie University. From our collaboration with NRC, one paper was published. Additionally, I would state that through other collaborations, two papers on different topics were published as well. The following chapters present our three publishable papers as the first author with the dominant contributions of the Ph.D. candidate in acquiring and interpreting the data as well as being the primary writer of these manuscripts. This sandwich thesis is composed of five major chapters as follows:

Chapter 1 (the current chapter) contains some LIB introductions, cathode materials and their development through complex engineering structures, different characterization techniques (electro- and photon-based), as well as the research motivations and objectives.

Chapter 2 is based on the first paper, currently under review, entitled "Probing the Mysterious Behavior of Tungsten as a Dopant Inside Pristine Cobalt-Free Nickel-Rich Cathode Materials". In this paper, the location and distribution of W have been investigated and its form (crystalline or amorphous) along with its more possible compound chemistry have been discussed. This chapter mainly focuses on the pristine state of the W-enriched structures and fulfills the first two objectives of this research.

Chapter 3 is written based on the second paper, ready to be submitted, titled "Structural Evolution of Cycled Complex Nickel-Rich Cathode Materials Enriched with Tungsten". This article presents the failure analysis of W-enriched materials, the mechanical and chemical improvement role of W compounds in the Ni-rich cathode structures, and the effect of some synthesis defects. According to the results and discussion in this chapter, the two initial aims of this thesis have been accomplished. In both the second and third chapters, strain analysis has been done based on the PDF analysis, which is part of the last objective of this research.

Chapter 4 presents a version of the third paper's final draft, entitled "Exploring the Effect of Surface Modification on the Coated Nickel-Rich Cathode Materials Structures". This paper characterized the quality of the coating by mechanofusion and the effect of this process on Ni-rich cathode materials' behavior through different electron-based analysis techniques. This article helps to meet the last two goals of this research.

Chapter 5 includes the major conclusions regarding this thesis on two main structural enhancement techniques, doping, and coating, as well as introducing some possible advice for future work.

1.10 References

[1] D. Linden, T.B. Reddy, HANDBOOK OF BATTERIES, Third Edit, 2002.

[2] H. Budde-Meiwes, J. Drillkens, B. Lunz, J. Muennix, S. Rothgang, J. Kowal, D.U. Sauer, A review of current automotive battery technology and future prospects, Proc. Inst. Mech. Eng. Part D J. Automob. Eng. 227 (2013) 761–776. https://doi.org/10.1177/0954407013485567.

[3] M. Armand, Nature Lithium Battery, Nature. 414 (2001) 359–367. https://doi.org/10.1038/35104644.

[4] L. Lu, X. Han, J. Li, J. Hua, M. Ouyang, A review on the key issues for lithium-ion battery management in electric vehicles, J. Power Sources. 226 (2013) 272–288. https://doi.org/10.1016/j.jpowsour.2012.10.060.

[5] A. Yoshino, The birth of the lithium-ion battery, Angew. Chemie - Int. Ed. 51 (2012) 5798–5800. https://doi.org/10.1002/anie.201105006.

[6] C. Liu, Z.G. Neale, G. Cao, Understanding electrochemical potentials of cathode materials in rechargeable batteries, Mater. Today. 19 (2016) 109–123. https://doi.org/10.1016/j.mattod.2015.10.009.

[7] U. Gulzar, S. Goriparti, E. Miele, T. Li, G. Maidecchi, A. Toma, F. De Angelis, C. Capiglia, R.P. Zaccaria, Next-generation textiles: From embedded supercapacitors to lithium ion batteries, J. Mater. Chem. A. 4 (2016) 16771–16800. https://doi.org/10.1039/c6ta06437j.

[8] I. Chu, M. Zhang, S.P. Ong, Y.S. Meng, Battery Electrodes, Electrolytes, and Their Interfaces, in: Handb. Mater. Model., 2018: pp. 1–24. https://doi.org/10.1007/978-3-319-50257-1_96-1.

[9] A. Wang, S. Kadam, H. Li, S. Shi, Y. Qi, Review on modeling of the anode solid electrolyte interphase (SEI) for lithium-ion batteries, Npj Comput. Mater. 4 (2018) 0–26. https://doi.org/10.1038/s41524-018-0064-0.

[10] J.B. Goodenough, K.S. Park, The Li-ion rechargeable battery: A perspective, J. Am. Chem. Soc. 135 (2013) 1167–1176. https://doi.org/10.1021/ja3091438.

[11] A. Manthiram, A reflection on lithium-ion battery cathode chemistry, Nat. Commun. 11 (2020) 1–9. https://doi.org/10.1038/s41467-020-15355-0.

[12] S. Ernst, T.P. Heins, N. Schlüter, U. Schröder, Capturing the Current-Overpotential Nonlinearity of Lithium-Ion Batteries by Nonlinear Electrochemical Impedance Spectroscopy (NLEIS) in Charge and Discharge Direction, Front. Energy Res. 7 (2019) 1–13. https://doi.org/10.3389/fenrg.2019.00151.

[13] J. Kasnatscheew, U. Rodehorst, B. Streipert, S. Wiemers-Meyer, R. Jakelski, R. Wagner, I.C. Laskovic, M. Winter, Learning from Overpotentials in Lithium Ion Batteries: A Case Study on the LiNi 1/3 Co 1/3 Mn 1/3 O 2 (NCM) Cathode, J. Electrochem. Soc. 163 (2016) A2943–A2950. https://doi.org/10.1149/2.0461614jes.

[14] N. Nitta, F. Wu, J.T. Lee, G. Yushin, Li-ion battery materials: Present and future, Mater. Today. 18 (2015) 252–264. https://doi.org/10.1016/j.mattod.2014.10.040.

[15] E. Boivin, J.N. Chotard, M. Ménétrier, L. Bourgeois, T. Bamine, D. Carlier, F. Fauth, E. Suard, C. Masquelier, L. Croguennec, Structural and electrochemical studies of a new Tavorite composition: LiVPO4OH, J. Mater. Chem. A. 4 (2016) 11030–11045. https://doi.org/10.1039/c6ta03339c.

[16] C.M. Julien, A. Mauger, K. Zaghib, H. Groult, Comparative Issues of Cathode Materials for Li-Ion Batteries, Inorganics. 2 (2014) 132–154. https://doi.org/10.3390/inorganics2020132.

[17] A. Chakraborty, S. Kunnikuruvan, S. Kumar, B. Markovsky, D. Aurbach, M. Dixit, D.T. Major, Layered Cathode Materials for Lithium-Ion Batteries: Review of Computational Studies on LiNi1- x- yCoxMnyO2 and LiNi1- x- yCoxAlyO2, Chem. Mater. 32 (2020) 915–952. https://doi.org/10.1021/acs.chemmater.9b04066.

[18] E.M. Erickson, F. Schipper, T.R. Penki, J.-Y. Shin, C. Erk, F.-F. Chesneau, B. Markovsky, D. Aurbach, Review—Recent Advances and Remaining Challenges for Lithium Ion Battery Cathodes, J. Electrochem. Soc. 164 (2017) A6341–A6348. https://doi.org/10.1149/2.0461701jes.

[19] A. Manthiram, An Outlook on Lithium Ion Battery Technology, ACS Cent. Sci. 3

(2017) 1063–1069. https://doi.org/10.1021/acscentsci.7b00288.

[20] S. Watanabe, M. Kinoshita, T. Hosokawa, K. Morigaki, K. Nakura, Capacity fade of LiAlyNi1-x-yCoxO 2 cathode for lithium-ion batteries during accelerated calendar and cycle life tests (surface analysis of LiAlyNi1-x-yCo xO2 cathode after cycle tests in restricted depth of discharge ranges), J. Power Sources. 258 (2014) 210–217. https://doi.org/10.1016/j.jpowsour.2014.02.018.

[21] F. Schipper, E.M. Erickson, C. Erk, J.-Y. Shin, F.F. Chesneau, D. Aurbach, Review—Recent Advances and Remaining Challenges for Lithium Ion Battery Cathodes, J. Electrochem. Soc. 164 (2017) A6220–A6228. https://doi.org/10.1149/2.0351701jes.

[22] T. Li, X.-Z. Yuan, L. Zhang, D. Song, K. Shi, C. Bock, Degradation Mechanisms and Mitigation Strategies of Nickel-Rich NMC-Based Lithium-Ion Batteries, Springer Singapore, 2019. https://doi.org/10.1007/s41918-019-00053-3.

[23] F. Schipper, M. Dixit, D. Kovacheva, M. Talianker, O. Haik, J. Grinblat, E.M. Erickson, C. Ghanty, D.T. Major, B. Markovsky, D. Aurbach, Stabilizing nickel-rich layered cathode materials by a high-charge cation doping strategy: Zirconium-doped LiNi0.6Co0.2Mn0.2O2, J. Mater. Chem. A. 4 (2016) 16073–16084. https://doi.org/10.1039/c6ta06740a.

[24] M. Dixit, M. Kosa, O.S. Lavi, B. Markovsky, D. Aurbach, D.T. Major, Thermodynamic and kinetic studies of LiNi0.5Co0.2Mn0.3O2 as a positive electrode material for Li-ion batteries using first principles, Phys. Chem. Chem. Phys. 18 (2016) 6799–6812. https://doi.org/10.1039/c5cp07128c.

[25] P. Teichert, G.G. Eshetu, H. Jahnke, E. Figgemeier, Degradation and aging routes of ni-rich cathode based li-ion batteries, Batteries. 6 (2020) 1–26. https://doi.org/10.3390/batteries6010008.

[26] H.H. Sun, H.H. Ryu, U.H. Kim, J.A. Weeks, A. Heller, Y.K. Sun, C.B. Mullins, Beyond Doping and Coating: Prospective Strategies for Stable High-Capacity Layered Ni-Rich Cathodes, ACS Energy Lett. 5 (2020) 1136–1146. https://doi.org/10.1021/acsenergylett.0c00191.

[27] X. Liu, H. Li, E. Yoo, M. Ishida, H. Zhou, Fabrication of FePO 4 layer coated LiNi 1/3Co 1/3Mn 1/3O 2: Towards high-performance cathode materials for lithium ion batteries, Electrochim. Acta. 83 (2012) 253–258. https://doi.org/10.1016/j.electacta.2012.07.111.

[28] A. Konarov, S.T. Myung, Y.K. Sun, Cathode materials for future electric vehicles and energy storage systems, ACS Energy Lett. 2 (2017) 703–708. https://doi.org/10.1021/acsenergylett.7b00130.

[29] N. Zhang, N. Zaker, H. Li, A. Liu, J. Inglis, L. Jing, J. Li, Y. Li, G.A. Botton, J.R. Dahn, Cobalt-Free Nickel-Rich Positive Electrode Materials with a Core-Shell Structure, Chem. Mater. 31 (2019) 10150–10160. https://doi.org/10.1021/acs.chemmater.9b03515.

[30] Y. Tang, Y. Zhang, W. Li, B. Ma, X. Chen, Rational material design for ultrafast rechargeable lithium-ion batteries, Chem. Soc. Rev. 44 (2015) 5926–5940. https://doi.org/10.1039/c4cs00442f.

[31] Q. Liu, H. He, Z.F. Li, Y. Liu, Y. Ren, W. Lu, J. Lu, E.A. Stach, J. Xie, Rate-dependent, Li-ion insertion/deinsertion behavior of LiFePO4 cathodes in commercial 18650 LiFePO4 cells, ACS Appl. Mater. Interfaces. 6 (2014) 3282–3289. https://doi.org/10.1021/am405150c.

[32] S. Taslimi Taleghani, B. Marcos, G. Lantagne, Modeling and simulation of a commercial graphite–LiFePO4 cell in a full range of C-rates, J. Appl. Electrochem. 48 (2018) 1389–1400. https://doi.org/10.1007/s10800-018-1239-6.

[33] L. Laffont, C. Delacourt, P. Gibot, M.Y. Wu, P. Kooyman, C. Masquelier, J.M. Tarascon, Study of the LiFePO4/FePO4two-phase system by high-resolution electron energy loss spectroscopy, Chem. Mater. 18 (2006) 5520–5529. https://doi.org/10.1021/cm0617182.

[34] D.B. Williams, C.B. Carter, Transmission Electron Microscopy, Springer US, Boston, MA, 2009. https://doi.org/10.1007/978-0-387-76501-3.

[35] P.J. Goodhew, J. Humphreys, Electron Microscopy and Analysis, Third Ed. (n.d.).

[36] S.J. Pennycook, D.E. Jesson, High-resolution Z-contrast imaging of crystals, Ultramicroscopy. 37 (1991) 14–38. https://doi.org/10.1016/0304-3991(91)90004-P.

[37] M. Weyland, D.A. Muller, Tuning the convergence angle for optimum STEM performance, ArXiv. (2020).

[38] Q.D. Truong, M.K. Devaraju, T. Tomai, I. Honma, Direct observation of antisite defects in LiCoPO4 cathode materials by annular dark- and bright-field electron microscopy, ACS Appl. Mater. Interfaces. 5 (2013) 9926–9932. https://doi.org/10.1021/am403018n.

[39] S.Y. Chung, S.Y. Choi, T. Yamamoto, Y. Ikuhara, Atomic-scale visualization of antisite defects in LiFePO4, Phys. Rev. Lett. 100 (2008) 1–4. https://doi.org/10.1103/PhysRevLett.100.125502.

[40] E. Liberti, J.G. Lozano, M.A. Pérez Osorio, M.R. Roberts, P.G. Bruce, A.I. Kirkland, Quantifying oxygen distortions in lithium-rich transition-metal-oxide cathodes using ABF STEM, Ultramicroscopy. 210 (2020) 112914. https://doi.org/10.1016/j.ultramic.2019.112914.

[41] S. Ahmed, M. Bianchini, A. Pokle, M.S. Munde, P. Hartmann, T. Brezesinski, A. Beyer, J. Janek, K. Volz, Visualization of Light Elements using 4D STEM: The Layered-to-Rock Salt Phase Transition in LiNiO2 Cathode Material, Adv. Energy Mater. 10 (2020). https://doi.org/10.1002/aenm.202001026.

[42] S.D. Findlay, Y. Kohno, L.A. Cardamone, Y. Ikuhara, N. Shibata, Enhanced light element imaging in atomic resolution scanning transmission electron microscopy, Ultramicroscopy. 136 (2014) 31–41. https://doi.org/10.1016/j.ultramic.2013.07.019.

[43] T. Grieb, F.F. Krause, M. Schowalter, D. Zillmann, R. Sellin, K. Müller-Caspary, C. Mahr, T. Mehrtens, D. Bimberg, A. Rosenauer, Strain analysis from nano-beam electron diffraction: Influence of specimen tilt and beam convergence, Ultramicroscopy. 190 (2018) 45–57. https://doi.org/10.1016/j.ultramic.2018.03.013.

[44] S.E. Zeltmann, A. Müller, K.C. Bustillo, B. Savitzky, L. Hughes, A.M. Minor, C. Ophus, Patterned probes for high precision 4D-STEM bragg measurements, Ultramicroscopy. 209 (2020). https://doi.org/10.1016/j.ultramic.2019.112890.

[45] R. Huang, Y.H. Ikuhara, T. Mizoguchi, S.D. Findlay, A. Kuwabara, C.A.J. Fisher, H. Moriwake, H. Oki, T. Hirayama, Y. Ikuhara, Oxygen-vacancy ordering at surfaces of lithium manganese(III,IV) oxide spinel nanoparticles, Angew. Chemie - Int. Ed. 50 (2011) 3053–3057. https://doi.org/10.1002/anie.201004638.

[46] R. Huang, Y. Ikuhara, STEM characterization for lithium-ion battery cathode materials, Curr. Opin. Solid State Mater. Sci. 16 (2012) 31–38. https://doi.org/10.1016/j.cossms.2011.08.002.

[47] Y. Makimura, S. Zheng, Y. Ikuhara, Y. Ukyo, Microstructural Observation of LiNi 0.8 Co 0.15 Al 0.05 O 2 after Charge and Discharge by Scanning Transmission Electron Microscopy , J. Electrochem. Soc. 159 (2012) A1070–A1073. https://doi.org/10.1149/2.073207jes.

[48] G.A. Botton, Probing bonding and electronic structure at atomic resolution with spectroscopic imaging, MRS Bull. 37 (2012) 21–28. https://doi.org/10.1557/mrs.2011.336.

[49] G. Botton, S. Prabhudev, Analytical electron microscopy, Springer Handbooks. (2019) 345–453. https://doi.org/10.1007/978-3-030-00069-1_7.

[50] S. Muto, K. Tatsumi, T. Sasaki, H. Kondo, T. Ohsuna, K. Horibuchi, Y. Takeuchi, Mapping of heterogeneous chemical states of lithium in a LiNiO 2-based active material by electron energy-loss spectroscopy, Electrochem. Solid-State Lett. 13 (2010) 115–117. https://doi.org/10.1149/1.3439641.

[51] S. Muto, T. Yoshida, K. Tatsumi, Diagnostic nano-analysis of materials properties by multivariate curve resolution applied to spectrum images by S/TEM-EELS, Mater. Trans. 50 (2009) 964–969. https://doi.org/10.2320/matertrans.MC200805.

[52] M. Bosman, M. Watanabe, D.T.L. Alexander, V.J. Keast, Mapping chemical and bonding information using multivariate analysis of electron energy-loss spectrum images, Ultramicroscopy. 106 (2006) 1024–1032.

https://doi.org/10.1016/j.ultramic.2006.04.016.

[53] M. Newville, Fundamentals of XAFS, Rev. Mineral. Geochemistry. 78 (2014) 33–74. https://doi.org/10.2138/rmg.2014.78.2.

[54] A. Gaur, B.D. Shrivastava, H.L. Nigam, X-Ray Absorption Fine Structure (XAFS) Spectroscopy – A Review, Proc Indian Natn Sci Acad Spl. Issue, Part B. 79 (2013) 921–966.

[55] V. Petkov, Pair Distribution Functions Analysis, Charact. Mater. (2012) 1361–1372. https://doi.org/10.1002/0471266965.com159.

[56] B. Ravel, Quantitative EXAFS Analysis, (2016).

[57] T. Sasaki, T. Nonaka, H. Oka, C. Okuda, Y. Itou, Y. Kondo, Y. Takeuchi, Y. Ukyo, K. Tatsumi, S. Muto, Capacity-Fading Mechanisms of LiNiO[sub 2]-Based Lithium-Ion Batteries, J. Electrochem. Soc. 156 (2009) A289. https://doi.org/10.1149/1.3076136.

Chapter 2

Probing the Mysterious Behavior of Tungsten as a Dopant Inside Pristine Cobalt-Free Nickel-Rich Cathode Materials

Complete Citation:

Zaker, N., Geng, C., Rathore, D., Hamam, I., Chen, N., Xiao, P., Yang, C., Dahn, J.R., Botton, G.A., "submitted to Advanced Functional Materials journal" (2022)

Acknowledgements

The McMaster authors would like to thank NSERC for funding this research through a Discovery Grant. The electron microscopy work was carried out at the Canadian Centre for Electron Microscopy (CCEM), a facility supported by the Canada Foundation for Innovation through the Major Science Initiatives program, NSERC and McMaster University. N.Z., G.A.B. and N.C. are also thankful for the resources provided by the Canadian Light Source. Part of the research described in this paper was performed using beamlines HXMA and BXDS at the Canadian Light Source, a national research facility of

the University of Saskatchewan, which is supported by the Canada Foundation for Innovation (CFI), the Natural Sciences and Engineering Research Council (NSERC), the National Research Council (NRC), the Canadian Institutes of Health Research (CIHR), the Government of Saskatchewan, and the University of Saskatchewan. The Dalhousie authors thank NSERC and Tesla Canada for funding their portion of the work and the Alliance grant.

Abstract:

Nickel-rich cathode materials with small amounts of tungsten dopants have attracted extensive attention in recent years. However, the chemical state, crystalline form, compound chemistry, and location of W in these layered structured cathodes are still not well-understood. In this work these missing structural properties are determined through a combination of macro-, to atomic-sensitive characterization techniques and density functional theory. W-doped $LiNiO_2$ particles, prepared with mechanofusion and coprecipitation methods, were used to probe changes in the structure and location of W-species. The results indicate that W is mainly distributed on the surfaces of secondary particles and in the grain boundaries between primary particles, regardless of the doping method. Electron energy loss spectroscopy mapping confirms the simultaneous presence of W, O, with and without Ni in the grain boundaries as well as some W- and O-rich regions on the very surface. The W-rich areas inside the grain boundaries are found to be in two forms, crystalline and amorphous. This paper suggests the presence of kinetically stabilized-$Li_{4+x}Ni_{1-x}WO_6$ (x=0, 0.1) with the possibility of $Li_xW_yO_z$ phases in $LiNiO_2$ which are consistent with electron microscopy, X-ray absorption and diffraction data. The multiple roles of W in this complex microstructure are discussed considering the W distribution.

Keywords:

Engineered complex cathode structures; Ni-rich cathode; Tungsten dopant; Mechanofusion; Coprecipitation; Li-ion battery.

2.1 Introduction

High energy density lithium-ion batteries are the best potential energy storage system for electric vehicles and to support a more sustainable and green future for the planet [1–4]. To fulfill commercial expectations, these batteries require higher capacity, cyclic lifetime, rate capability, and thermal stability [5–8]. Besides many attempts to enhance the main components in Li-ion batteries by discovering new materials and adjusting currently available materials, the cathode is still the main limiting factor for energy density and is the highest price component of a Li-ion cell [1,9,10]. Layered cathode materials are common in commercial applications. In these materials, higher levels of nickel lead to higher energy densities [11,12]. However, Ni enrichment brings several problems, such as decreased cycling life span, safety, and thermal stability, leading to quicker failure [2,13–15]. A new generation of optimized engineered complex cathode structures have emerged, utilizing ultra-high Ni cathode materials, along with various methods like doping, core-shell structures, and coatings. These approaches can be categorized as either bulk or surface modification strategies, with the ultimate goal for all being to stabilize the active material and/or to increase its lifetime during charge-discharge cycling [4,16–24].

Atomic doping is one of the most conventional methods to alter the cathode host crystal and reinforce its structure [19]. In this regard, tremendous work has been done to identify the best dopant candidates and some cations with a high-valence state have drawn significant attention [13,25–27]. Using high oxidation state cations like Ti^{4+}, Zr^{4+}, Ta^{5+}, Mo^{+6}, W^{+6}, etc., would stabilize the Ni-rich cathode structures, alleviate Jahn-Taller active

elements (Ni^{+3}), suppress the diffusion of Ni^{2+}, protect cathode from side reactions with the electrolyte, or prevent undesirable phase transformation [17,28–30]. Lately, a family of W-doped Ni-rich cathode materials has demonstrated significantly improved LIB performance, as well as thermal and structural stabilities [31–33]. These recent studies have pointed out a few general effects of W on the behavior of LIBs and proposed some hypotheses as to what drives the observed enhancements. However, no comprehensive investigation has been conducted thus far to experimentally validate some of the hypotheses found in the literature. The high-valence charge and the complex electronic configuration of W in comparison with other common cation dopants, make the prediction of its role in the layered structure more complicated [34]. Therefore, understanding the W role would require identifying the location and distribution of W in bulk or surface, its effect on the structure of the layered material after synthesis, and the presence of possible W-phases inside the Ni-rich cathode structure.

In recently published papers [34–36], the general aspects of performance enhancement and structural modification have been the focus of discussion. From our previous work [34–36], a Ni-rich cathode material with only 1%W dopant showed the best cycling behavior and fracture resistance among the tested materials as compared to other doping levels. It is worth mentioning that based on our previous paper, the optimum heat treatment temperature to reach a better W-enriched structure and some level of heterogeneity regarding the W distribution in the host structure have been reported [36]. To better understand the role of W in battery performance, this article presents in-depth characterization results and therefore reveals the preferred location of W, its forms as well as new possible W-variants in the doped-$LiNiO_2$ cathode materials. For this purpose, both X-ray-based and electron-based characterization techniques, as well as modeling, have

been used. These characterization techniques, alongside simulation and fitting of experimental data, provide sufficient information to predict and experimentally identify the location of W inside the cathode. Our results show that W is detected within the grain boundaries of the secondary particles and forming a thin layer, few nm thickness, on the edge of primary particles adjacent to these grain boundaries. Additionally, W is also found on the surface of secondary particles. As will be discussed in detail below, W-rich compounds which contain Ni with chemical composition $Li_{4+x}Ni_{1-x}WO_6$ (x=0 and 0.1 which are kinetically stabilized compounds) along with the probability of $Li_xW_yO_z$ phases, with the preferred concentration on the top surface and inside the grain boundaries of LNO structure, play a protective layer role as well as stress absorber medium, respectively.

2.2 Results and discussions

2.2.1 SXRD and PDF

The synchrotron-based powder XRD (SXRD) data for LNO doped with different amounts of W is illustrated in Figure 2-1(a). The patterns quantification in Table 2-1 shows that both lattice volume and cation mixing (amount of Ni in the Li layer inside the LNO) are increased with increased W dopants. Both of these changes are consistent with the presence of more Ni^{2+}, with a larger ionic radius than Ni^{3+} in the transition metal (TM) sites, and in agreement with other published works [31–33].

As shown in Figure 2-1(b), for higher amounts of W, additional peaks can be observed at 2θ angles between 19° to 35°, which is consistent with either a lower symmetry structure in additional phases or with superlattice reflections in LNO. Additionally, the presence of a broad hump in the scattering distribution around 19° to 35° in doped materials suggests the existence of an amorphous phase. However, in the LNO_ pristine sample, the detection of a weak hump might be caused by the capillary tube scattering.

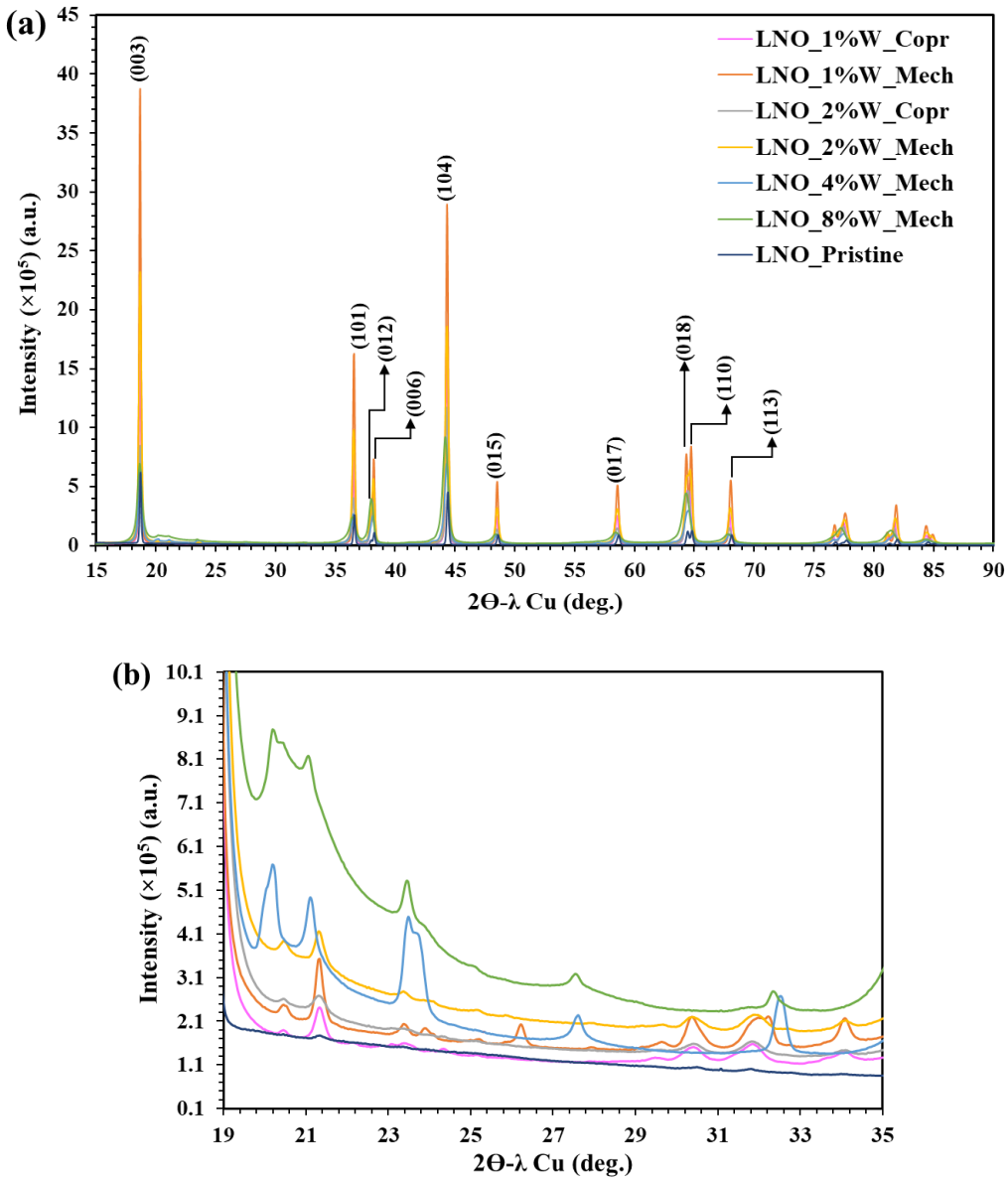

Figure 2-1 (a) SXRD patterns for pristine LNO and W-doped LNO (1%,2%,4%, and 8%W) prepared with mechanofusion, and W-doped LNO (1% and 2%W) prepared by coprecipitation. (b) The emerging tiny peaks in the range of 2Θ between 19° to 35° as well as the presence of a broad "hump" indicate an amorphous phase.

According to Figure 2-1(a), the major peaks can be indexed with high precision using the α–NaFeO2 ($R\bar{3}m$) structure [37]. For lower dopant amounts, namely LNO_1%W_mech, a clear separation between the (006), (012) and (018), (110) peaks, along with the higher

intensity of the (003) peak, are consistent with a clear layered structure. The ratio of $\frac{I_{(003)}}{I_{(104)}}$, identified as the R-value, has been used to track the amount of cation mixing inside the layered structure. Based on the literature, values below 1.2 are indicative of undesirable cation mixing due to more disordering or the formation of inactive cubic phase of LNO in the layered structures, which reduces electrochemical performance [38–40]. Our results show that the R-value decreased from LNO (~1.37) to 1%W (~1.34) and to 8%W (~0.76), indicating higher levels of cation mixing in the higher W-doped LNO structures and for samples prepared by coprecipitation.

Rietveld refinement of the patterns provides a much more accurate way of calculating the amount of Ni in Li layers sites, as presented in Table 2-1. The phase fractions of the Li_4NiWO_6 (see further below), the lattice parameters of LNO and the atomic occupancy of Li and Ni in Li sites were refined, and the R-value was extracted directly from the raw XRD patterns. In general, the absence of the (003) peak is consistent with the Fm(-)3m phase rather than the layered structure [15]. In Figure 2-1(a), the intensity of the (003) peak was significantly reduced in W-rich structures. Work in the literature suggested that this could be due to the presence of a rock salt/spinel phase based on electron diffraction patterns, caused by the presence of W in the structure of Ni-rich NMC ($Li\ Ni_x\ Co_y\ Mn_{1-x-y}\ O_2$) [31,33]. As shown below, however, the changes induced by the presence of W alters the local symmetry at the edge of particles where W is detected (see section 2.2.2). Also, the peak broadening noticeably increased with increasing the W content. This effect could either be caused by higher lattice strain induced by W, if present in the lattice, or by smaller particle size, as reported by other researchers [33]. Our previous work [36] showed that higher levels of W-doping in LNO materials generates smaller primary particles or, in other words, there are more grain boundaries inside their secondary particles.

Table 2-1 Crystallographic and phase information for LNO and other W-doped LNO materials based on the Rietveld refinement. The R_w% value is a goodness of fit parameter for the Rietveld refinement. The R-value is the ratio of the (003)/(104) peak intensities.

Materials	Phases Wt. fractions %		R_w%	Lattice parameters in LNO			Atom's occupancy in LNO		R-value
	Li_4NiWO_6	LNO		a [Å]	C [Å]	Volume [Å^3]	Li1	Ni1	
LNO_Pristine	0	100	3.86	2.87404	14.18384	101.463	0.982	0.018	1.37
LNO_1%W_Mech	0.652	99.348	6.33	2.87672	14.20978	101.839	0.973	0.027	1.34
LNO_2%W_Mech	0.686	99.314	7.33	2.87949	14.20191	101.979	0.951	0.049	1.25
LNO_4%W_Mech	6.645	93.355	8.85	2.88166	14.19745	102.1	0.889	0.111	0.98
LNO_8%W_Mech	7.733	92.267	11.62	2.89002	14.21934	102.852	0.82	0.18	0.76
LNO_1%W_Copr	0.679	99.321	6.7	2.88239	14.20709	102.221	0.922	0.078	0.99
LNO_2%W_Copr	0.818	99.182	10.28	2.88343	14.19265	102.191	0.898	0.102	0.72

According to Figure 2-1(a), for the higher W content (e.g., 8% W) material, the (110) peak shifted to lower angles, which could be ascribed to there being a higher amount of larger radius ions in the TM planes in the W-rich samples. On possible explanation for this is the presence of more Ni^{2+} (0.69 Å) with larger radii than Ni^{3+} (0.56 Å) in doped materials. Some of the previous literature suggested that the W^{6+} ions tend to occupy the TM sites and reduce some of the Ni^{+3} to Ni^{2+} ions to maintain charge balance, which inevitably increases cation mixing due to the similar ionic radii of Ni^{2+} and Li^{+} (0.72 Å). In our DFT work, we considered three different scenarios to maintain the charge balance when W^{+6} is in the LNO structure: 1) one Ni^{3+} vacancy for each W^{+6}, 2) three atoms single valence reductions by formation of three Ni^{2+} ions with and without their replacement in Li sites, and 3) formation of three Li^{+} vacancies. However, our DFT calculations show that none of

these configurations is energetically favorable. Additionally, the uniform presence of W in the LNO could not be entirely validated by the EXAFS data analysis, which will be discussed in section 0.

Other investigations indicated that the presence of XRD peaks in the range of 20° and 35° (2Θ range based on $\lambda_{CuK\alpha}$) originated from the ordering in the TM layers with Li_2MnO_3-type structure. For the Li_2MnO_3-type structure, different layer stacking along the c-direction might be possible, leading to various space groups such as C2/m, C2/c, and $P3_112$. However, the C2/m system is more energetically favored (albeit by small margin) and results in a better fit for the Li_2MnO_3-type structure [41]. Other work also reported the presence of a tiny broad peak at larger angles close to the (003) peak possibly arising from $[\sqrt{3}a_{hex} \times \sqrt{3}a_{hex}]$ R30° superlattice ordering resulting from stacking faults alongside the c-direction [42]. On the other hand, these extra peaks might originate from minute contents of different W phases or variants present within the doped LNO particles as second phases. To validate this possibility, various probable W compounds were considered either based on the DFT calculations (predicting which phases are energetically and thermodynamically favored) or based on existing W compounds, accounting for the combination of elements (W, O, Li, Ni) and similar space groups (C2/m, C2/c, Cm,…) to the Li_2MnO_3-type structure that were used above to fit the tiny peaks in XRD patterns.

Li_4NiWO_6 and $Li_{4.1}Ni_{0.9}WO_6$, with C2/m and Cm space group symmetry, respectively, have been found to improve the fit quality of the XRD patterns beyond the bulk LNO phase. As demonstrated further below, this is also consistent with simulations to fit the XAFS modulations from the W atoms' environments in the doped materials. To confirm these results with the XRD refinement, the LNO together with either one or both of these phases were studied. Due to the similarity of XRD peak positions in these two W-variants,

especially between 20° and 35° (based on the $\lambda_{CuK\alpha}$) 2Θ range, the fitting residuals were considered for different scenarios. First, the fitting was carried out considering LNO with one of the compounds (either Li_4NiWO_6 or $Li_{4.1}Ni_{0.9}WO_6$) at a time, then considering LNO with both phases at the same time. While the fitting residues were relatively low and approximately similar in both cases, the concentrations yielded some unphysical outputs when fitting the peaks with both phases at the time. Based on this result and the similarity of the residues, the fitting of LNO with only one of the phases was considered. The results of fitting with LNO and Li_4NiWO_6 are represented in Table 2-1. While there is a quantitative improvement of the residuals of fit, it is also clear that a perfect match to the full series of SXRD peaks is not obtained as illustrated in Figure 2-6S (for brevity, the figure number will be followed by "S" for referring to figures in the supporting information, section 2.5) especially in lower W amount. This suggests a combination of phases or of changes in the structure induced by multiple effects that are not accounted for by a simple Rietveld refinement.

Further insight into the complexity of the doped material and how the main lattice of the LNO phase is affected can be obtained from PDF analysis. PDF analysis provides an average distribution of pairs of interatomic distances. This information would make it possible to detect if interatomic spacings and order change. By inspecting the short and medium spacing ranges, we can deduce that the average structure of the doped compounds (with the concentration of W used in this work) shows no detectable changes in the PDF (such as clear extra peaks) as compared to the pristine material (see SI document for completeness). These results agree with SXRD analysis due to the low concentration of W-variants inside the LNO.

2.2.2 STEM and EELS

High-resolution-STEM images of the doped samples in their pristine state, from both the mechanofusion process and coprecipitation synthesis, are shown in Figure 2-2(a-c). The contrast mechanism, in HAADF mode of detection, is related to the atomic number and the thickness of regions that are scattering electrons and thus the brighter areas denote heavier elements or thicker regions of the sample. These high-resolution images, Figure 2-2(a,b), mainly show the same apparent behavior at grain boundaries: two bright bands (mostly crystalline) separated by a dark region in between. Since W is the heaviest element inside these materials, based on the intensities in the images, the W-rich area would be located in those bright band regions. Because the dark areas could also imply a different thickness, a more detailed spectroscopic analysis with EELS is still required. From inspection, however, two conclusions can be drawn: 1) there is W diffusion along grain boundaries between the primary particles, very deep in the structure of secondary particles (this is more evident in Figure 2-4(a)), and 2) W is located at grain boundaries but it is not clear if W is also in the structure, given that the concentration of W away from the boundaries is lower. In other words, these images demonstrate that W diffuses through the secondary particles and is mainly located inside the grain boundaries. Further analysis using Fourier Transform (FT) and crystal distance matching was performed to thoroughly understand the high-resolution atomic lattice images, as will be discussed in the following.

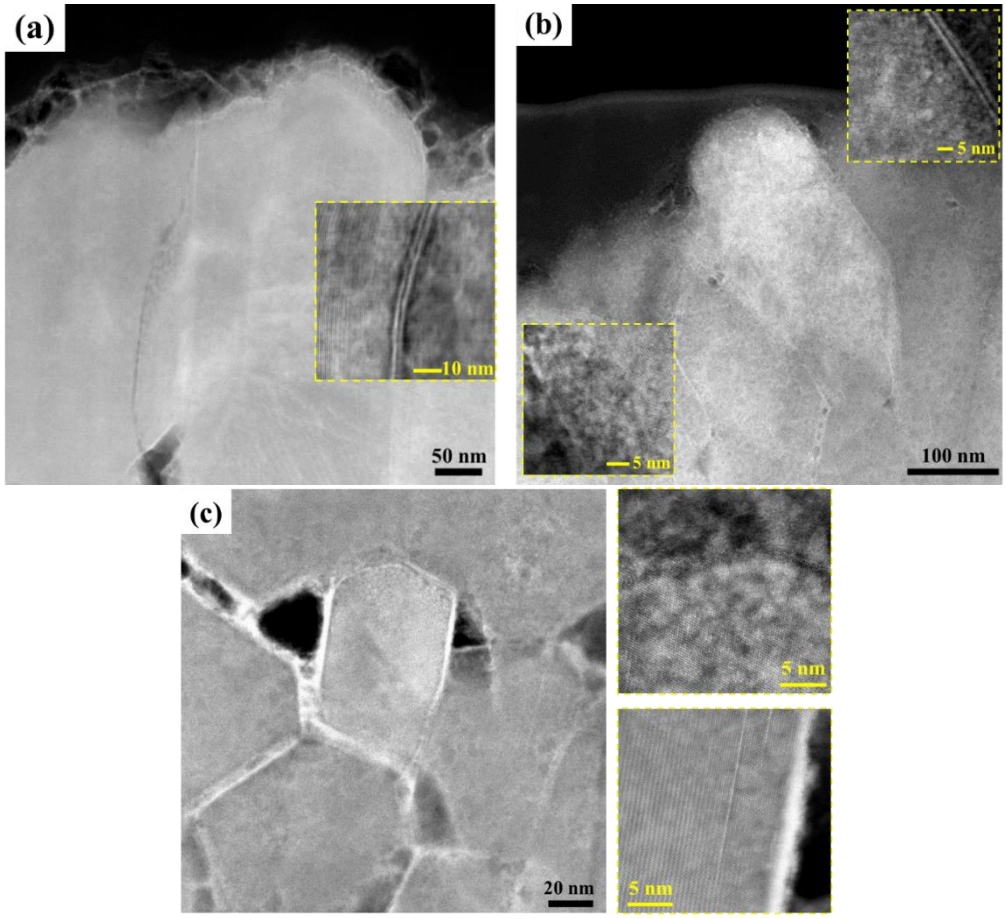

Figure 2-2 The HAADF images of (a) LNO_1%W_Mech, (b), and (c) LNO_1%W_Copr from the top and the middle part of the secondary particle, respectively. Each figure also includes higher magnification images of the grain boundaries.

Detailed atomic resolution imaging of a primary particle (in the core part of the secondary particle, Figure 2-3), near a grain boundary and including a region further away, was carried out in order to probe in detail the changes to the structure induced by the presence of W. First, an area further from the grain boundary was selected, marked “I” in Figure 2-3(a). The FT calculation providing a local numerical diffraction pattern and the intensity profiles from two different atomic planes confirm the <010> zone axis of LNO for region “I” is presented in Figure 2-3(b, c). Based on the line profile (Figure 2-3(c)), one can notice the high-intensity TM planes and troughs corresponding to the Li planes. However, within

the Li planes where there should be very clear intensity minima since the Li does not contribute to the HAADF signal, there are additional intensity maxima (marked by orange arrows), locally consistent with cation mixing corresponding to either Ni or possible W atoms. Since the concentration of W is low and the intensity within the Li layers is quite uniform within these planes, this suggests that, in these regions, Ni would be present within the Li layers, consistent with results from structure refinement where some cation mixing is deduced. In the <010> zone axis, the distances between the atomic columns from the line profiles match well with the spacing between the Li and Ni sites, as shown in Figure 2-3(d). In other areas, however, no cation mixing is detected, and the pristine layered structure is visible, which is shown in the purple dotted line box in Figure 2-3(a). This also suggests that this effect is not an electron beam propagation artefact due to the channeling of the electron beam to the TM columns, since the thickness of the two regions would be very similar.

Very clear from Figure 2-3(a) is also a very bright crystalline region (identified as region "II") at the edge of the grain, adjacent to the grain boundary. Based on the intensity of the atomic columns, it is expected that this is due to the presence of W. As will be explored further in the discussion of the EELS mapping, this W-rich area also contains O and Ni. The image of the numerical diffraction with FT from this bright area in Figure 2-3(b) does not show layered structural phase symmetry. Prior literature has shown that a spinel phase (cubic symmetry) which only originates from cation mixing [43,44] can appear after electrochemical cycling on the edge of primary particles. Here, our results illustrate that, although there is cation mixing between the Ni and Li atoms, the precise measurements with EELS (shown further below) reveal more information about the concentration of W

in such non-layered phase areas and demonstrate the presence of some tungsten phase variants on the very surface of the primary particles.

XRD refinement results (as well as the subsequent validation by EELS mapping and XAFS fitting) indicate a better fit to the pattern with the presence of Li, Ni, W, and O phase, which suggests that the crystalline bright area "II" could be either the stoichiometric compound Li_4NiWO_6 or its solid solution $Li_{4.1}Ni_{0.9}WO_6$. Further clarification is obtained from the high-resolution HAADF image through the numerical FT diffraction from region "II" (Figure 2-3(b)), which is perfectly consistent with the $<\bar{3}\bar{1}1>$ zone axis direction of either of these two W-compounds. Furthermore, from the line profiles and the calculated atomic distance between W and Ni atoms (Figure 2-3(c,d)), the plane spacings are in good agreement with the expectations from this zone axis. For this comparison, the spacing between the W and Ni atomic positions have been considered since they are the most visible sites from the HAADF detector. However, as demonstrated in Figure 2-3(d), these W variants show almost identical atomic distances in this zone axis. It is therefore impossible to differentiate between them even by detailed local analysis. The stoichiometric compound Li_4NiWO_6 with C2/m symmetry has three shared sites (4g, 4h and 2d Wyckoff positions) for Ni and Li with Ni occupancies between 16% to 26% and a single site for W (2a Wyckoff position); however, in the solid solution of a general composition $Li_{4+x}Ni_{1-x}WO_6$ (in this specific case corresponding to a previously-identified compound with composition $Li_{4.1}Ni_{0.9}WO_6$ and Cm symmetry), there are four sites with the combination of Ni, Li, and W (site 1: W=99.1% and Li=0.9% with 2a Wyckoff position, site 2: W=0.5%, Ni=28.2% and Li=71.3% with 4b Wyckoff position, site 3: W=0.4%, Ni=7.7% and Li=91.9% with 2a Wyckoff position and site 4: Ni=12.7% and Li=87.3% with 4b Wyckoff position).

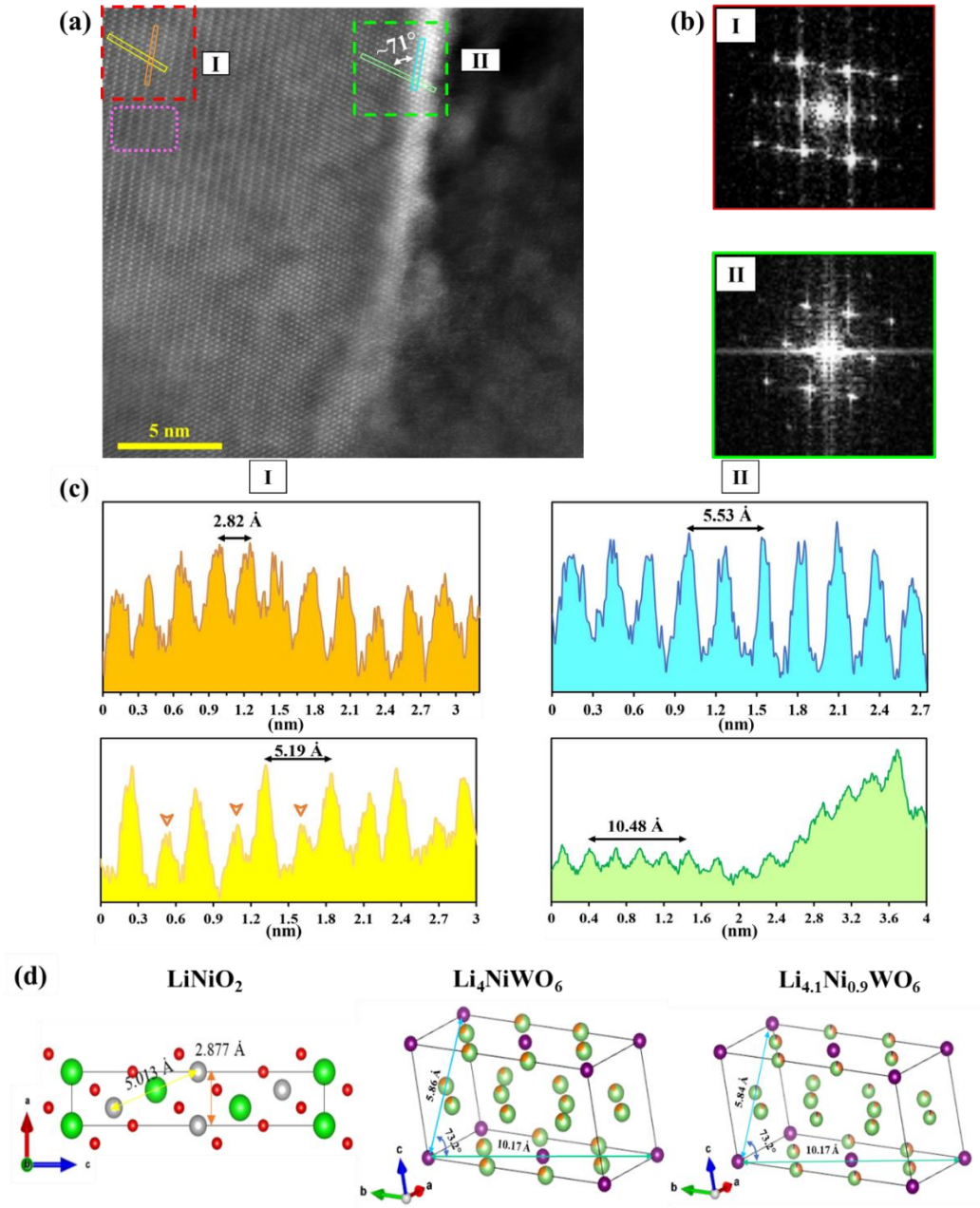

Figure 2-3 (a) The HAADF image of the LNO_1%W_Copr sample. Two areas, "I" and "II", with two different atomic lines and angles, are marked. (b) shows the FT calculations from each selected area. (c) The line profiles from each selected atomic line in (a), with the same color (the orange arrows represent the heavier atoms within the Li layer). (d) The 3D structure of the $LiNiO_2$, $Li_{4.1}Ni_{0.9}WO_6$, and Li_4NiWO_6 from the appropriate zone axis view with calculated atomic distances. Li, O, and W are in green, red, and purple colors, respectively. Ni is gray in the LNO and orange in the W-phases.

The low magnification EELS maps from different doped materials, regardless of doping methods (Figure 2-4(a,b)) reveal that W is mainly concentrated on the very surface of the primary and secondary particles as well as at the grain boundaries in between the primary particles. Also, the W concentration inside the deeper level of the secondary particle, especially in the grain boundary, seems to increase with more W dopant. These results are consistent with the previously presented XRD peak broadening since smaller primary particles provide more accessible pathways for W to reach inside the secondary particles through their grain boundaries. This reduction of primary grain size along with the presence of W in the grain boundaries, improve the strength of this family of doped structure and increase their resistance toward cracking [35]. Having W-rich areas on the surface of the secondary particles can play a protective role in reducing the direct contact between the Ni-rich cathode materials and the electrolyte. A second role of W, given this microstructure, in addition to strengthening the grain boundaries, would be acting as a damping medium for the cycling stress due to the presence of W-rich areas. The detailed experimental discussion regarding the protective role from side reactions during cycling, along with strengthening of the grain boundaries and damping cycling stress through the presence of W-variants, are out of this paper's scope and will be discussed in more depth in a follow-up work focused on the effect of W on the degradation mechanisms through electrochemical cycling. For in-depth characterization of the form and location of W inside the doped materials, higher magnification EELS mapping was implemented.

A high-magnification EELS map and the related Annular Dark-Field (ADF) image are presented in Figure 2-4(c) (as well as Figure 2-9S(a)), which illustrate that the W is noticeably present in regions within grain boundaries of the secondary particles with an amorphous structure. Additionally, the W signal is still apparent within a few nanometers

of the surface of the primary particles within the crystalline atomic arrangement of the grain. Furthermore, there are marked differences between the O K-near-edge structure of bulk areas and those containing W, visible in the pre-edge peak feature. This pre-edge peak is very clearly detectable in the inner parts of the primary particles and is consistent with the results for pure LNO, which has a sharp and very clearly visible pre-edge peak. In Ni-rich materials, the general expectation for the O K-edge peak's shape is the appearance of the pre-edge peak arising from the transition between O 1s and the hybridized state of O 2p with Ni 3d states. In addition, the other features over 534 eV are due to the transition from O 1s to the hybridized state of O 2p with Ni 4sp states. Based on the literature, changes in the crystal structure through cation mixing could substantially affect the hybridization state between TM 3d and O 2p bands, and induce changes in the O pre-edge peak [45]. In our case, the alteration in the mentioned hybridization state seems to be induced by changes in the chemical environment as a result of the W presence. The pre-edge peak intensity decreases from the core of particles (i.e. away from the grain boundaries) to the grain boundary until the pre-edge finally disappeared inside the grain boundaries where the shape is significantly different, as shown in more detail in Figure 2-9S(b) and Figure 2-10S(b). No spectroscopic evidence indicates an O K-edge consistent with WO_3. Based on Figure 2-9S(a) and Figure 2-4(c), although the pure oxygen signal mapping (i.e. a large energy range integrating the total edge signal) showed lower O content inside the grain boundaries, further investigation following Principal Component Analysis for noise reduction and Multiple Linear Least Square fitting (considering two different shapes of O peak, one with and another one without pre-edge (Figure 2-9S(c) and Figure 2-10S(c))) reveals that the O K-edge within the grain boundary has no pre-edge feature. An example of the quality of MLLS fitting results is illustrated in Figure 2-9S(d). Further evidence obtained from the

secondary particle, Figure 2-11S, also shows the presence of an approximately 10 nm thick region on the top of the surface with W- and O-rich layers without any Ni element. Moreover, Energy-Dispersive X-ray Spectroscopy (EDXS) maps were also acquired and are consistent with the segregation as detected with EELS (Figure 2-12S).

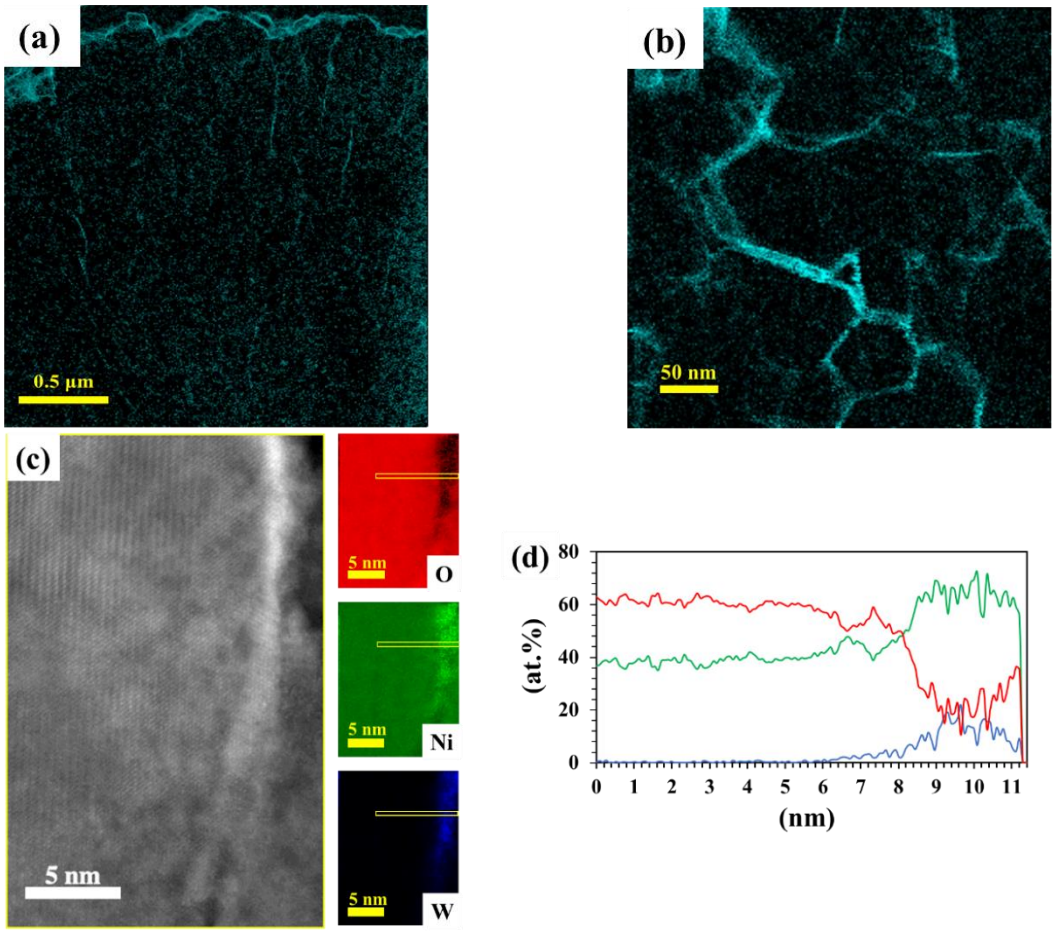

Figure 2-4 The EELS map of W for (a) LNO_1%W_Mech in total view and (b) LNO_1%W_Copr in the middle of the sample. (c) The ADF and spectrum images from one of the primary particles inside the LNO_1%W_Copr material, with assigned elemental distribution. (d) The line profile from the yellow line in (c).

The high level of noise in EELS maps and the line profiles is due to the use of a very low electron beam current in order to minimize radiation damage. As illustrated in Figure 2-4(d), the W, Ni, and O elements were detected near the primary particle perimeters,

which encouraged the authors to perform a complementary analysis in addition to the EELS measurement to provide further insights on the W phase/phases. XAFS analysis was utilized to fulfill this demand. The strengths of XAFS over EELS analysis are its better sensitivity to low concentrations and the ability to acquire the higher energy peaks of W. In EELS, only the tungsten M-edge, with its delayed and broad shape is accessible, but in XAFS, the W L_3-edge is easily captured.

2.2.3 XAFS analysis

The normalized XANES spectra of eight samples, shown in Figure 2-13S, reveal a double peak feature in all the doped W materials regardless of the doping amount (1%, 2%, 4%, 8%) and the doping approach. The energy position of the W L_3-edge in doped materials is nearly overlapping with the WO_3 reference, which was attributed to the expected oxidation state of tungsten (W^{+6}). In other research, the W L_3-edge peak in both WO_3 and WO_2 showed a single peak shape as well [46]. However, these double-peak shapes can result from either a distorted environment around the W or the coexistence of multiple W species inside the doped samples. To fit the XAFS data, two different hypotheses were considered as is discussed below.

As a first consideration, it was assumed that W is uniformly doped in the LNO structure, and these doped structures are described by considering different scenarios calculated by DFT. Among all doped structural assumptions, W occupies the Ni site with octahedral geometry. To balance the tungsten's extra charge and to maintain neutrality, several possibilities were considered, as discussed above, even though these were not energetically favorable [34] (i.e. (1) one Ni^{3+} or (2) three Li^{+} vacancies as well as (3) three reductions of Ni^{+3} to Ni^{+2} with and without exchanging position with 3 Li^{+}). In addition, an experimental comparison of the Radial Distribution Function (RDF) around Ni and W

atoms, based on EXAFS data derived from the Ni K-edge from pure LNO and the W L_3-edge from W doped LNO, was made to determine if these two distributions would clarify the same environment for the Ni and W species. In Figure 2-5(a), the RDF extracted from EXAFS modulations of the Ni K-edge, modeled with Feff simulations based on different hypothetical Ni sites, Ni1 (on a Li site) and Ni2 (on a Ni site) and the experimental data from the LNO material are demonstrated. The RDF peaks from Feff modeling can be used to identify the major differences between two Ni local structural environments, notably after the first two shells (up to ~3Å, identified as features "I" and "II"). The main difference between these two sites is the presence of features "III" and "V" which are exclusively specific for sites Ni1 and Ni2, respectively. The "V" feature is comparatively less practical than "III" since it is located at a higher R value and is influenced by the Debye-Waller effect in the experimental data. According to Figure 2-5(a), the experimental data can be described very well by the model with Ni only at Ni2 site and is congruous with the expectation based on structure refinement from XRD data showing low cation mixing. Considering these fingerprint features, the comparison between the two experimental RDF patterns was carried out as depicted in Figure 2-5(b). According to Figure 2-5(b), both materials reveal the same location for the first peak with good first shell match. However, the significantly weaker peak intensity of the "II" peak in the doped material, with respect to the second neighboring shell of W, indicates that the W atoms' 2^{nd} shell coordination is either incomplete or W is located at the surface site. Also, the missing "IV" and "V" peaks might be resulting from having large site disordering at the W occupied site, which is consistent with the "II" peak's low intensity. Consequently, the uniform distribution of W inside the Ni site of the LNO, cannot be experimentally justified.

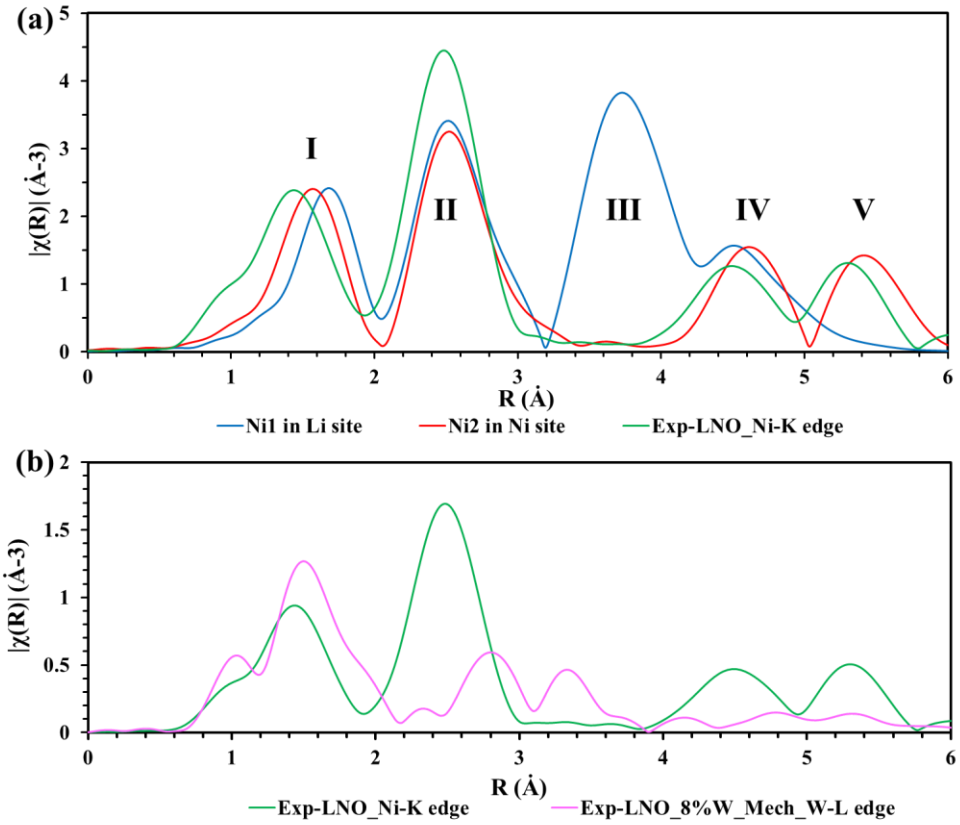

Figure 2-5 (a) The EXAFS results calculated by Feff modeling considering Ni-occupied Li site (Ni1) or Ni site (Ni2) and their comparison with the experimental data for pure LNO with respect to the Ni K-edge. (b) The comparison of the experimental EXAFS pattern for pure LNO and LNO_8%W_Mech regarding Ni K-edge and W L_3-edge, respectively.

Since the EELS maps demonstrate the presence of W within more localized areas and not simply uniform doping through LNO, a second configuration was investigated in which W-rich compounds being found inside the doped materials is assumed, and the impact on the consistency of the EELS and XANES was investigated. The compounds considered here are suggested based on DFT calculation or are previously published phases. Furthermore, four reference compounds (Li_2WO_4, $Li_2W_2O_7$, Li_4WO_5, and $NiWO_4$) were synthesized and examined through the same experimental methods, Figure 2-14S, to

compare data with the doped materials. Normalized XANES features were used for the linear combination fitting (LCF) analysis since the preliminary matching results from the 1st derivative XANES showed the same major answer as the normalized one. In the end, eight possible compounds were compared, with either different chemistry or crystal symmetry for the final fitting. All eight structures are shown in Figure 2-15S. The main spectral features considered for identifying the candidate phases are a double-peak shape in the XANES, presenting almost the same intensity ratio between the first and the second peak as doped samples' experimental data, or compounds containing simultaneously W, O, and sometime Ni elements in which by combining their individual XANES features, the best fitting toward the experimental data could be achieved. During the final fitting step (fitting the range -20 to 70 eV with respect to the absorption edge), whenever the edge energy E_0 difference was larger than +/-10 eV, that compound was eliminated since such a large discrepancy in the energy calibration is unlikely.

Comparing the XANES features of the eight phases (247 total possible combinations), the stoichiometric compound Li_4NiWO_6, and the solid solution $Li_{4.1}Ni_{0.9}WO_6$, presented the most similarities of their W edge with the doped materials. Though they are not thermodynamically stable, these two compounds seem kinetically favorable. The final fitting results and their phase weightings between two finalized LCF answers are displayed in the Table 2-3S.

The experimentally-resolved XANES white-line has two main features: 1) a double peak fine structure, and 2) a signal intensity trend with the lower energy peak stronger than the higher energy one. According to the simulations in Figure 2-16S, the double peak white-line structure and its intensity trend are reproduced by LCF fitting. However, the best fit does not perfectly overlap with the experimental data. The variance, specifically for the

relative intensity feature, could be driven by: 1) the subtle structural differences in the first shell W-O bond distances, bond angles, and the further beyond local structure environments between those actual W species in samples and the models which guided the XANES fitting, and/or 2) certain code-related defects in the XANES modeling. For these reasons, based just on XANES simulations, one cannot completely exclude the possibility of other coexisting W species besides these picked ones within the doped material structures. As discussed in the EELS sections, based on Figure 2-9S(a) and Figure 2-11S(e), there is clearly a lack of Ni element inside some W-rich areas. Considering several possible $Li_xW_yO_z$ compounds in the XAFS fitting, none of them has been selected to better match the spectra. This may originate from incomplete matches between these models and the actual $Li_xNi_yO_z$ compounds in the doped materials. The experimental data from the four mentioned reference compounds have been considered for LCF analysis to investigate this effect further. According to Figure 2-17S, the best fittings in the presented doped samples show a calculated phase weight of more than 0.84 for the Li_4WO_5 reference phase. However, the best match between the experimental and LCF results in LNO_1% W_Mech, considering only these four reference compounds, does not seem entirely enough to describe all the possible W species inside the rest of the doped samples. On the other hand, the Li_4WO_5 reference compound was not a single phase based on our powder XRD data. Therefore, to consider this compound as a potential candidate through the final XANES modeling (based on the crystal structure files), phase identification from XRD analysis and then separate XANES modeling have been made to validate which of the identified phases would be a better representative of this reference compound. As can be seen in Figure 2-18S, two Li_4WO_5 phases, with P-1 and Fm-3m space groups, reveal double peak XANES features. However, none of the simulations of these two phases could

completely reproduce the full experimental features: the correct intensity ratio of the first two peaks, and the features at higher energy of the Li_4WO_5 reference compound. This mismatch could be due to the discrepancies between the XANES experiments and fitting for either of these two considered Li_4WO_5 models. We can therefore conclude that a combination of W-rich phases (with and without Ni) would be required to explain the XANES features through fitting. Some possible factors contributing to these discrepancies are the unknown relative fraction of phases with Ni and without Ni, as well as the amorphous nature of the Ni-deficient phase due to the changes this would generate on the XANES.

The following reactions present the energetically favorable products regarding the presence of a deficient (2.1) or sufficient (2.2) amount of Li source in the environment.

$$Li_4NiWO_6 + 16\ Li_{1-1/32}Ni_{1+1/32}O_2 + \frac{1}{2}\ O_2 \rightarrow \frac{35}{2}\ LiNiO_2 + Li_2WO_4 \qquad \Delta E = -1.63eV \qquad (2.1)$$

$$Li_4NiWO_6 + \frac{1}{2}\ Li_2O + \frac{1}{4}O_2 \rightarrow LiNiO_2 + Li_4WO_5 \qquad \Delta E = -1.16eV \qquad (2.2)$$

For the first reaction, the contact between the inner side of the LNO particle with excess Ni (1/32) in the Li layer, and the surface of the Li_4NiWO_6, is considered. In both reactions, the entropy of O_2, which depends on pressure and temperature, was not taken into account for ΔE.

On the one hand, those W-rich regions between the primary grains might lack access to sufficient oxygen or Li sources to form more stable compounds. On the other hand, the heat treatment temperature here was above the melting point of the $Li_xW_yO_z$ compounds, and if they were produced at the beginning, they would melt and therefore be able to diffuse through the grain boundaries of the secondary particles and after that react with the LNO.

Then the Ni/W ratio in those small gaps would be much different from the synthesis condition, making these $Li_{4+x}Ni_{1-x}WO_6$ compounds metastable. Other studies showed that the essential parameters for synthesizing Li_4NiWO_6 were the amount of Ni/W ratio as well as the extra amount of precursor combination (Li_2CO_3, NiO, and WO_3) for eliminating the Li deficiency [46]. Furthermore, under high temperature and low O_2 partial pressure during synthesis, the $\Delta G=\Delta E-T\Delta S$ could turn positive.

It is worth noting that the heterogeneous distribution of W and the presence of W-containing compounds, regardless of used synthesis methods in this research, reached the same results. However, further investigation on the cycled particles demonstrated that the high amount of porosities in coprecipitated particles which are visible in Figure 2-2(c) and Figure 2-4(b), made these particles more vulnerable to electrolyte infiltration and faster capacity degradation. An unoptimized protocol causes this effect for our coprecipitated samples, which are discussed in more detail in our future work.

2.3 Conclusion

The role of W in the crystalline structure and its elemental distribution on cathode materials when used as a dopant in $LiNiO_2$ was investigated using electron microscopy, X-ray scattering, and X-ray spectroscopy methods. Synchrotron-based X-ray diffraction analysis showed the appearance of minor peaks consistent with the additional presence of minor fractions of the stoichiometric compound Li_4NiWO_6 or the solid solution form $Li_{4+x}Ni_{1-x}WO_6$ consistent with the $Li_{4.1}Ni_{0.9}WO_6$ phase in doped $LiNiO_2$. However, not all minor features can be fully explained by structural refinement of the powder patterns with these phases. Synchrotron-based pair distribution function analysis revealed no significant structural differences induced by doping. Electron microscopy analysis with STEM imaging along with numerical diffraction of atomic-resolved images from nanometer scale

areas and electron energy loss spectroscopy, however, showed very clearly the presence of W in two main distinct types of regions: at grain boundaries and in their proximity on the surfaces of primary particles, as well as, on the surface of secondary particles. Within crystalline regions at the surface of primary particles, the W presence within a few ~1-3 nm of the grain boundaries was deduced and showed a pattern consistent with either Li_4NiWO_6 or $Li_{4.1}Ni_{0.9}WO_6$ phase structure. Detailed high-resolution EELS analysis mapping also provided more thorough information regarding the spatial distribution of W, demonstrating that this element was mostly in crystalline regions on the primary particles' perimeter (together with Ni) and within grain boundaries of the secondary particles where W-rich amorphous phases (sometime without Ni) were also found, thus indicating the presence of $Li_xW_yO_z$ compounds at the center of the boundaries. Additionally, these $Li_xW_yO_z$ compounds might also be available on the very surface of the secondary particles. Therefore, W was found to propagate during the synthesis along the grain boundaries, well within the core of the secondary particles, even if WO_3 had been initially placed on the surface of the particles. From the spatially resolved spectroscopic mapping of the O K-edge, the bonding environment of oxygen atoms at the grain boundaries was different and not consistent with WO_3. Spectral fitting of the W L_3-edge XANES indicated that the spectral features could not be solely explained with the $Li_{4+x}Ni_{1-x}WO_6$ phases (x=0 and 0.1) but must contain other compounds, such as $Li_xW_yO_z$ phases as evident from EELS. Due to different environmental conditions inside the grain boundaries and the surface of the primary particles, these metastable $Li_{4+x}Ni_{1-x}WO_6$ phases (x=0 and 0.1) in their bulk form, might be stabilized and kinetically favored. These results demonstrated that W played a significant role through its presence in the grain boundaries rather than the minor structural modifications of the bulk phases. This is very important from a mechanical strengthening

perspective since the most common fracture type in the Ni-rich cathode materials is intergranular cracking. The presence of W in grain boundaries increased the doped material's total resistance to cracking initiation and growth, making these series of cathodes suitable for use due to their longer life and higher capacity. This complex microstructure with W-rich areas at the surface of secondary particles and within grain boundaries, therefore, suggests that W might play multiple roles, protecting the surfaces from side reactions, strengthening grain boundaries, and providing a damping medium from stresses occurring during cycling. These effects will be discussed in more detail in a follow-up publication.

2.4 Experimental section

2.4.1 Synthesis procedures

In this work, two different synthesis methods, mechanofusion (a dry particle fusion method) and coprecipitation in a Continuously Stirred Tank Reactor (CSTR), were used to dope W within the cathode. These two different approaches were selected to fully understand the tungsten's behavior as a dopant, regardless of the synthesis method. Mechanofusion was conducted using a spinning speed of 2400 rpm for 60 minutes. During this process, a commercial $Ni(OH)_2$ with a primary particle size of approximately 15 μm was coated with a nano-sized (less than 100 nm) WO_3 powder from Sigma-Aldrich. 50 g of $Ni(OH)_2$ was loaded inside the mechanofusion bowl in addition to 1.263, 2.552, 5.210, and 10.873 g of WO_3 to reach 1, 2, 4, and 8 mol% of W in LNO, respectively. On the other hand, $(Ni_{1-x}(OH)_2)_{0.98} \cdot (NiWO_4)_{0.01}$ and $(Ni_{1-x}(OH)_2)_{0.96} \cdot (NiWO_4)_{0.02}$ precursors having W/(Ni+W) molar ratios of 0.01 and 0.02 were synthesized using the coprecipitation method via the CSTR. The synthesis steps were similar to those in the study conducted by Van

Bommel et al [47]. Two aqueous solutions were prepared containing 400 mL of 2.0 M $NiSO_4$ in addition to either 100 mL of 0.0808 M or 0.1633 M $NaWO_4$ for the former and latter precursors, respectively. More details regarding the aqueous solution, reactor temperature, stirring speed, and other processing parameters have been explained in the authors' previous work [36].

In the end, all the precursors from the mechanofusion and coprecipitation methods were ground with $LiOH{\cdot}H_2O$ (molar ratio of Li to (Ni + W) = 1.02/1). After this grinding step, the blended powders were placed under an oxygen flow at a preheated temperature of 480°C. Next, these preheated batches were ground again to reach a uniformly homogenized mixture. For the heating steps under oxygen flow, the ground powder particles were heated at 480 and 800°C for 2 and 20 hours, respectively. Although different calcination temperatures were used in our previous studies, the present paper only focuses on the optimum temperature results at 800°C [36]. Finally, pure LNO and W-doped LNO with 1, 2, 4 and 8% W were synthesized and used for other characterization techniques as reference materials. The higher W content samples (4% and 8%) were used as references to extend the structural investigation although there are no benefits to these concentrations from a performance point of view. For the sake of brevity and clarity, two labels will be used in this manuscript whereby "Mech" stands for mechanofusion and "Copr" indicates coprecipitation. For reference purpose, the pure LNO was subjected to the same heat treatment steps with the exception of the heating temperature in the second step which was set to 700°C.

2.4.2 XRD and PDF

Synchrotron XRD was conducted on the high-energy wiggler beamline of the Brockhouse X-ray Diffraction and Scattering sector at the Canadian Light Source (CLS) in Saskatoon,

Canada, for meticulous crystallographic analysis. The selected energy was 30.3383 keV (λ=0.4087 Å), and a nickel powder was utilized for detector calibration. All the powder samples were placed inside polyimide capillaries. All the angles in the XRD data were modified based on $\lambda_{CuK\alpha}$ for normalization with respect to the literature.

In addition, pair distribution function (PDF) analysis was performed on the same synchrotron beamline, in which an X-ray energy of 65 keV was employed to acquire a higher magnitude wave vector, Q ($Q = 4\pi\sin\Theta/\lambda$)[48]. This setting reaches a reasonably high Q_{max} (26 A^{-1}) and results in sharp peaks in the PDF.

2.4.3 Scanning transmission electron microscopy and analytical electron microscopy

We employed Scanning Transmission Electron Microscopy (STEM) and Electron Energy Loss Spectroscopy (EELS) for detailed spectroscopic analysis. A ThermoFisher Scientific (TFS) Helios G4 plasma-focused ion beam (PFIB) was used to create the ultra-thin samples required for these techniques. The samples were first coated with a very thin layer of carbon to reduce the charging effect in scanning electron microscopy (SEM) imaging mode, then two more layers of carbon and tungsten were added to the top surface in order to protect the surface structure of the particles from potential ion beam damage during the milling and lift-out procedures. The protective tungsten layer was applied due to its high resistance under ion milling. This step does not influence the amount of W inside the doped samples, as we demonstrated by analyzing non-doped samples prepared with the same coating conditions, which resulted in no detection of W even in trace concentration in thin lamella. All the STEM images were acquired at 200 keV incident electron energy using a high-angle annular dark-field (HAADF) detector within an FEI Titan 80-300 equipped with aberration correctors for the probe and imaging lenses. The convergence semi-angle in

STEM was 19.1 mrad. EELS data was acquired in STEM mode with a collection angle of 55 mrad, and a direct electron detector Gatan K2 Summit® was used to improve the quality of EELS signals, especially at low beam current (to reduce electron beam irradiation damage). To reduce the noise level on the EELS maps, Principal Component Analysis (PCA) was utilized. In addition, more detailed EELS features fitting was carried out using Multiple Linear Least Squares (MLLS) to separate spectroscopic maps based on different peak shapes of the O K-edge. Energy-Dispersive X-ray spectroscopy (EDXS) maps were obtained on a TFS Talos 200X fitted with a Super-EDS detector (results shown in Supporting Information).

2.4.4 X-ray absorption fine structure (XAFS)

The XAFS data acquisition was carried out on the Hard X-ray Micro-Analysis (HXMA) beamline at the CLS. The HXMA photon source is a superconducting wiggler insertion device running at 1.9 T, and energy selection was performed based on the W L_3- and Ni K-absorption edges with a Si (111) and (220) crystals monochromator, respectively. XAFS data were collected in both transmission mode and fluorescence modes using Oxford straight ion chamber detectors (100% filled with He) and 13 element Ge detector with Soller slits and Cu filter (several layers of Al foil), respectively. The same powder-form WO_3 model compound that was utilized for doping was set between the I_1 and I_2 ion chambers downstream of the sample for in-step energy calibration for each tungsten XAFS scan.

2.4.5 DFT calculations

Density Functional Theory (DFT) was exploited to deduce crystallographic information for the different W-doped $LiNiO_2$ structural scenarios and calculate the most thermodynamically-stable W compound during synthesis. DFT was also employed to

assess separate crystallographic information regarding other possible W-compounds with almost identical energy.

The Vienna Ab initio Simulation Package (VASP) was used to conduct these calculations with Projector Augmented Wave (PAW) pseudopotentials [49–52]. The exchange and correlation terms were defined by the Strongly Constrained and Appropriately Normed (SCAN) functional[53]. An energy cutoff of 520eV was considered for the plane-wave basis. The Brillouin zone was sampled with less than 0.05 $Å^{-1}$ k-point spacing. All the calculations were spin polarized and adopted ferromagnetic spin orderings.

2.5 Supporting information

2.5.1 PDF analysis

PDF is presented on two space ranges (Figure 2-7S(a,b)) for clarity in the discussion and better visualization. The first set corresponds to the local order up to 12Å (Figure 2-7S(a)) and the second set is shown for the intermediate range between 12 Å to 30 Å (Figure 2-7S(b)) comparing the pure LNO and the W-doped compounds from pair interatomic distance aspect. Although no major changes like clear extra peaks are detected in the PDF results of the doped compounds, using a more detailed analysis, we can deduce that the main W influence is reflected through small PDF peak shifts toward higher r-position as well as peak broadening, which is particularly noticeable with higher W content, Figure 2-8S. The shift to larger r-spacing could be caused by an average increase of strain in highly doped structures due to a combination of factors: 1) the increase in cation mixing in W-doped LNO structure and having more Ni^{+2} with larger radius than Ni^{3+}, or 2) Li deficiency inside the LNO due to the presence of Li-rich W-compounds which reduce more Ni^{3+} to balance the crystal charge. The damping of the peaks, causing an apparent broadening,

particularly enhanced at larger r-spacings, might be triggered by several factors: larger Debye-Waller factors in the structure; the presence of low-coherence areas or few amorphous phases, either of which could produce destructive interference and reduce the sharpness of the peaks on a further distance than their crystalline domain size [48]; or the presence of crystalline phases similar to LNO but with a range of slightly different lattice parameters, in small enough concentrations that no strong additional peak are clearly visible in the PDF. The larger damping at higher distances suggests that the perturbations are longer range and that the average structure remains the same, likely due to the low concentration of W. The main conclusion that can be drawn from the PDF data is that no significant changes in the average structure of the LNO were induced after doping with W with the concentration of W used in this work.

To quantitatively calculate the effects of the dopant on the PDF peaks, five different peaks were chosen, marked in Figure 2-7S(a). The location of the maximum and the full width half maximum (FWHM) of the peaks were measured, and the results are represented in Table 2-2S**.** The numbers have been rounded based on the order of PDF's resolution ($\delta r = \frac{2\pi}{Q_{max}} = \frac{2\pi}{26} = 0.242$ Å). As previously mentioned, the general trend in all the peak locations was moving toward higher r-spacings when the W amount increased. Based on that, the strain value was calculated by considering the location of the peaks in the doped material with respect to the same peak in LNO. The number of each bond per unit volume and their effect on the final PDF peaks, considered by separately simulating the PDF shape of each bond, are different. The first peak is detected at around 1.95 Å, which is almost equal to what we expect from the first Ni-O (~1.97Å) and Li-O (as well as Ni in Li site-O ~2.11Å) bond length. The second peak, labeled as (2), is positioned around ~2.87Å, which is near the bond length of O-O (varies between ~2.7Å to ~3.1Å), Li-Li (or two Ni in lithium

site) about ~2.88Å, Ni-Ni (including both Ni either in Ni site or Li site) between ~2.88Å to 2.89Å as well as the Ni-Li between ~2.88Å to 2.89Å. Based on the calculation, the third peak is placed around ~ 4.98Å, which could represent the bonding distance between O-O (~ 4.88Å to ~ 5.1Å), Li-Li, Ni-Ni, and Ni-Li (~ 4.98Å to ~ 5 Å). The fourth peak's position is around ~ 6.46Å, which is almost the same bonding distance of O-O (~6.35Å to ~ 6.53Å), Li-Li (~6.46Å) as well as Ni-Li and Ni-Ni (~ 6.44Å to ~ 6.46Å). The final peak, (5), is located around ~ 7.6Å, which presents a similar distance to what we expect to see from the O-O (~7.55Å to ~ 7.7Å), Li-Li (~7.61Å to ~ 7.63Å), Ni-Li and Ni-Ni (~7.61Å to ~ 7.66Å). A simple correlation of the layer distances with the presence of W is not straightforward since, for these distances, many factors can cause changes, such as bonding lengths, bonding angles, or distortion, and so on (Li layer and Ni layer distances are around (lattice parameter c/3) ~ 4.73 Å in LNO). Nevertheless, there are no obvious new peaks, and all peaks show an increasing trend in the displacement (hence strain) with higher amounts of W, except for the LNO_2% W_Mech sample. The second peak, on the other hand, still has a higher displacement value with higher doping concentrations even in the LNO_2% W_Mech sample. The higher precision of the second peak in correctly identifying the increase in strain can be attributed to its lowest FWHM in comparison with the other peaks in all materials, which reduces the calculation error to locate the bonding length, r. In addition, as described in the XRD results, from the LNO structural aspect, the "a" lattice parameter showed an expanding behavior with higher W content, and that distance (~2.8769Å) is the same as the bonding distance of O-O, Li-Li, Ni-Ni, and Ni-Li. Since Li and O are both lighter elements than Ni and their X-ray scattering factors are lower than Ni, they could not make a significant difference in XRD, and the effective bonding change is caused by Ni-Ni. This conclusion is also supported by separate PDF simulations in

PDFgui. The number of Ni pairs in the LNO in the r location of the second peak is almost doubled compared to any other place. This is another factor contributing to the shift behavior observed when this peak is considered for all the doped materials. By either considering a higher amount of cation mixing (higher amount of Ni^{+2}) or new Li-rich W-compounds in the doped materials, the change in the Ni-Ni bonding with a higher number per volume unit cell at the second peak position better explains the behavior of this peak among the others in all the doped samples.

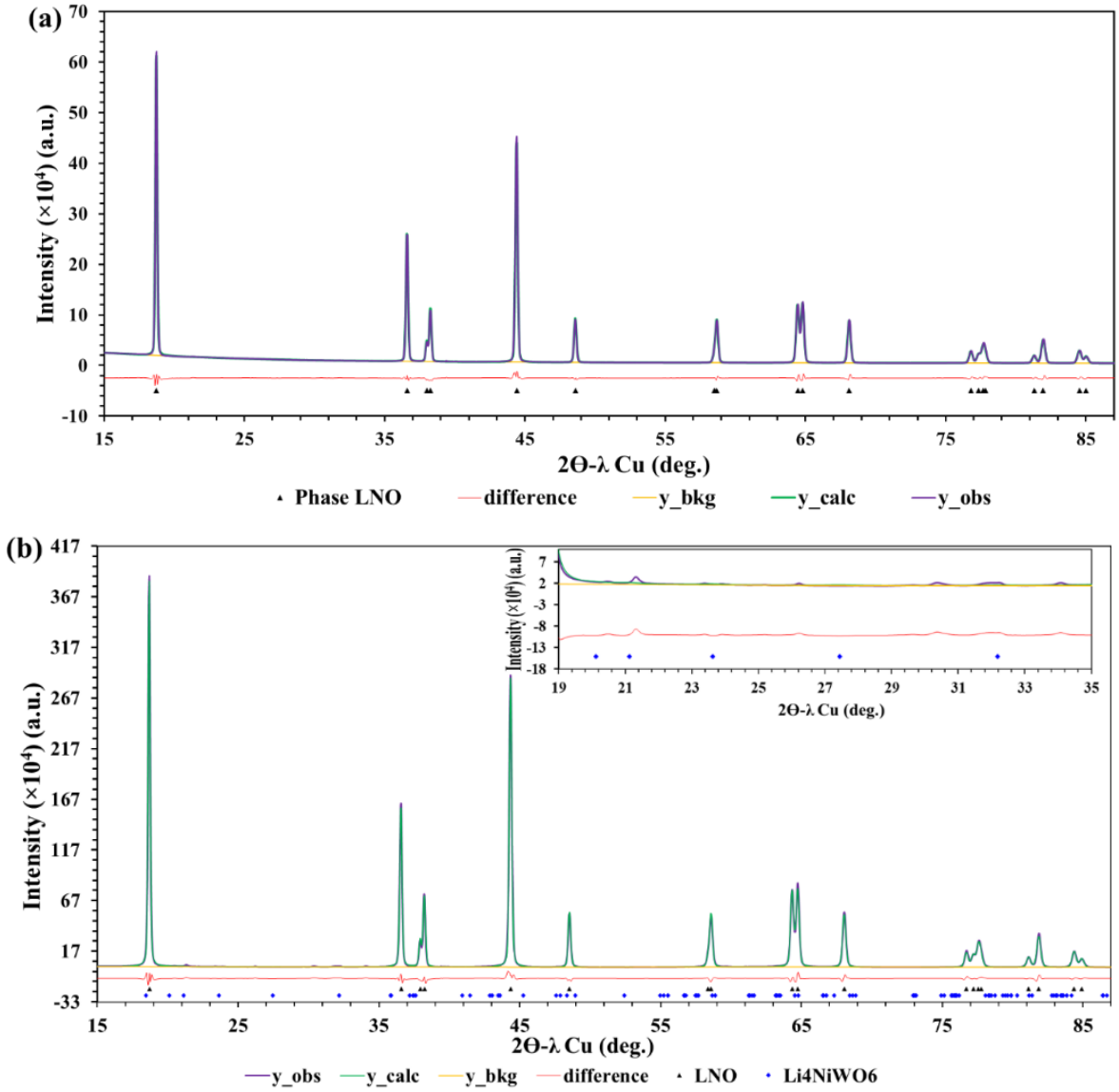

Figure 2-6S Measured (y_obs), and calculated (y_calc) SXRD patterns, as well as their difference, are shown for (a) LNO_Pristine, (b) LNO_1%W_Mech, and (c) LNO_4%W_Mech respectively. The positions of the present phases are illustrated in each of them as well. The higher magnification map between 19° and 35° in (b) and (c), provide a better view of the fitting quality. As can be seen, the fitting in the 19° to 35° range is not convincing for (b) due to the very low amount of W-phase (Table 2-1) and very high intensity of LNO peaks. However, in higher W-doped LNO, (c), the quality of fitting in the 19° to 35° range improves significantly.

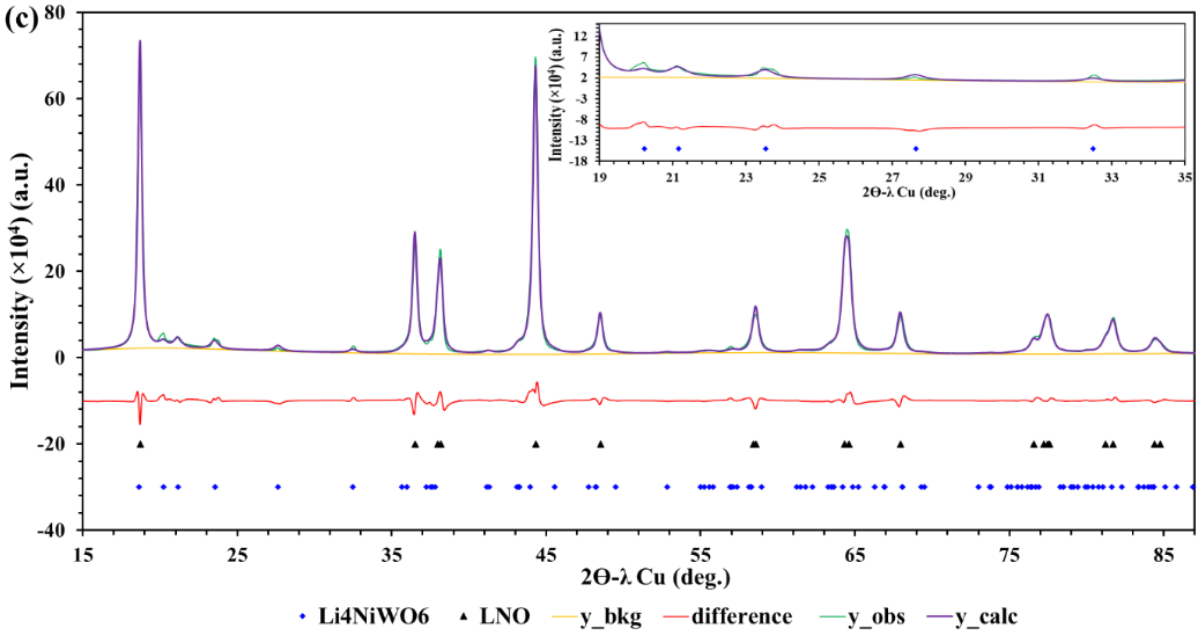

Figure 2-6S Continued.

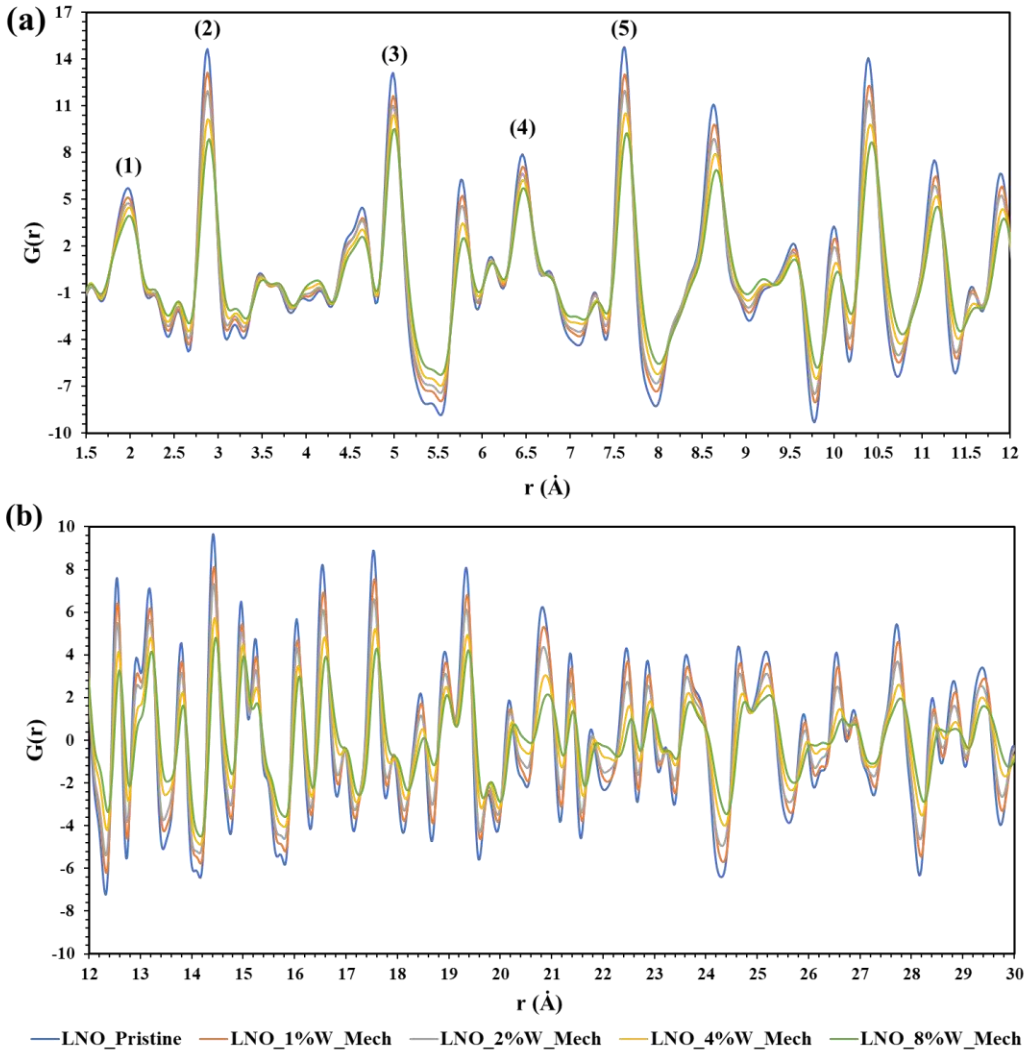

Figure 2-7S Comparison of the PDF data among LNO and the different amounts of tungsten dopant ones in (a) the local structure range (1.5Å -12Å), and (b) the intermediate structure range (12Å-30Å). Numbers represent the location of selected peaks for quantification analysis.

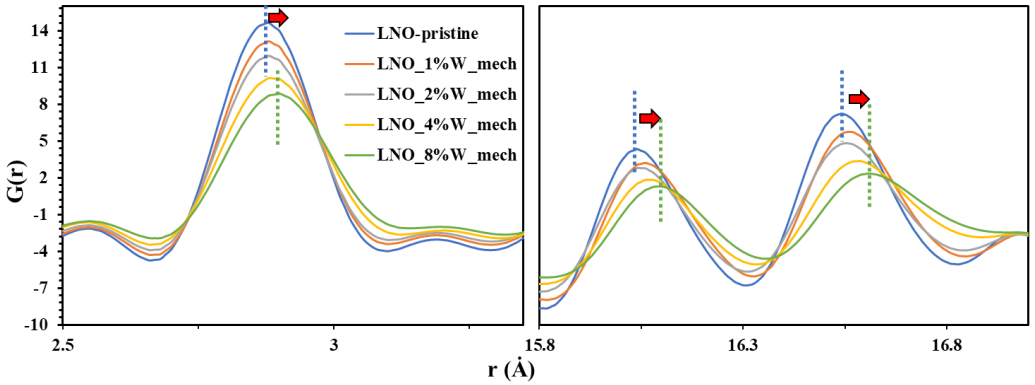

Figure 2-8S PDF peaks are shown with higher magnification to better illustrate their shift toward higher r-position and peak broadening as a function of W amount.

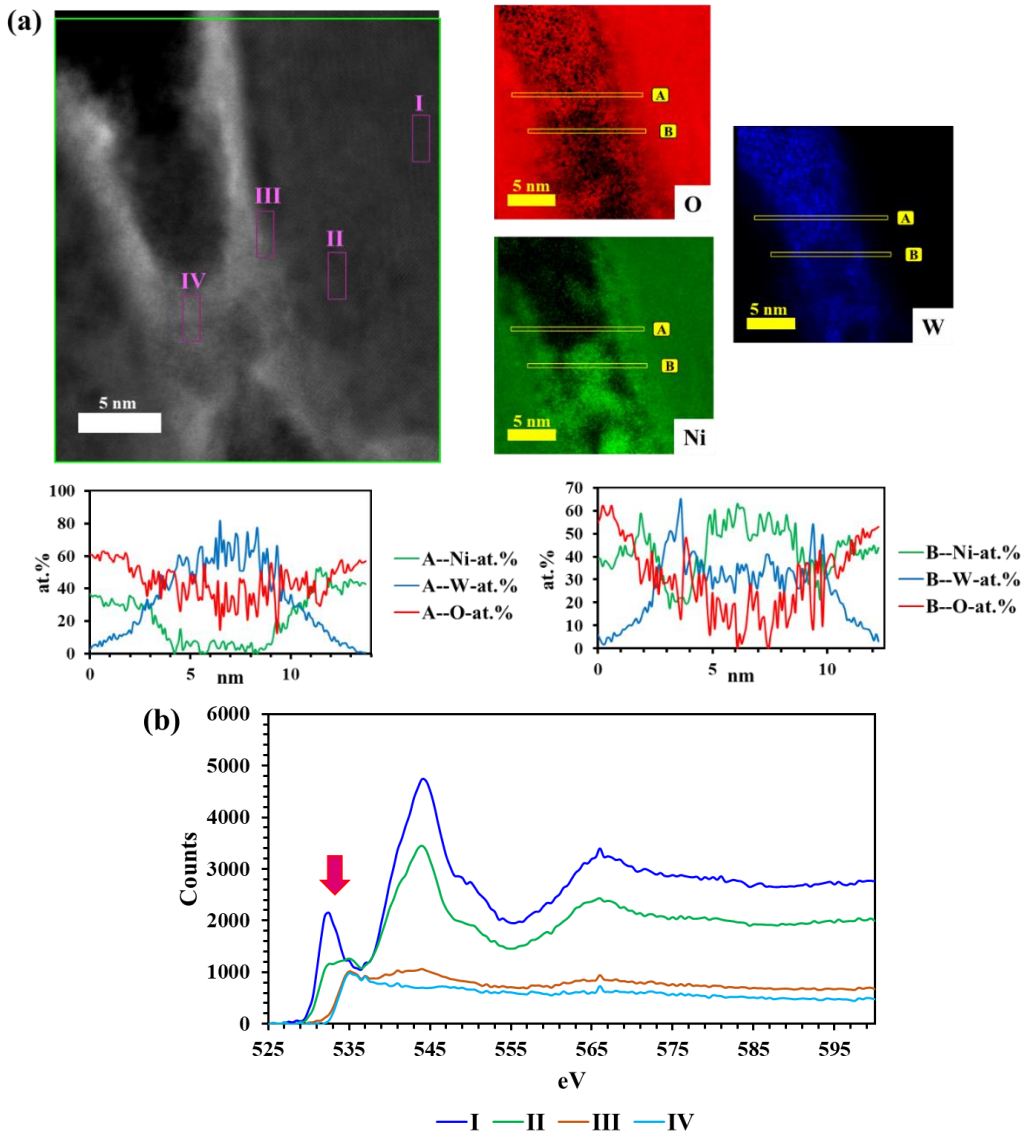

Figure 2-9S (a) annular dark-field (ADF) and spectrum images from LNO_1%W_ Copr's grain boundary, with the labeled elemental distribution. The line profiles from two different selected areas, "A" and "B" also reveal the presence of all of these three elements simultaneously. (b) Changes in the O pre-edge peak intensity and O K-edge shape from within the core of particles (i.e., areas away from grain boundaries) into different grain boundary regions based on the selected areas illustrated in (a) ADF image. (c) Further investigation by MLLS fitting after principal component analysis, to differentiate the elemental distribution of O with and without pre-edge and their reference spectra shape are also illustrated in red and rouged. (d) MLLS fitting results show a good fit for the three selected regions in (c).

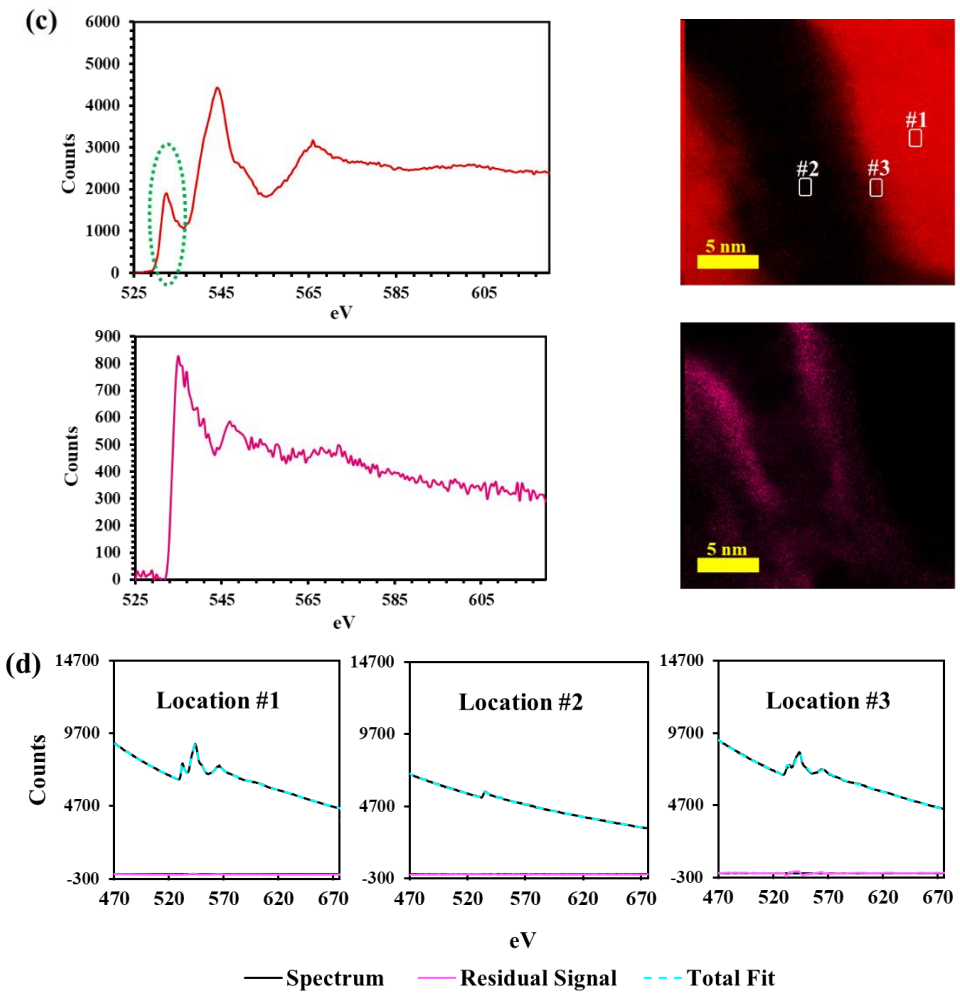

Figure 2-9S Continued.

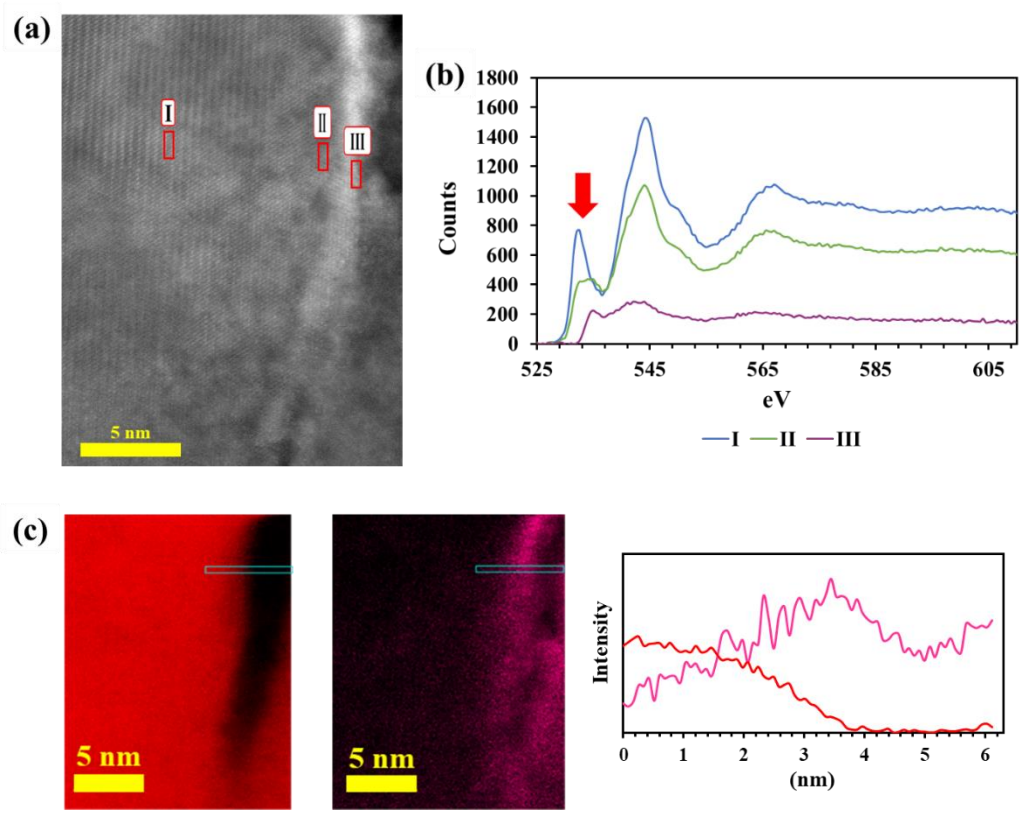

Figure 2-10S Spectral variations in different areas of the LNO_1%W_Copr structure. (a) ADF image and (b) changes in the O pre-edge peak and edge shape based on different regions identified on selected areas of the ADF image (a), which is the same as, Figure 2-4(c). (c)The EELS maps from one of the primary particles inside the mentioned material in Figure 2-4(c), after PCA and MLLS fitting and the line profile extracted from the chosen cyan line to distinguish the distribution of O peak with and without pre-edge in red and rouged, respectively.

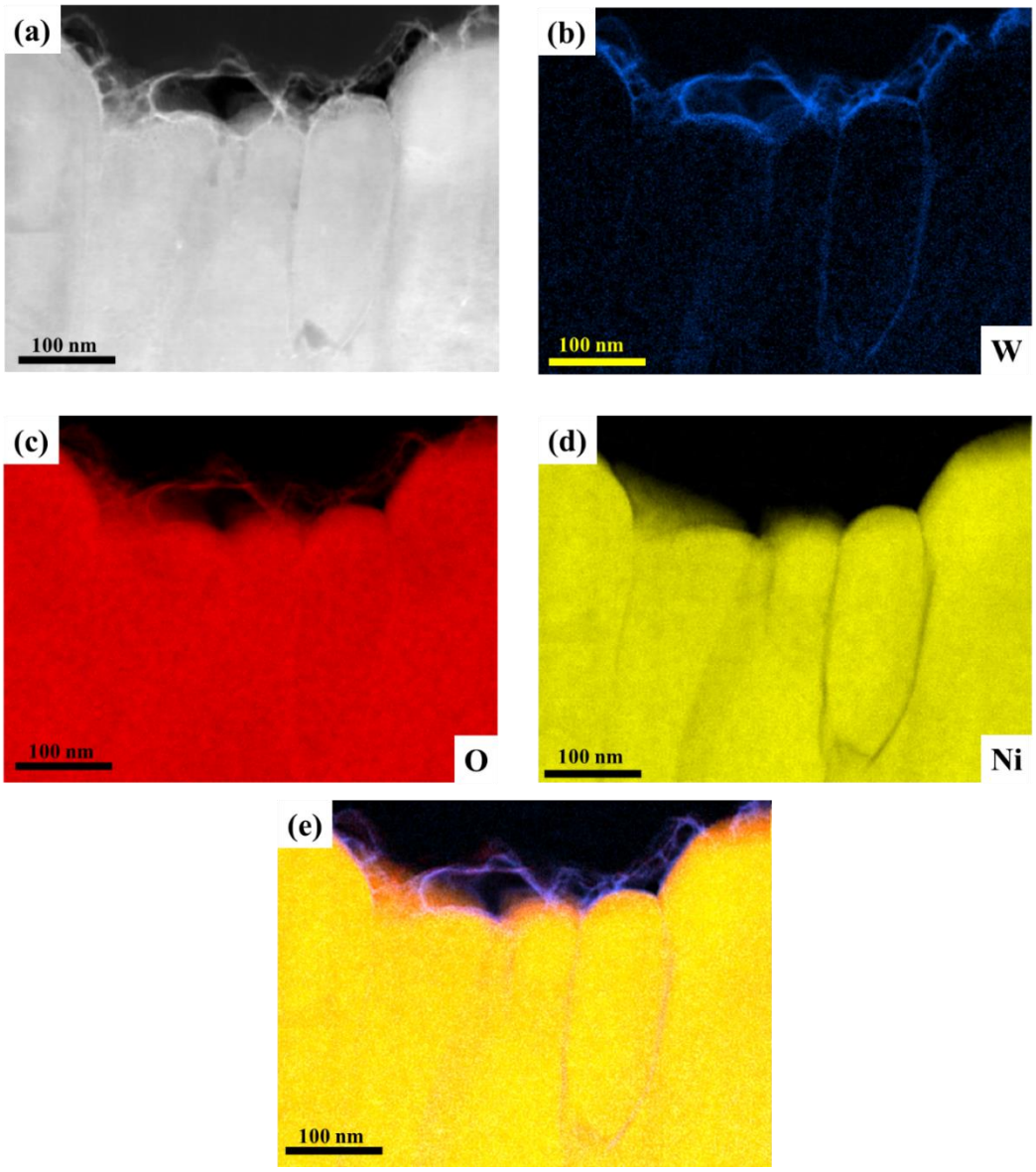

Figure 2-11S (a) High magnification ADF image from the top surface of LNO_1%W_ Mech. EELS mapping images illustrate the elemental distribution of (b) W, (c) O, and (d) Ni in blue, red, and yellow, respectively. (e) The color mix picture of all three elements (W, O, and Ni) shows that on the very surface, a thin layer in purple contains only W and O, with about 10 nm in width.

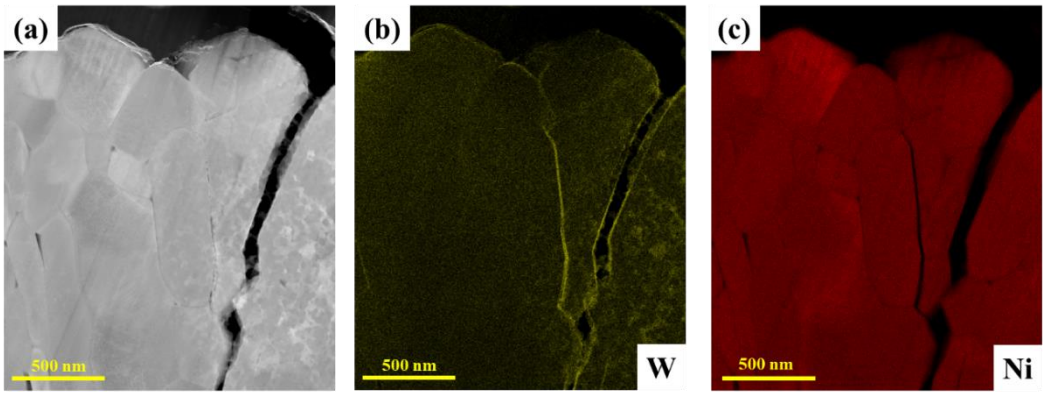

Figure 2-12S (a) HAADF image and EDXS maps of (b) W and (c) Ni, in LNO_1%W_ Mech sample. The W maps are consistent with the segregation of W, as determined from EELS measurements (see the main manuscript).

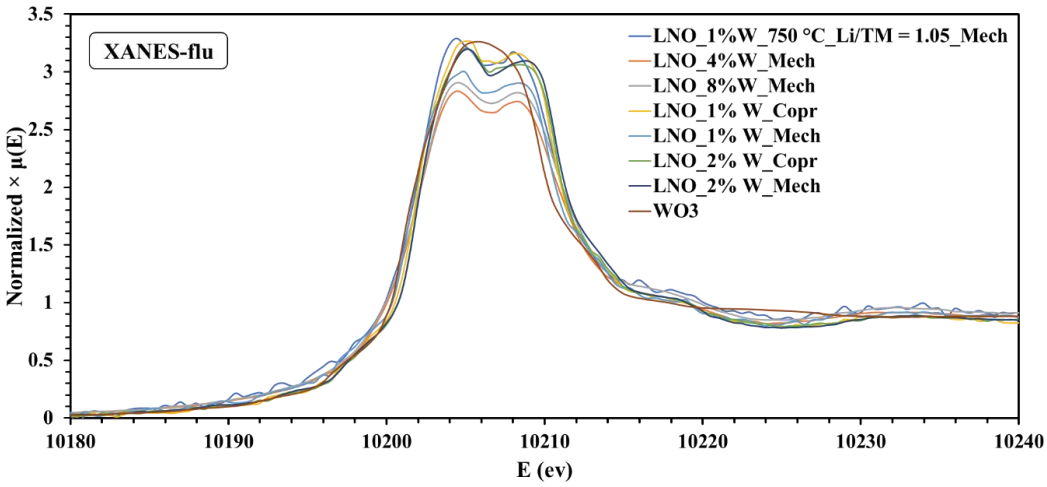

Figure 2-13S The normalized XANES spectra of W L-edge for W-doped materials using the mechanofusion, and coprecipitation approaches. All data are acquired in fluorescence mode and energy calibration reference was WO_3 nanoparticles.

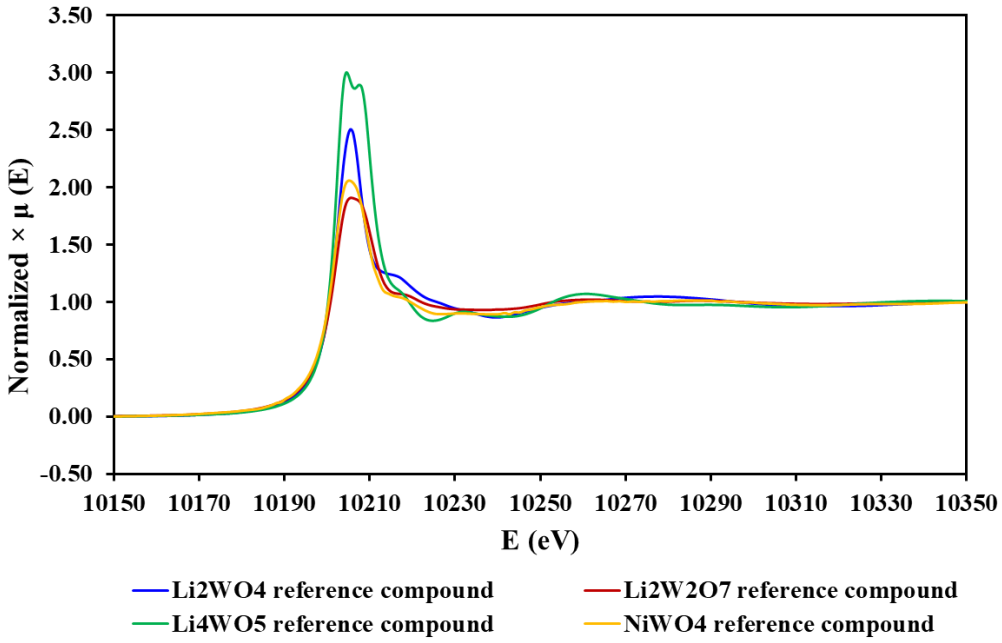

Figure 2-14S The normalized μ(E) of four reference compounds from transmission mode.

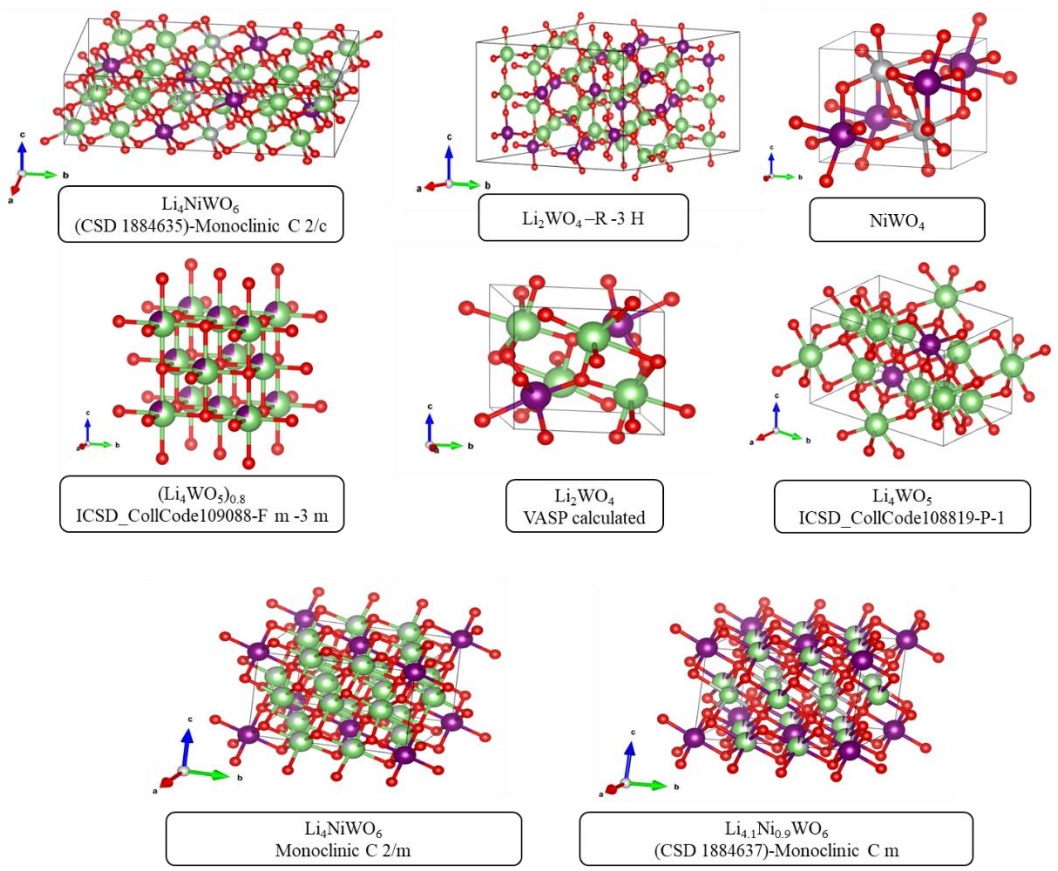

Figure 2-15S 3D crystal structures of eight different compounds were selected for the final fitting step through the doped materials.

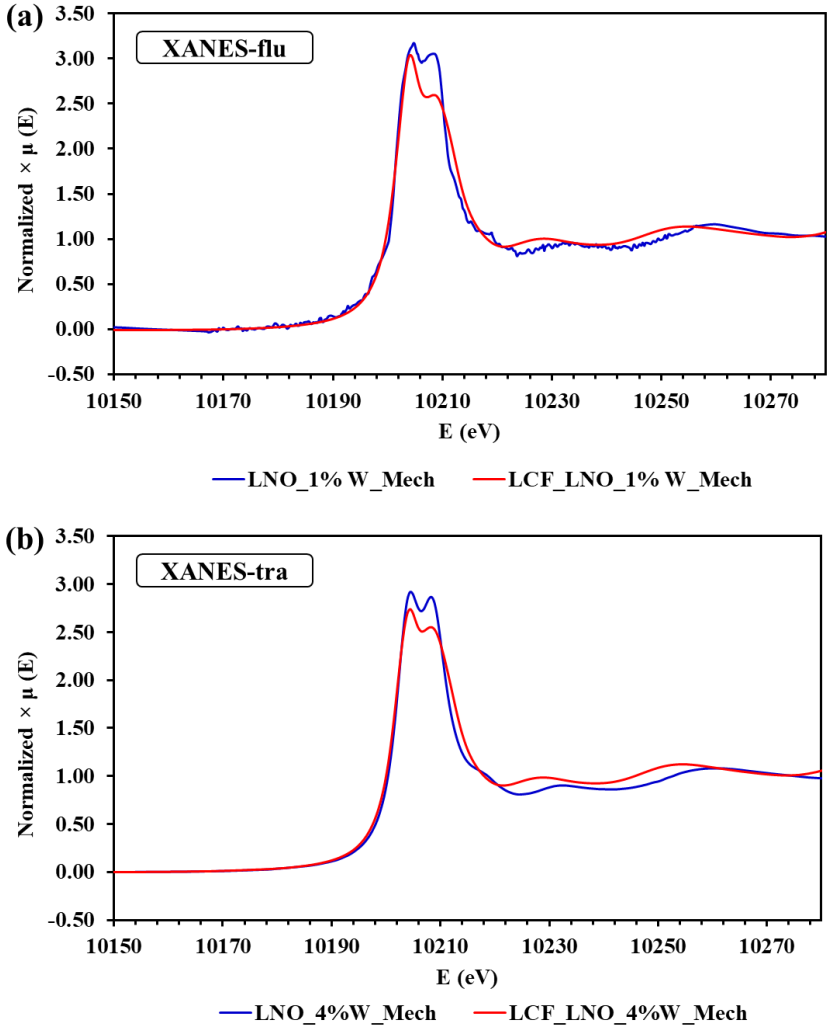

Figure 2-16S The comparison between LCF best fitting results and the experimental data regarding the normalized μ(E) of (a) LNO_1% W_Mech sample from fluorescence mode and (b) LNO_4% W_Mech sample from transmission mode.

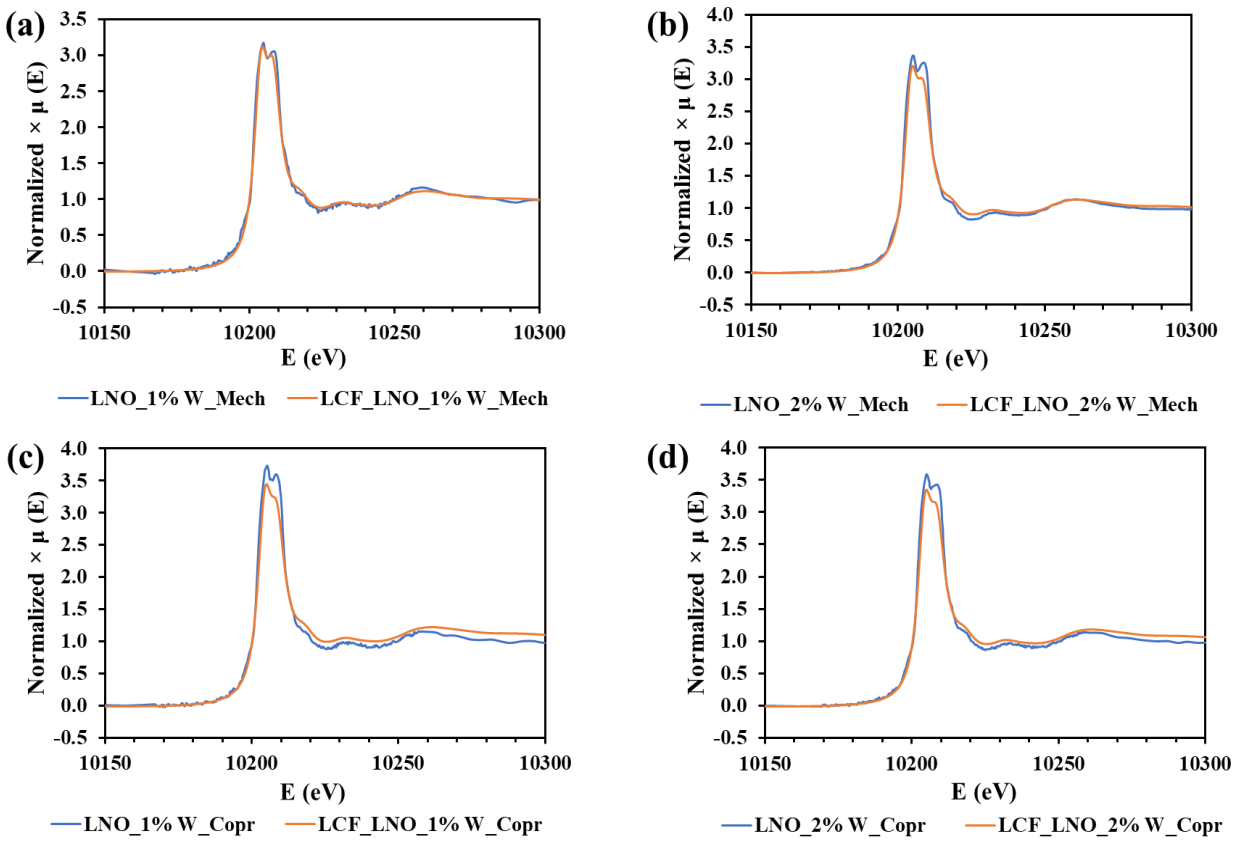

Figure 2-17S The comparison between LCF fitting results considering the 4 reference compounds, Figure 2-14S, and the experimental data regarding the normalized μ(E) of (a) LNO_1% W_Mech, (b) LNO_2% W_Mech, (c) LNO_1% W_Copr and (d) LNO_2% W_Copr sample, respectively. All the spectra are acquired in fluorescence mode. Based on the LCF fitting, all of these fitted data have more than a phase weight of 0.84 for Li_4WO_5.

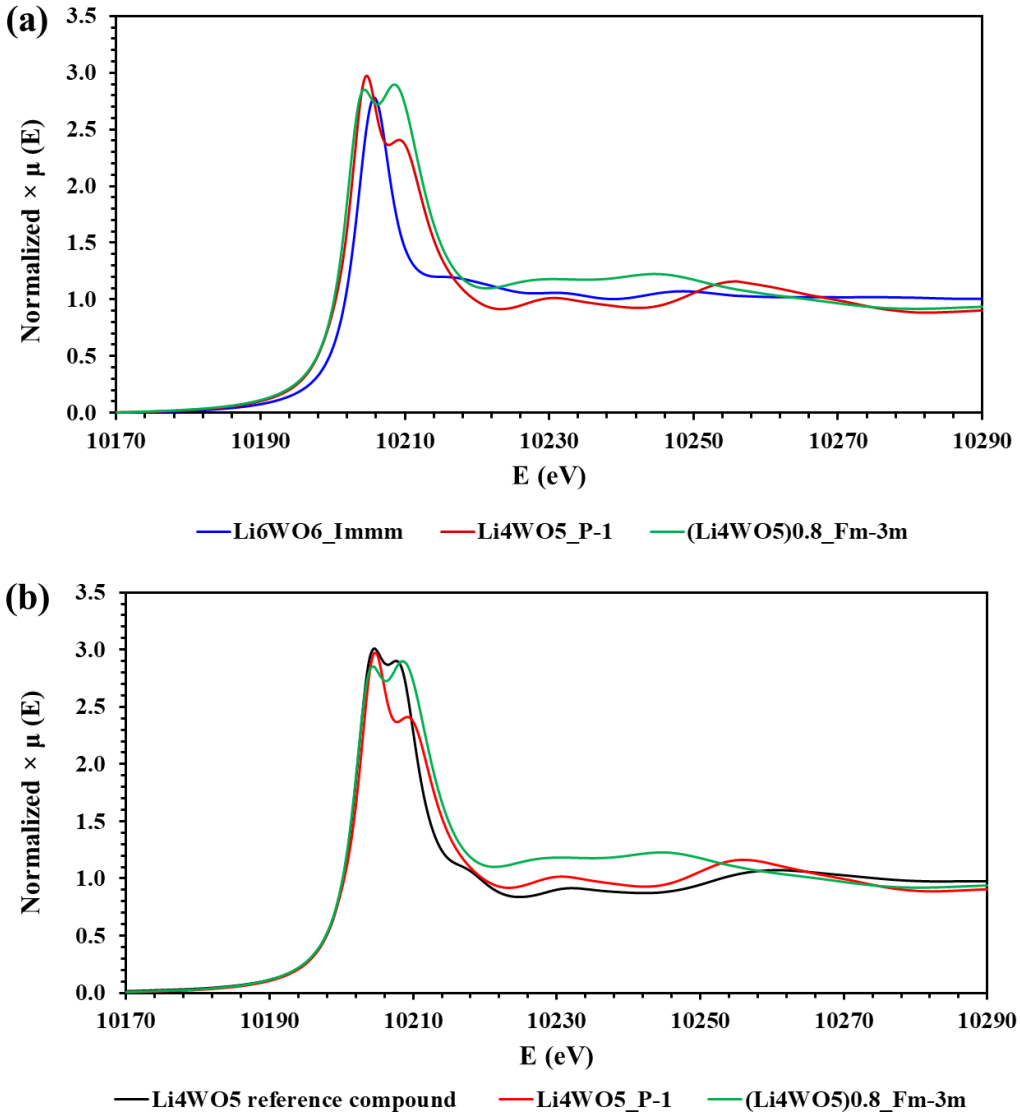

Figure 2-18S (a) The normalized μ(E) is based on the XANES modeling performed on 3 phases identified within the Li_4WO_5 reference compound. (b) Comparison among the experimental normalized μ(E) of the Li_4WO_5 reference compound (from transmission mode) and two calculated ones based on the identified crystal phases. These two crystal phases are also considered in the 8 final candidate phases.

Table 2-2S The PDF peak analysis and strain calculation in doped materials based on the selected peak locations.

Sample name	Peak's parameters (Å)	Peak's number					Δr/r * 100				
		1	2	3	4	5	1	2	3	4	5
LNO_Pristine	FWHM	0.290	0.198	0.247	0.209	0.228	0	0	0	0	0
	Xc	1.957	2.878	4.985	6.461	7.615					
LNO_1%W_Mech	FWHM	0.289	0.199	0.256	0.209	0.232	0.095	0.128	0.088	0.115	0.102
	Xc	1.959	2.881	4.989	6.469	7.623					
LNO_2%W_Mech	FWHM	0.285	0.199	0.259	0.208	0.236	0.081	0.152	0.030	0.024	0.063
	Xc	1.958	2.882	4.986	6.463	7.620					
LNO_4%W_Mech	FWHM	0.306	0.205	0.271	0.214	0.247	0.137	0.442	0.217	0.158	0.234
	Xc	1.959	2.890	4.995	6.472	7.633					
LNO_8%W_Mech	FWHM	0.304	0.213	0.279	0.220	0.256	0.341	0.737	0.315	0.253	0.377
	Xc	1.963	2.899	5.000	6.478	7.644					

Table 2-3S The finalized normalized XANES fitting results for different doped materials.

Sample name	Calculated weighting		Normalized weighting		E_0	E_0	R-factor
	Li_4NiWO_6	$Li_{4.1}Ni_{0.9}WO_6$	Li_4NiWO_6	$Li_{4.1}Ni_{0.9}WO_6$	Li_4NiWO_6	$Li_{4.1}Ni_{0.9}WO_6$	
LNO_1% W_Mech	0.341	0.703	0.327	0.673	-2.1	-0.1	0.0097
LNO_2% W_Mech	0.232	0.827	0.219	0.781	-1.8	0.3	0.0153
LNO_1% W_Copr	0.203	0.933	0.179	0.821	-2.2	0.2	0.0201
LNO_2% W_Copr	0.241	0.868	0.217	0.783	-2	0.3	0.0188
LNO_4%W_Mech	0.483	0.517	0.483	0.517	-1.6	0.2	0.0079
LNO_8%W_Mech	0.414	0.581	0.416	0.584	-1.5	0.3	0.0089
LNO_1%W_750 °C_Li/TM = 1.05_Mech	0.366	0.709	0.34	0.66	-2.1	-0.1	0.0136

2.6 References

[1] A. Manthiram, A reflection on lithium-ion battery cathode chemistry, Nat. Commun. 11 (2020) 1–9. https://doi.org/10.1038/s41467-020-15355-0.

[2] A. Manthiram, An Outlook on Lithium Ion Battery Technology, ACS Cent. Sci. 3 (2017) 1063–1069. https://doi.org/10.1021/acscentsci.7b00288.

[3] D. Andre, S.J. Kim, P. Lamp, S.F. Lux, F. Maglia, O. Paschos, B. Stiaszny, Future generations of cathode materials: An automotive industry perspective, J. Mater. Chem. A. 3 (2015) 6709–6732. https://doi.org/10.1039/c5ta00361j.

[4] A. Konarov, S.T. Myung, Y.K. Sun, Cathode materials for future electric vehicles and energy storage systems, ACS Energy Lett. 2 (2017) 703–708. https://doi.org/10.1021/acsenergylett.7b00130.

[5] J.B. Goodenough, K.S. Park, The Li-ion rechargeable battery: A perspective, J. Am. Chem. Soc. 135 (2013) 1167–1176. https://doi.org/10.1021/ja3091438.

[6] C. Liu, Z.G. Neale, G. Cao, Understanding electrochemical potentials of cathode materials in rechargeable batteries, Mater. Today. 19 (2016) 109–123. https://doi.org/10.1016/j.mattod.2015.10.009.

[7] Y. Tang, Y. Zhang, W. Li, B. Ma, X. Chen, Rational material design for ultrafast rechargeable lithium-ion batteries, Chem. Soc. Rev. 44 (2015) 5926–5940. https://doi.org/10.1039/c4cs00442f.

[8] J. Vetter, P. Novák, M.R. Wagner, C. Veit, K.C. Möller, J.O. Besenhard, M. Winter, M. Wohlfahrt-Mehrens, C. Vogler, A. Hammouche, Ageing mechanisms in lithium-ion batteries, J. Power Sources. 147 (2005) 269–281. https://doi.org/10.1016/j.jpowsour.2005.01.006.

[9] W. Li, E.M. Erickson, A. Manthiram, High-nickel layered oxide cathodes for lithium-based automotive batteries, Nat. Energy. 5 (2020) 26–34. https://doi.org/10.1038/s41560-019-0513-0.

[10] A. Kwade, W. Haselrieder, R. Leithoff, A. Modlinger, F. Dietrich, K. Droeder, Current status and challenges for automotive battery production technologies, Nat.

Energy. 3 (2018) 290–300. https://doi.org/10.1038/s41560-018-0130-3.

[11] H.J. Noh, S. Youn, C.S. Yoon, Y.K. Sun, Comparison of the structural and electrochemical properties of layered Li[NixCoyMnz]O2 (x = 1/3, 0.5, 0.6, 0.7, 0.8 and 0.85) cathode material for lithium-ion batteries, J. Power Sources. 233 (2013) 121–130. https://doi.org/10.1016/j.jpowsour.2013.01.063.

[12] H. Li, P. Zhou, F. Liu, H. Li, F. Cheng, J. Chen, Stabilizing nickel-rich layered oxide cathodes by magnesium doping for rechargeable lithium-ion batteries, Chem. Sci. 10 (2019) 1374–1379. https://doi.org/10.1039/c8sc03385d.

[13] F. Schipper, E.M. Erickson, C. Erk, J.-Y. Shin, F.F. Chesneau, D. Aurbach, Review—Recent Advances and Remaining Challenges for Lithium Ion Battery Cathodes, J. Electrochem. Soc. 164 (2017) A6220–A6228. https://doi.org/10.1149/2.0351701jes.

[14] W. Liu, P. Oh, X. Liu, M.J. Lee, W. Cho, S. Chae, Y. Kim, J. Cho, Nickel-Rich Layered Lithium Transition-Metal Oxide for High-Energy Lithium-Ion Batteries, Angew. Chemie - Int. Ed. 54 (2015) 4440–4457. https://doi.org/10.1002/anie.201409262.

[15] E.M. Erickson, F. Schipper, T.R. Penki, J.-Y. Shin, C. Erk, F.-F. Chesneau, B. Markovsky, D. Aurbach, Review—Recent Advances and Remaining Challenges for Lithium Ion Battery Cathodes, J. Electrochem. Soc. 164 (2017) A6341–A6348. https://doi.org/10.1149/2.0461701jes.

[16] S.T. Myung, F. Maglia, K.J. Park, C.S. Yoon, P. Lamp, S.J. Kim, Y.K. Sun, Nickel-Rich Layered Cathode Materials for Automotive Lithium-Ion Batteries: Achievements and Perspectives, ACS Energy Lett. 2 (2017) 196–223. https://doi.org/10.1021/acsenergylett.6b00594.

[17] F. Schipper, M. Dixit, D. Kovacheva, M. Talianker, O. Haik, J. Grinblat, E.M. Erickson, C. Ghanty, D.T. Major, B. Markovsky, D. Aurbach, Stabilizing nickel-rich layered cathode materials by a high-charge cation doping strategy: Zirconium-doped LiNi0.6Co0.2Mn0.2O2, J. Mater. Chem. A. 4 (2016) 16073–16084. https://doi.org/10.1039/c6ta06740a.

[18] M. Dixit, M. Kosa, O.S. Lavi, B. Markovsky, D. Aurbach, D.T. Major, Thermodynamic and kinetic studies of LiNi0.5Co0.2Mn0.3O2 as a positive electrode material for Li-ion batteries using first principles, Phys. Chem. Chem. Phys. 18 (2016) 6799–6812. https://doi.org/10.1039/c5cp07128c.

[19] H.H. Sun, H.H. Ryu, U.H. Kim, J.A. Weeks, A. Heller, Y.K. Sun, C.B. Mullins, Beyond Doping and Coating: Prospective Strategies for Stable High-Capacity Layered Ni-Rich Cathodes, ACS Energy Lett. 5 (2020) 1136–1146. https://doi.org/10.1021/acsenergylett.0c00191.

[20] P. Teichert, G.G. Eshetu, H. Jahnke, E. Figgemeier, Degradation and aging routes of ni-rich cathode based li-ion batteries, Batteries. 6 (2020) 1–26. https://doi.org/10.3390/batteries6010008.

[21] A. Chakraborty, S. Kunnikuruvan, S. Kumar, B. Markovsky, D. Aurbach, M. Dixit, D.T. Major, Layered Cathode Materials for Lithium-Ion Batteries: Review of Computational Studies on LiNi1- x- yCoxMnyO2 and LiNi1- x- yCoxAlyO2, Chem. Mater. 32 (2020) 915–952. https://doi.org/10.1021/acs.chemmater.9b04066.

[22] X. Liu, H. Li, E. Yoo, M. Ishida, H. Zhou, Fabrication of FePO 4 layer coated LiNi 1/3Co 1/3Mn 1/3O 2: Towards high-performance cathode materials for lithium ion batteries, Electrochim. Acta. 83 (2012) 253–258. https://doi.org/10.1016/j.electacta.2012.07.111.

[23] N. Zhang, N. Zaker, H. Li, A. Liu, J. Inglis, L. Jing, J. Li, Y. Li, G.A. Botton, J.R. Dahn, Cobalt-Free Nickel-Rich Positive Electrode Materials with a Core-Shell Structure, Chem. Mater. 31 (2019) 10150–10160. https://doi.org/10.1021/acs.chemmater.9b03515.

[24] C. Geng, S. Trussler, M. Johnson, N. Zaker, B. Scott, G. Botton, J.R. Dahn, A low-cost instrument for dry particle fusion coating of advanced electrode material particles at the laboratory scale., J. Electrochem. Soc. (2020). https://doi.org/10.1149/1945-7111/aba00e.

[25] and A.Y. Da Liu, Siyang Liu, Congcong Zhang, Longzhen You, Tao Huang, Revealing the Effect of Ti Doping on Significantly Enhancing Cyclic Performance

at a High Cutoff Voltage for Ni-Rich LiNi0.8Co0.15Al0.05O2 Cathode, (2019) 0–8. https://doi.org/10.1021/acssuschemeng.9b01312.

[26] M. Zubair, G. Li, B. Wang, L. Wang, H. Yu, Electrochemical Kinetics and Cycle Stability Improvement with Nb Doping for Lithium-Rich Layered Oxides, ACS Appl. Energy Mater. 2 (2018) 503–512. https://doi.org/10.1021/acsaem.8b01534.

[27] C. Liang, F. Kong, R.C. Longo, C. Zhang, Y. Nie, Y. Zheng, K. Cho, Site-dependent multicomponent doping strategy for Ni-rich LiNi1-2: YCoyMnyO2 (y = 1/12) cathode materials for Li-ion batteries, J. Mater. Chem. A. 5 (2017) 25303–25313. https://doi.org/10.1039/c7ta08618k.

[28] T. Weigel, F. Schipper, E.M. Erickson, F.A. Susai, B. Markovsky, D. Aurbach, Structural and Electrochemical Aspects of LiNi0.8Co0.1Mn0.1O2 Cathode Materials Doped by Various Cations, 18 (2019). https://doi.org/10.1021/acsenergylett.8b02302.

[29] L.Q. Wang, L.F. Jiao, H. Yuan, J. Guo, M. Zhao, H.X. Li, Y.M. Wang, Synthesis and electrochemical properties of Mo-doped Li [Ni 1 / 3 Mn 1 / 3 Co 1 / 3] O 2 cathode materials for Li-ion battery, 162 (2006) 1367–1372. https://doi.org/10.1016/j.jpowsour.2006.08.033.

[30] F.A. Susai, D. Kovacheva, A. Chakraborty, T. Kravchuk, R. Ravikumar, M. Talianker, J. Grinblat, L. Burstein, Y. Kau, D.T. Major, B. Markovsky, D. Aurbach, Improving Performance of LiNi0.8Co0.1Mn0.1O2 Cathode Materials for Lithium-Ion Batteries by Doping with Molybdenum-Ions: Theoretical and Experimental Studies, (2019). https://doi.org/10.1021/acsaem.9b00767.

[31] U.H. Kim, D.W. Jun, K.J. Park, Q. Zhang, P. Kaghazchi, D. Aurbach, D.T. Major, G. Goobes, M. Dixit, N. Leifer, C.M. Wang, P. Yan, D. Ahn, K.H. Kim, C.S. Yoon, Y.K. Sun, Pushing the limit of layered transition metal oxide cathodes for high-energy density rechargeable Li ion batteries, Energy Environ. Sci. 11 (2018) 1271–1279. https://doi.org/10.1039/c8ee00227d.

[32] H.H. Ryu, G.T. Park, C.S. Yoon, Y.K. Sun, Suppressing detrimental phase transitions via tungsten doping of LiNiO2 cathode for next-generation lithium-ion

batteries, J. Mater. Chem. A. 7 (2019) 18580–18588. https://doi.org/10.1039/c9ta06402h.

[33] G.T. Park, H.H. Ryu, N.Y. Park, C.S. Yoon, Y.K. Sun, Tungsten doping for stabilization of Li[Ni0.90Co0.05Mn0.05]O2 cathode for Li-ion battery at high voltage, J. Power Sources. 442 (2019) 227242. https://doi.org/10.1016/j.jpowsour.2019.227242.

[34] D. Rathore, C. Geng, N. Zaker, I. Hamam, Y. Liu, P. Xiao, G.A. Botton, J. Dahn, C. Yang, Tungsten Infused Grain Boundaries Enabling Universal Performance Enhancement of Co-Free Ni-Rich Cathode Materials, J. Electrochem. Soc. 168 (2021) 120514. https://doi.org/10.1149/1945-7111/ac3c26.

[35] I. Hamam, R. Omessi, D. Rathore, C. Geng, R. Cooke, K. Plucknett, D.P. Bishop, N. Zaker, G.A. Botton, C. Yang, J.R. Dahn, Correlating the mechanical strength of positive electrode material particles to their capacity retention, Cell Reports Phys. Sci. 3 (2022) 100714. https://doi.org/10.1016/j.xcrp.2021.100714.

[36] C. Geng, D. Rathore, D. Heino, N. Zhang, I. Hamam, N. Zaker, G.A. Botton, R. Omessi, N. Phattharasupakun, T. Bond, C. Yang, J.R. Dahn, Mechanism of Action of the Tungsten Dopant in LiNiO 2 Positive Electrode Materials, Adv. Energy Mater. 12 (2022) 2103067. https://doi.org/10.1002/aenm.202103067.

[37] Y. Li, M. Bettge, B. Polzin, Y. Zhu, M. Balasubramanian, D.P. Abraham, Understanding Long-Term Cycling Performance of Li 1.2 Ni 0.15 Mn 0.55 Co 0.1 O 2 –Graphite Lithium-Ion Cells, J. Electrochem. Soc. 160 (2013) A3006–A3019. https://doi.org/10.1149/2.002305jes.

[38] X. Zhang, W.J. Jiang, A. Mauger, Qilu, F. Gendron, C.M. Julien, Minimization of the cation mixing in Li1+x(NMC)1-xO2 as cathode material, J. Power Sources. 195 (2010) 1292–1301. https://doi.org/10.1016/j.jpowsour.2009.09.029.

[39] L. Wang, J. Li, X. He, W. Pu, C. Wan, C. Jiang, Recent advances in layered LiNi x CoyMn1−x−y O2 cathode materials for lithium ion batteries, J. Solid State Electrochem. 13 (2009) 1157–1164. https://doi.org/10.1007/s10008-008-0671-7.

[40] P. Kalyani, N. Kalaiselvi, Various aspects of LiNiO2 chemistry: A review, Sci.

Technol. Adv. Mater. 6 (2005) 689–703. https://doi.org/10.1016/j.stam.2005.06.001.

[41] J. Bréger, M. Jiang, N. Dupré, Y.S. Meng, Y. Shao-Horn, G. Ceder, C.P. Grey, High-resolution X-ray diffraction, DIFFaX, NMR and first principles study of disorder in the Li 2MnO 3-Li[Ni 1/2Mn 1/2]O 2 solid solution, J. Solid State Chem. 178 (2005) 2575–2585. https://doi.org/10.1016/j.jssc.2005.05.027.

[42] N. Yabuuchi, K. Yoshii, S.-T. Myung, I. Nakai, S. Komaba, Detailed Studies of a High-Capacity Electrode Material for Rechargeable Batteries, Li2MnO3−LiCo1/3Ni1/3Mn1/3O2, J. Am. Chem. Soc. 133 (2011) 4404–4419. https://doi.org/10.1021/ja108588y.

[43] A.M.J. Electrochem, A. Soc, S. Choi, A. Manthiram, Factors Influencing the Layered to Spinel-like Phase Transition in Layered Oxide Cathodes Factors Influencing the Layered to Spinel-like Phase Transition in Layered Oxide Cathodes, (2002). https://doi.org/10.1149/1.1497171.

[44] S. Jung, H. Gwon, J. Hong, K. Park, D. Seo, Understanding the Degradation Mechanisms of Ion Batteries, (2014) 1–7. https://doi.org/10.1002/aenm.201300787.

[45] S. Hwang, D.H. Kim, K.Y. Chung, W. Chang, Understanding local degradation of cycled Ni-rich cathode materials at high operating temperature for Li-ion batteries, Appl. Phys. Lett. 105 (2014). https://doi.org/10.1063/1.4895336.

[46] Z.N. Taylor, A.J. Perez, J.A. Coca-Clemente, F. Braga, N.E. Drewett, M.J. Pitcher, W.J. Thomas, M.S. Dyer, C. Collins, M. Zanella, T. Johnson, S. Day, C. Tang, V.R. Dhanak, J.B. Claridge, L.J. Hardwick, M.J. Rosseinsky, Stabilization of O.O Bonds by d0 Cations in Li4+xNi1-xWO6 ($0 \leq x \leq 0.25$) Rock Salt Oxides as the Origin of Large Voltage Hysteresis, J. Am. Chem. Soc. 141 (2019) 7333–7346. https://doi.org/10.1021/jacs.8b13633.

[47] A. van Bommel, J.R. Dahn, Analysis of the Growth Mechanism of Coprecipitated Spherical and Dense Nickel, Manganese, and Cobalt-Containing Hydroxides in the Presence of Aqueous Ammonia, Chem. Mater. 21 (2009) 1500–1503.

https://doi.org/10.1021/cm803144d.

[48] V. Petkov, Pair Distribution Functions Analysis, Charact. Mater. (2012) 1361–1372. https://doi.org/10.1002/0471266965.com159.

[49] G. Kresse, J. Hafner, Ab initio molecular dynamics for liquid metals, Phys. Rev. B. 47 (1993) 558–561. https://doi.org/10.1103/PhysRevB.47.558.

[50] G. Kresse, J. Hafner, Ab initio molecular-dynamics simulation of the liquid-metalamorphous- semiconductor transition in germanium, Phys. Rev. B. 49 (1994) 14251–14269. https://doi.org/10.1103/PhysRevB.49.14251.

[51] R.A. Vargas-Hernández, Bayesian Optimization for Calibrating and Selecting Hybrid-Density Functional Models, J. Phys. Chem. A. 124 (2020) 4053–4061. https://doi.org/10.1021/acs.jpca.0c01375.

[52] P.E. Blöchl, Projector augmented-wave method, Phys. Rev. B. 50 (1994) 17953–17979. https://doi.org/10.1103/PhysRevB.50.17953.

[53] J. Sun, R.C. Remsing, Y. Zhang, Z. Sun, A. Ruzsinszky, H. Peng, Z. Yang, A. Paul, U. Waghmare, X. Wu, M.L. Klein, J.P. Perdew, Accurate first-principles structures and energies of diversely bonded systems from an efficient density functional, Nat. Chem. 8 (2016) 831–836. https://doi.org/10.1038/nchem.2535.

Chapter 3

Structural Evolution of Cycled Complex Nickel-Rich Cathode Materials Enriched with Tungsten

Complete Citation:

Zaker, N., Geng, C., Hamam, I., Chen, N., Yang, C., Dahn, J.R., Botton, G.A.

Acknowledgments

This research was funded by NSERC through a Discovery Grant. Part of the research described in this paper was performed at the Canadian Light Source, a national research facility at the University of Saskatchewan, which is supported by the Canada Foundation for Innovation (CFI), the Natural Sciences and Engineering Research Council (NSERC), the Canadian Institutes of Health Research (CIHR), the Government of Saskatchewan, and the University of Saskatchewan. The electron microscopy work was carried out at the Canadian Centre for Electron Microscopy (CCEM), a facility supported by the Canada Foundation for Innovation, NSERC, and McMaster University. Synthesis of the cathodes and cycling measurements were carried out at Dalhousie University supported financially by NSERC, Tesla Canada, and the Alliance grant.

Abstract:

The chemical stability and structural integrity of W-enriched $LiNiO_2$ (LNO) cathode materials are investigated following electrochemically cycling to determine the effect of W on the cycling behavior of these layered materials. The presence of 1%W, mostly located at grain boundaries between primary particles and the surface of the LNO secondary particle structures, enhances the cycling performance of particles that have been enriched through the mechanofusion process. In materials where the LNO cathode particles are not optimized and contain porosities, the doping is not effective in spite of the W enrichment, as the porosities enable infiltration of the electrolyte. The W-rich layer on the surface of secondary particles in the 1%W enriched sample prepared by mechanofusion plays an excellent protective layer role as CEI, while W-phases at grain boundaries generate a more robust structure by accommodating some of the cycling stress.

Keywords:

Ni-rich cathode; Tungsten enrichment; Structural evolution; Cycling effect; Li-ion battery.

3.1 Introduction

Lithium-ion batteries (LIB) have grown to be vital energy storage devices for many portable appliances, especially electric vehicles [1–4]. Despite the high energy density of LIBs, insufficient battery life, performance, cost, and safety are still playing important roles in inhibiting the broad use of this technology [2,5,6]. To reach the favorable performance target, battery materials scientists are working on developing better negative and positive electrode materials with higher capacity and better cyclic life [7]. In spite of achieving higher capacity by utilizing silicon-based anodes [8], cathode materials are still limiting the practical capacity of the cell and dominating the material price, especially for those industrial materials which contain cobalt [9,10]. To address these limitations, Ni-rich positive electrode materials, among other popular layered structures, have shown promising results in increasing the specific capacity [9,11]. However, nickel-rich materials exhibit some undesirable behaviors, namely safety hazards, thermal instabilities, as well as fast deterioration of their practical lifetimes [12–16]. To tackle these challenges in ultra-high Ni cathode host structures, a variety of bulk and/or surface modifying approaches have been recommended, such as the introduction of dopants, protecting the outer part of the particles by coating, and using a variety of core-shell structures [12,17–22]. Recent findings indicate that adding a low tungsten content to the Ni-rich cathode materials can noticeably enhance the performance of these LIBs and reduce cyclic degradation [23–26]. In our latest published work [27–30], we mainly focused on identifying the location of W, its distribution, and any new possible W-compounds present in W-enriched Ni-rich materials where the addition of W is carried out using two different synthesis approaches, namely mechanofusion and coprecipitation. Using high-resolution microscopy and spectroscopy techniques, we provided detailed information regarding the heterogeneous

distribution of W (on the very surface of the secondary particles and in between the grain boundaries of primary particles) as well as the presence of W-rich variants $Li_{4+x}Ni_{1-x}WO_6$ (x=0 and 0.1), and the likelihood of $Li_xW_yO_z$ compounds [28,30]. Due to the importance of understanding the failure mechanisms of these new complex structures after extensive cycling, we focus here on the microstructure evolution and the mechanisms of the capacity fade. To fulfill this aim, advanced photon- and electron-based characterization techniques have been used for acquiring and processing high-resolution structural and spectroscopic data. This powerful combination provides in-depth insight into the most critical factors affecting the failure mechanisms.

3.2 Experimental procedures

3.2.1 Synthesis procedures

To understand the effect of W additions to LNO, two different enrichment methods discussed previously [28,30] were considered, mechanofusion and coprecipitation. For the mechanofusion process, 50.0 g of a commercial 15 μm-size $Ni(OH)_2$ along with 1.263 and 2.552 g of WO_3 nano-sized powder, was added simultaneously into the mechanofusion bowl, for making LNO with 1 and 2 mol% of W, respectively. The bowl spun at 2400 rpm speed for a duration of 60 minutes. To prepare particles through coprecipitation, a continuously stirred tank reactor (CSTR) was used to obtain $(Ni_{1-x}(OH)_2)_{0.98} \cdot (NiWO_4)_{0.01}$ (with W/(Ni+W) molar ratio of 0.01) and $(Ni_{1-x}(OH)_2)_{0.96}$ $(NiWO_4)_{0.02}$ (with W/(Ni+W) molar ratio of 0.02) precursors. The synthesis process was inspired by Van Bommel et al. work [31], and the details involving the materials used and the technical parameters were described in the authors' earlier papers [28,30]. As highlighted further below in the

manuscript, samples enriched with W by coprecipitation are porous in nature, an effect that will be discussed through the paper.

For the lithiation process, $LiOH \cdot H_2O$ was ground with each synthesized material batch obtained from mechanofusion as well as from coprecipitation separately to reach precursors with a molar ratio of Li/ (Ni + W) = 1.02/1. Then, these ground precursors were preheated under an oxygen atmosphere for 3 hours at 480 °C and then reground for more homogeneous mixing. After that, the heating processes began at 480 °C for 2 hours, followed by 20 hours at 800 °C (due to improved performance results [28]), all under an oxygen atmosphere. For reference comparison, the pure LNO (identified hereafter as LNO_pristine or LNO_700) was prepared under a similar heat treatment process, with a different second heating step at a temperature of 700 °C. To provide a comprehensive interpretation of the effect of the final heat treatment temperature, another LNO batch with the same heat treatment process, as the one used for the W-enriched particles, was made and used in section 3.3.1, identified hereafter as LNO_800. To be concise in the identification of samples, the terms “Mech” and “Copr” will be applied, referring to mechanofusion and coprecipitation, respectively. Also, the label “Cycled” will be used to separate the cycled-state materials from the pristine ones.

3.2.2 Electrochemical measurement

To produce cathode electrodes, synthesized powders were mixed with polyvinylidene difluoride (PVDF) and Super-S carbon black from Timcal in a 92:4:4 weight ratio. Then, N-methyl-2-pyrrolidone (NMP) was mixed with the above powder for 300 s, in a 1:1 weight ratio, to form a slurry which was then cast on the aluminum foil via a 150 µm notch bar. After leaving the coated Al foils to fully dry at 120 °C under the laboratory room environment, the samples were calendared under 2000 atm pressure. Next, the prepared

electrodes were cut into 12.75 mm diameter circles and placed under vacuum for about 16 hours (overnight) at 120 °C temperature. All the coin cell assembly was done inside a glove box in an Ar atmosphere. In each coin cell, beside the produced cathode electrode, a Li metal foil, two layers of Celgard#2300, as well as 1.2 M LiPF6 (lithium hexafluorophosphate) in a 1:4 volume ratio of FEC (fluoroethylene carbonate) /DMC (dimethyl carbonate), were used as the anode electrode, separator, and electrolyte, respectively. An E-one Moli Energy Canada battery test system was used for electrochemical cycling measurements of coin cells at 30 °C temperature. The cycling test was set between 3.0 V and 4.3 V vs. Li^+/Li, with two different C-rates. Two first and last cycles had a C/20 rate, and 50 cycles in between were run at a C/5 rate. Before starting any analysis, cycled materials were disassembled from coin cells, washed with DMC, and fully dried in an Ar-glovebox.

3.2.3 Synchrotron-based X-ray Diffraction (SXRD) and Pair Distribution Function (PDF)

Both SXRD and PDF analysis were acquired on the high-energy wiggler beamline of the Brockhouse X-ray diffraction and scattering sector at the Canadian Light Source (CLS) in Saskatoon, Canada. The X-ray energy was set at 30.3383 keV and 65 keV for SXRD and PDF, respectively. For PDF, higher energy (i.e. shorter wavelength) was selected to collect a higher wave vector and better distinguish between different bonding distances in real space [32]. In this work, a relatively high Q_{max} (26 A^{-1}) was resolved.

Cycled materials were measured in the electrode form (on the Al foil); however, pristine powder samples were put into polyimide capillaries. To calibrate the SXRD detector, a nickel powder was used as a reference.

3.2.4 Scanning Electron Microscopy (SEM) and Energy-Dispersive X-ray Spectroscopy (EDS)

To better understand the average morphological changes in cathode materials, a Thermofisher Helios G4 Plasma-Focused Ion Beam (PFIB) was used to prepare SEM cross-sections, acquire elemental mappings via EDS, as well as make thin lamellae for further analysis with a Transmission Electron Microscope (TEM). To obtain a wider cross-sectioning area and reduce the milling time, higher ion currents were used first, with subsequent milling using reduced current settings until the end of the process, although some residual curtaining remained on the finishing surface. A pre-tilt sample holder (45°) was used for cross-section milling. Higher resolution SEM images were acquired in immersion mode with low voltage and beam current (2 kV-50 pA and 1 kV-0.1 nA) to detect surface features as much as possible. EDS analysis was done at 10 kV acceleration voltage. For TEM sample preparation, carbon layers and subsequently thicker W layers were applied on the surface of the areas of interest through electron- and ion-beam-induced deposition in the PFIB, respectively, before the lift-out of a chosen particle at the top of the electrode. A tungsten protective layer with high milling resistance is desired for optimal sample preparation. This step did not affect the W distribution inside the doped particles. This matter was confirmed using the same protection layers on a sample without any W dopant, which did not show any trace of W within the particle.

3.2.5 Scanning Transmission Electron Microscopy (STEM) and Electron Energy Loss Spectroscopy (EELS)

Detailed analysis by TEM was conducted using STEM for high-resolution imaging through a High-Angle Annular Dark-Field (HAADF) detector, as well as EELS for determining, with high spatial resolution, the distribution of elements as well as any changes in their

chemical state in the sample. An FEI Titan 80-300 microscope fitted with two aberration correctors and operated at 200 keV was used for this work. For acquiring STEM images and EEL spectra, 19.1 mrad convergence semi-angle and 55 mrad collection-angle were used, respectively. A direct electron detector Gatan K2 Summit® was required to enhance the signal quality of EEL spectra when the beam current was reduced to minimize electron beam irradiation damage. Some statistical and data processing methods, namely, Principal Component Analysis (PCA) and Multiple Linear Least Squares (MLLS), were used for noise reduction of the EELS signal and separately fitting the whole spectrum based on different O K-edge shape references, respectively.

3.2.6 X-ray Absorption Fine Structure (XAFS)

The XAFS experiments were performed with the Hard X-ray Micro-Analysis (HXMA) beamline at CLS. Si crystals with different orientations (220) and (111) were used to produce a monochromatic beam and to select the appropriate energy to acquire Ni K and W L_3 absorption edges separately. XAFS data for this work were acquired in both modes, fluorescence (13 element Ge detector) and transmission (Oxford straight ion chamber detectors).

3.3 Results and discussions

3.3.1 Electrochemical behavior

The cycling behavior of LNO from two different heat treatment temperatures (700 °C and 800 °C), as well as different enrichment levels (1%W and 2%W) in LNO from two synthesis procedures (mechanofusion and coprecipitation), are shown in Figure 3-1(a-c). As can be seen from Figure 3-1(a), for the initial cycle at C/20, the W-enrichment reduces the capacity of the cells in comparison to the undoped samples treated at the lower

temperature. However, the retained capacity after cycling is recovered in W-enriched materials (Figure 3-1(b)), especially at the 1% W concentration level prepared by mechanofusion, since the voltage hysteresis between charge and discharge curves after several cycling is reduced.

The pure LNO sample (Figure 3-1(a)) shows many steps in its voltage profile due to the several phase transformations from H_1(Hexagonal) to M (Monoclinic), M to H_2, and H_2 to H_3 crystal structure; however, this discontinuity (step shapes) in voltage is not desirable. In the enriched coprecipitated particles (as shown in Figure 3-1(b, c)), the capacity retention over 54 cycles still seems steady despite having lower charging and discharging capacity compared to the undoped material synthesized at 700 ^{o}C. The best performance among these materials is demonstrated for the 1%W_Mech sample, with a low voltage hysteresis. Figure 3-1(d) shows the comparison between the dQ/dV vs. V profiles of the first and last cycle (with C/20 rate) for 1%W_Mech material related to the critical phase transformation from the H_2 to the H_3 structure. The difference between the location of these peaks is reduced in higher cycle numbers, and the intensity remains almost unaffected. These effects are good indications of the stabilized structure and durability of the cathode during cycling.

A comparison of LNO samples produced following 700 °C and 800 °C heat treatments shows a reduced delivered capacity for the higher temperature treatment (Figure 3-1(c)). However, the 800 °C heat treatment provides a better outcome for the enrichment procedures [28], and those enriched structures show higher and more stable capacity retention after cycling, with only a small amount of W. In pure LNO at 800 °C, the particle size growth could not be prevented without W present, leading to poorer kinetics and, therefore, lower capacity in those materials. The crystal structure tends to decompose and

return to a rock salt phase through various steps at high temperatures (around 700 °C and higher) [33]. The pace of this phase transformation increases with higher temperatures and drastically slows down under O_2 or air atmosphere [33] (here, the lithiation is conducted under oxygen gas flow). In W-containing materials, specially prepared with mechanofusion, it appears that the presence of W likely reduces this unwanted reaction by protecting the surface of these Ni-rich materials, which is the most vulnerable location for decomposition.

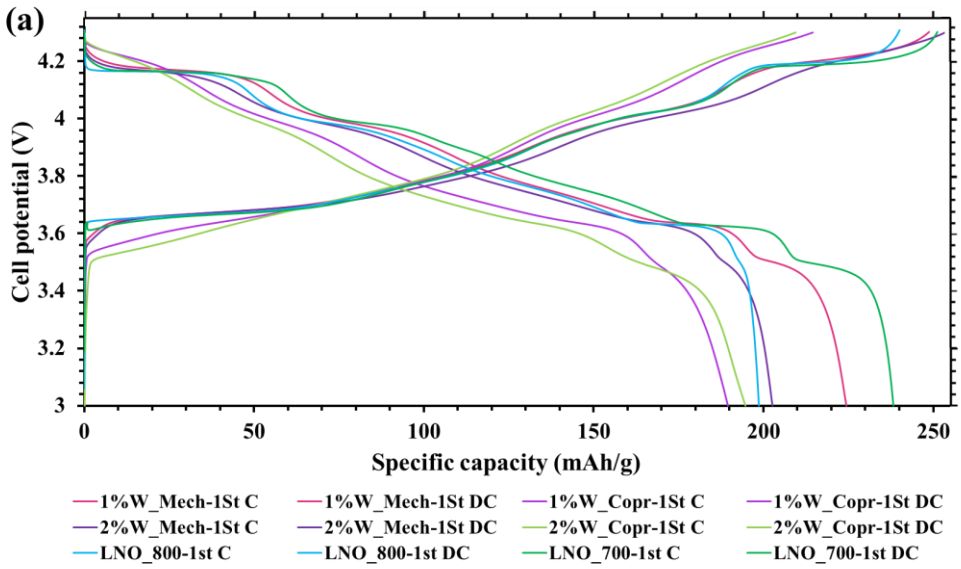

Figure 3-1 (a) and (b) are the first and the last (54th) charge and discharge voltage profiles at C/20 rate between 3.0 V-4.3 V, respectively. (c) Cycling performance of samples with two first and last cycles at C/20 rate and 50 cycles at C/5 rate. (d) Comparison between the first derivative of the 2nd charge and 1st discharge curves, as well as the 54th charge and 53rd discharge curves for 1%W_Mech where the H_2 to H_3 transformation occurs. Labels C and DC here refer to the charging and discharging process, respectively.

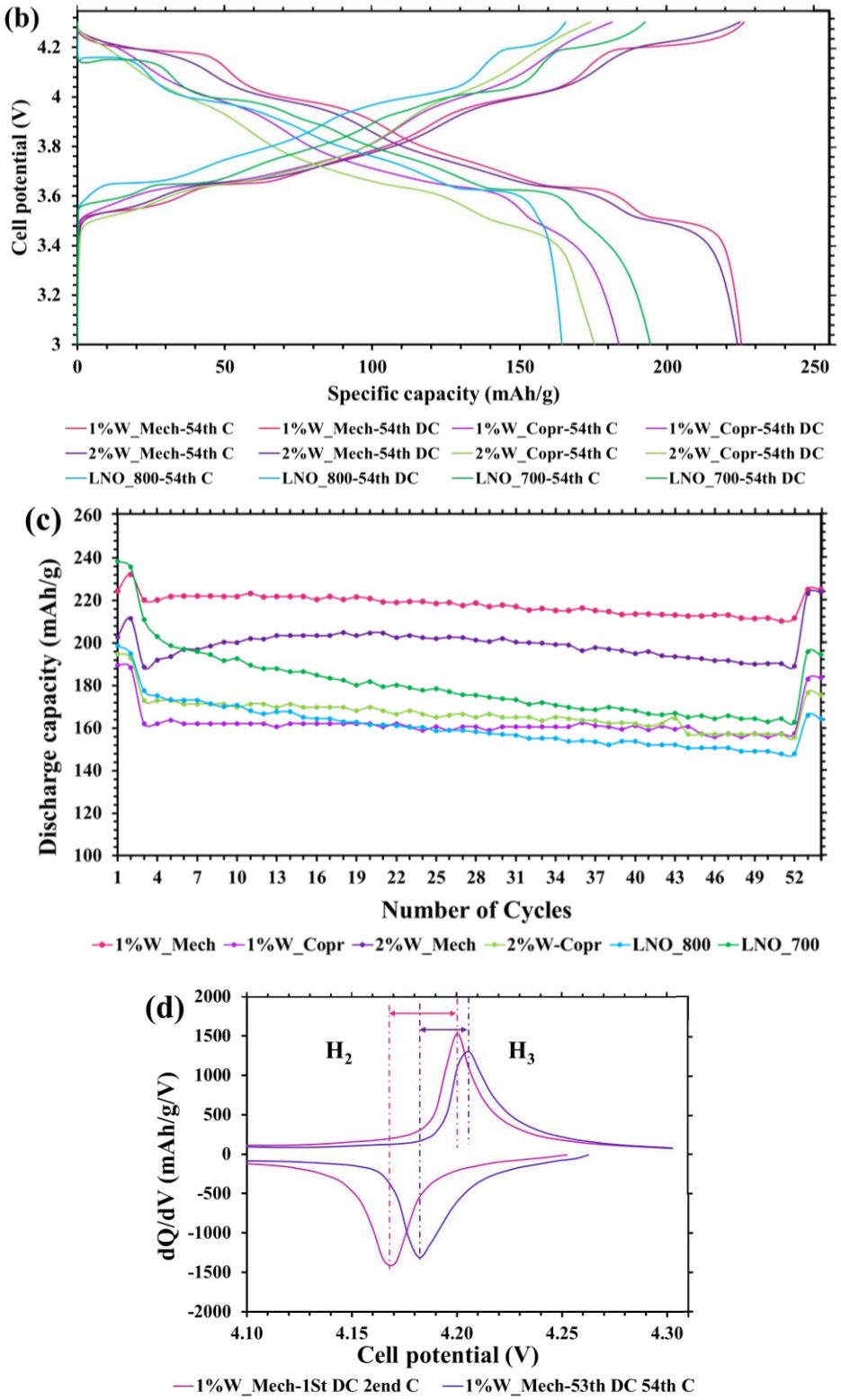

Figure 3-1 Continued.

3.3.2 XRD and PDF

Cycled electrodes made of materials coated on Al foil current collectors were extracted from coin cells and studied via XRD, Figure 3-2. These cycled cathodes have higher background than pristine materials due to the presence of the Al foil which introduces more scattering than regular capillary sample holders. The patterns also exhibit a sloping background (below 30° 2θ angles) which is an indication of the presence of amorphous compounds. This latter contribution could be due to the formation of the Cathode Electrolyte Interphase (CEI), of other side reaction products during cycling, as well as from the presence of fillers (i.e. PVDF), etc. . This sloping background covers almost all the minor extra peaks expected due to the presence of new W-compounds ($Li_{4+x}Ni_{1-x}WO_6$, x=0 and 0.1 with C2/m and Cm space group symmetry, respectively) as discussed in our previous work [30].

Table 3-1 summarizes the XRD fitting results by considering only LNO and Al as possible phases since the other present phases did not display peaks of sufficient amplitude or sharpness to be adequately fitted. Consequently, our discussion is only focused on the effect of cycling on the major peaks of LNO structures. The residual fitting values of the Rietveld refinement shown in Table 3-1 are therefore higher than those obtained from the XRD analysis of pristine materials because of the overlap of Al and $LiNiO_2$ (with the $R\bar{3}m$ layered structure) peaks, the texture in Al foil, as well as the omission of any other minor phases which are within the sloping background area.

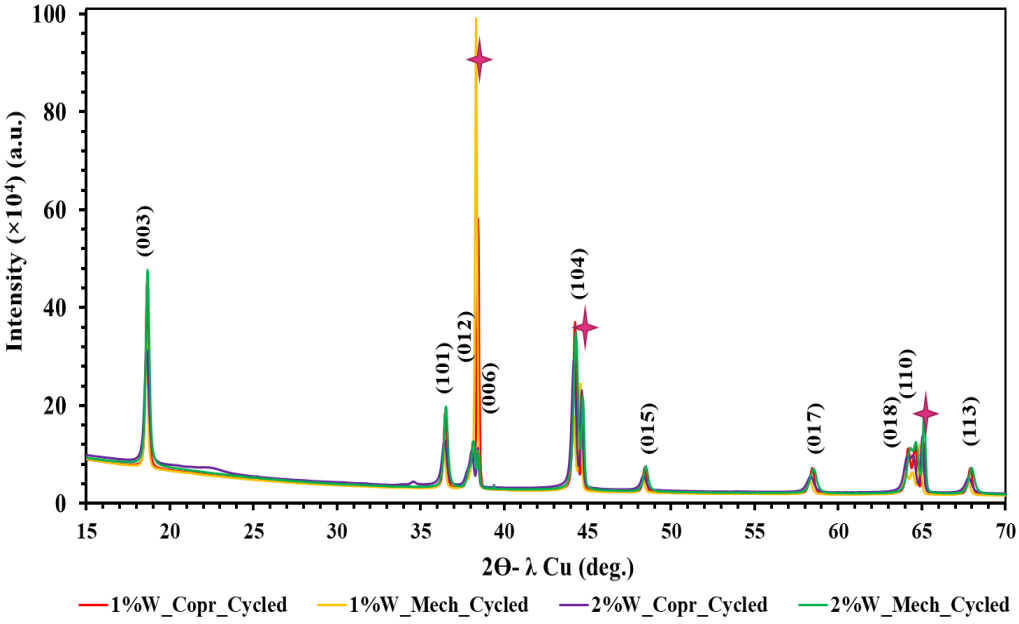

Figure 3-2 Synchrotron XRD patterns for cycled W-enriched materials from mechanofusion and coprecipitation methods. Red stars illustrate the locations of Al peaks. The 2Θ angles of the patterns are converted to the copper's $\lambda_{k\alpha}$ for comparison purposes with the literature.

The first observation on the high-resolution synchrotron XRD is the broadening of some major LNO peaks following cycling. The peaks that best exemplify this broadening in the XRD patterns are the (003) and (101) reflections of LNO which both show higher widths in cycled materials. There are two possible contributions to this broadening: the grain size and the residual strain. Since the grain size in fully discharged particles would be expected to be the same as pristine, uncycled particles, this increased width might be caused by residual strain inside the cycled materials. This assumption would be reasonable because, even in the presence of cracks inside the cycled particles, most of the cracks propagate through the grain boundaries between the primary particles, which would not affect the measured size by XRD (primary particles are the smallest coherence domains).

Furthermore, since strain build-up occurs first and complete cracking would require more extended cycling, for the 54-cycled samples, it would be fair to assume the presence of residual strain, rather than grain size changes, to be the cause of this broadening. The (003) peak reflects changes in the c lattice parameter, and it has been shown that this lattice parameter changes abruptly at a high state of charge, especially inside the Ni-rich cathode materials [14,26]. A second effect observed from the analysis of the major peaks, compared to the pristine samples investigated in our previous work [30], is the higher level of cation mixing in cycled materials revealed by the occupancy ratio Ni (on Li site)/Li, shown in Table 3-1(Ni/Li%) (For instance in LNO_1%W_Mech, the Ni/Li% is 2.77% [30]). This indicates some degradation in the layered structure of the cathodes after cycling.

Table 3-1 Rietveld refinement results based on the cycled materials.

sample name	Phases Wt. fractions		LNO's Lattice parameters		Atom's occupancy inside LNO		Ni/Li %	Rw%
	LNO	Al	a (Å)	c (Å)	Li	Ni (on Li site)		
1%W_Mech_Cycled	0.38	0.62	2.88787	14.25596	0.9545	0.0455	4.77	10.56
2%W_Mech_Cycled	0.85	0.15	2.87947	14.21441	0.919	0.081	8.81	10.75
1%W_Copr_Cycled	0.62	0.38	2.88242	14.23713	0.909	0.091	10.01	7.87
2%W_Copr_Cycled	0.81	0.19	2.88743	14.25614	0.892	0.108	12.11	9.65

Our previous work on the effect of W additions on pristine LNO has shown that no major changes in the PDF of LNO structure were detected [30]. However, some important effects can be highlighted in the PDF patterns when considering the impact of cycling. The PDF analysis was therefore used to extract further details on the cycling effects regarding the bonding distances between the atom pairs of the W-enriched LNO cycled bulk phase. The full pattern analysis of the entire bonding distance range is not possible here due to overlapping Al-Al bond pairs with almost all the LNO distance pairs (Figure 3-3(a)). The first peak, marked (1) on the PDF, however, corresponds only to the LNO phase and does

not present overlap with Al. This peak represents Ni-O, and Li-O bonds. The comparison of the first peak between each W-enriched material in its pristine state and after cycling (Figure 3-3(b,c)) shows that in all the cycled materials, peak (1) at ~ 1.98 Å, shifts to a lower bonding distance, r, and in both materials prepared by coprecipitation, some level of distortion in their peak shape can be detected. The reduction of Ni-O bonding distance is expected during the charging process (i.e., delithiation) because of the higher oxidation level of Ni. Furthermore, the Li-O bonding distance general behavior is comparable to the c lattice parameter trend, with expansion up to some charge level and sudden extraction at a critical charging state [13]. These two opposite trends (expansion and extraction) arise from the reduction of the Li^+ screening effect at the beginning of charging, which is necessary to keep the Ni-O interlayer closer to each other, which results in c-axis expansion, as discussed in [13]. At a higher level of charging, it has been shown that Ni and O (3d orbital state and 2p orbital state, respectively) hybridize effectively and cause a sudden reduction in c lattice parameters [13]. Therefore, in the high charge state, both a and c lattice parameters decrease and generate a contraction inside the lattice. Subsequently, during discharge, the reverse process is expected. The shifting of the peak at ~ 1.98 Å in the PDF pattern, towards shorter bonding distances, suggests that in cycled materials (after 54 cycles), the structural change is not fully recovered during their following discharging process (especially at the beginning of the discharge [13]), and this could be due to the separation or isolation of some active materials from the conducting additives network or current collector which could cause a reduction in the capacity.

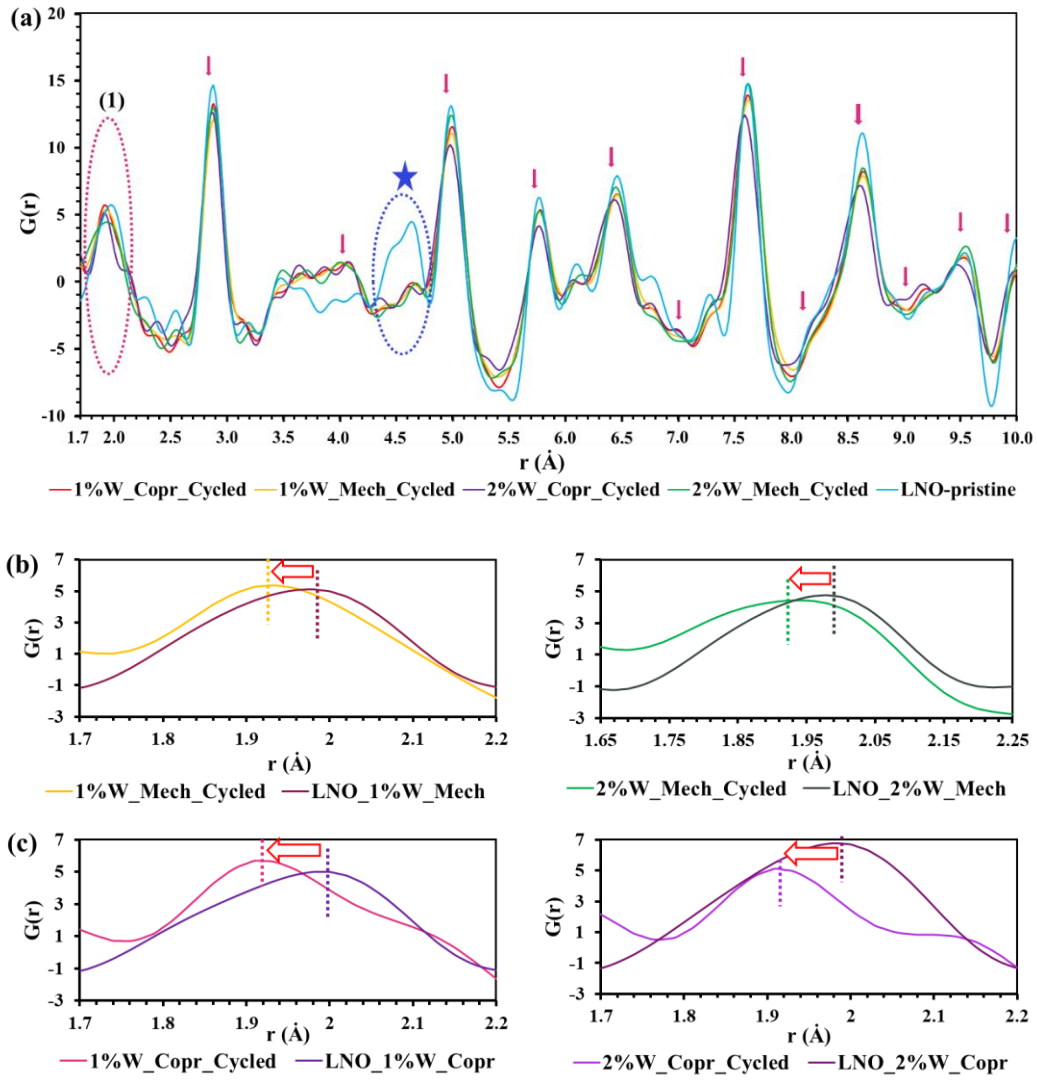

Figure 3-3 (a) The comparison between the pair distribution function of W-enriched cycled materials and pure LNO in the local structure domain (1.66Å -10Å). The red vertical arrows show the location of aluminum's bonds from the current collector in the electrode samples, and the red dotted oval shape, marked (1), illustrates the position of the first peak separated from aluminum's bond pairs. Also, the blue dotted oval shape, marked with a star, shows the major damping in the PDF peaks. (b) and (c) show more detailed views of the pair distributions corresponding to the first selected peak in (a), versus the pristine state of each material prepared through the mechanofusion and coprecipitation, respectively. The dotted lines and horizontal arrows exhibit the peak shifting toward the lower bond distance r-position in cycled materials.

A second bonding pairs range that does not overlap with Al shows significant changes to the pristine material (Figure 3-3(a)) and is identified with a star in the r-range around ~4.25 Å to ~4.8 Å. Here the intensity of the PDF peaks significantly decreases. Based on the previous study on doped materials in the pristine state [30], the W-enrichment generates no major changes in the PDF peaks of LNO. Therefore, this significant damping in this bond-distance range can only be caused by cycling effects. Based on the LNO layered structure, two main pair bonding distances are located in this mentioned range, O-Li (~4.47 Å and ~4.58 Å) and O-Ni (~4.47 Å, ~4.52 Å, ~4.58 Å and ~4.66 Å). These bonding distances could also be affected by changes in the d-spacing of Li and Ni layers which are about 4.73 Å. In the above bond pairs, oxygen is the common element, and since there is no participation from oxygen in the electrochemical chemical reaction and no major changes were detected due to the addition of W, one possible explanation for this damping could be some level of oxygen release.

3.3.3 SEM cross-section and EDS mapping and fracture analysis

To better analyze the overall effect of cycling on the morphology, elemental distribution, and fracture of the particles inside the cathode electrode, SEM imaging, following cross-sectioning with PFIB, and EDS mapping were carried out. In Figure 3-4(a), most of the secondary particles in the 1% W-enriched material prepared by mechanofusion after cycling (1%W_Mech_Cycled) stay intact, while the remaining cracked particles are mainly located on the top of the electrode. The cracking of particles at the top of the electrode may originate from the electrode preparation process which includes electrode calendaring and contact with a roller, as well as through cycling because of their more direct exposure to the electrolyte. These secondary particles show high packed density. PFIB cross-section of an individual particle extracted to prepare thin lamellae (Figure 3-4(a-vi)) shows that,

within the particle, cracks are mostly located within the core of the particle. As expected, during the charging process, both surface and core of the secondary particles lose Li and experience massive volume shrinkage, notably in Ni-rich materials and at the end of the charge (change in volume of LNO: $\Delta V_{LNO} \approx$ -9.38% [26,34]). The surface is expected to lose Li first since it is in contact with the electrolyte, where the reactions initially occur, and diffusion out of the particles is faster compared to the core. This causes the volume change and shrinkage initially, more than the core section, generating tension on the surface and compression at the core level, as discussed in [13]. The reciprocal effect of these volume changes and induced stresses occurs during discharging, which puts the core of the particle under tension, resulting in the initiation and growth of cracks over multiple cycles. In Ni-rich cathode materials, most of the fractures occur through grain boundaries [13,34]. Based on Figure 3-4(a), it appears that the presence of W-rich areas in the grain boundaries demonstrated in our previous work [30] improves the structural integrity of the secondary particles, suggesting an increase in the toughness of the secondary particles and better accommodation of cycling stress without cracking. In previous work by the authors, it has been shown that by increasing the concentration of W from 0 to 1% in LNO through mechanofusion, both the compression resistance or strength, as well as retained capacity are improved [29]. The reduction of stress inside the electrode can also affect the electrochemical behavior of these materials based on thermodynamic arguments. For example, in previous work, it has been shown that higher internal strain would consume some part of the necessary energy for the charging and discharging phase transformation toward elastic-plastic deformations and change the equilibrium potential (for charge and discharge reactions) [36,37]. These phenomena increase the hysteresis cycling behavior and reduce the electrochemical energy of the cell. In our case, the presence of W-

compounds at the/near the grain boundaries within the secondary particles, with the ability to accommodate some part of the volume change, would aid the phase transformation and reduce the potential hysteresis in W-enriched materials.

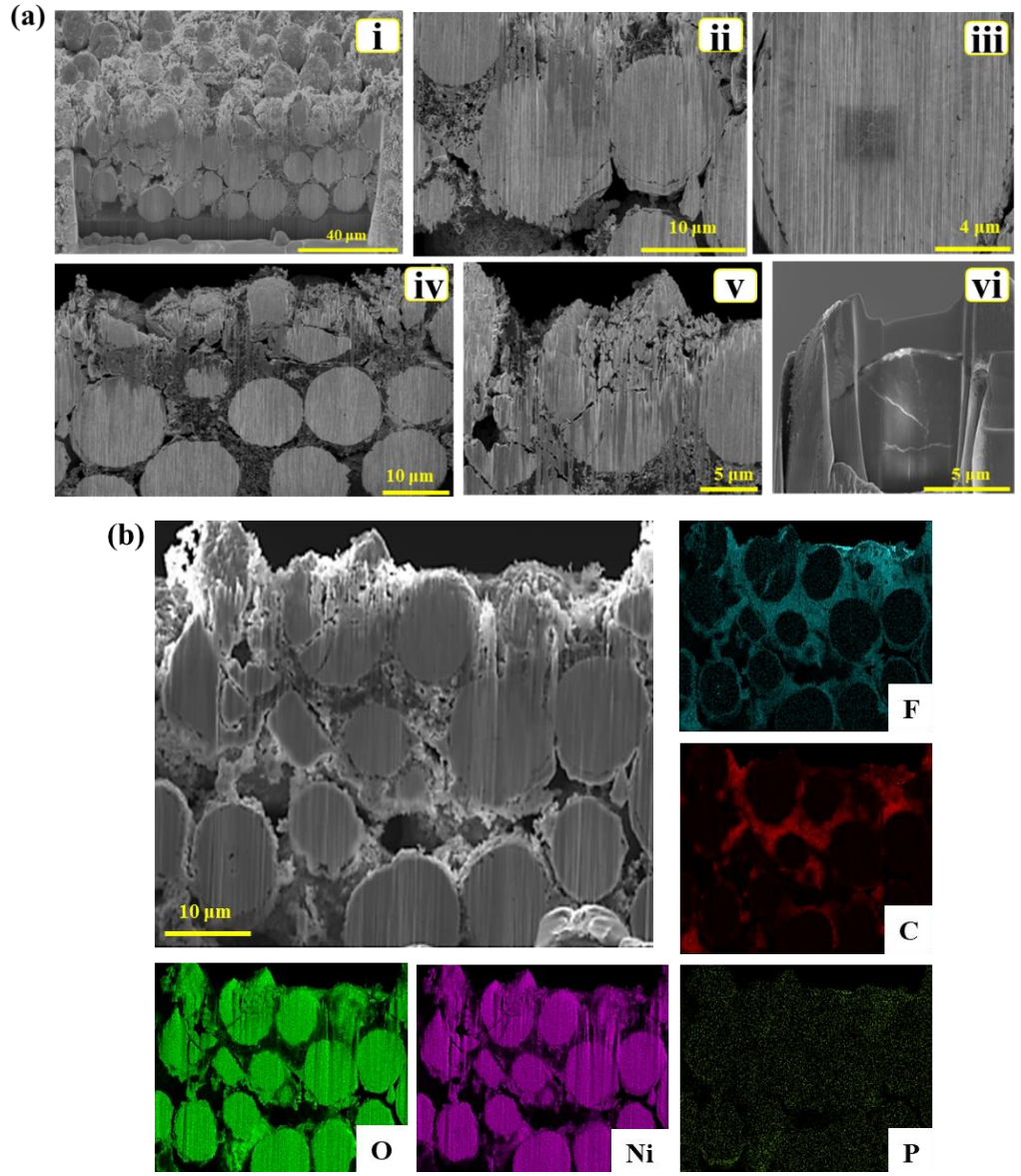

Figure 3-4 (a) cross-sectional views of 1%W_Mech_Cycled, in the electrode shape after 54 cycles. "i-v" show the overview and detailed views of multiple high-resolution SEM cross-section images as well as "vi" which illustrates PFIB lamellae, and (b) the corresponding EDS maps revealing the elemental distribution due to the cycling process.

Based on Figure 3-4(b), due to the reduced cracking as discussed above and highly packed and dense particles, reactions with the electrolyte are limited and mostly occur on the surface of the secondary particles (see the elemental distribution of fluorine in EDS mappings). However, due to the large interaction volumes of X-ray, and poor detection limits in EDS, the accurate W distribution is not detected (hence the W map is not shown). Overall, based on Figure 3-4(a,b), the 1%W_Mech_Cycled material shows good resistance to fractures and side chemical reactions (evidenced by the presence of fluorine and phosphorus mostly outside of the secondary particles), making this material exhibit the best performance among other samples in this study.

As can be seen from Figure 3-5(a), the secondary particles in the 1%W_Copr_cycled materials are smaller and have a higher level of porosities, clearly more visible in the FIB cross-sectional sample, Figure 3-5(a-vi), as compared to the sample prepared by mechanofusion (1%W_Mech_Cycled). There are two possible contributions to the higher level of porosities in the samples which have been prepared by coprecipitation to reach W-enriched precursors. First is the contribution of the W-rich phases at the grain boundaries, leading to a change in the kinetics of grain boundaries' mobility, resulting in gaps between grains (more clearly visible in Figure 3-6(d)). The second contribution could be attributed to the Kirkendall effect because of the opposite direction and different speed of diffusion between Ni (speedily outward) and O atoms (gently inward), producing inner voids or cavities due to the supersaturation of interior vacancies during the synthesis of the samples [38–40]. Since these porosities appear to be between the primary particles (see further evidence in Figure 3-6(d)), the likely origin is the synthesis process which would require optimization to completely suppress the many porosities present in the particles' core, as seen in Figure 3-5(a), and develop more dense secondary particles. The rate of chemical

side reactions in 1%W_Copr_Cycled materials increases due to the higher levels of porosities (hence affecting the particle integrity during cycling), which is visible from Figure 3-5(b), with fluorine detected even within the core of particles (see further results in section 3.3.4). Accordingly, the detrimental effect of porosities (due to the not optimized synthesis process) ultimately make coprecipitated particles more vulnerable to electrochemical side reactions.

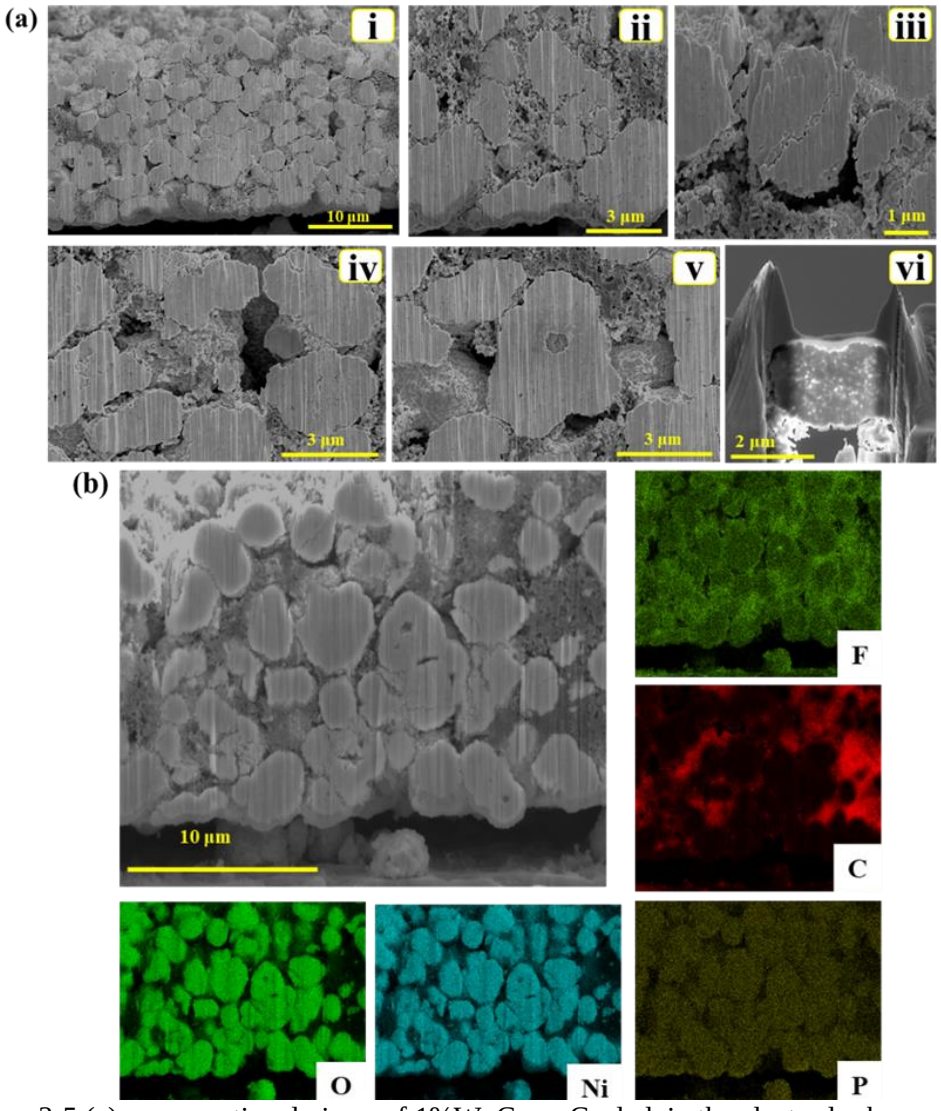

Figure 3-5 (a) cross-sectional views of 1%W_Copr_Cycled, in the electrode shape after 54 cycles. "i-v" demonstrate several views of multiple high-resolution SEM cross-section images and "vi" points out the PFIB lamellae. (b) The obtained EDS maps.

3.3.4 EELS and STEM

For higher spatial resolution investigation of the elemental distribution in cycled materials and better visualization of cycling effects on the samples, EELS analysis was carried out. Two generally different behaviors are identified in samples prepared by mechanofusion and coprecipitation. In the W-enriched LNO from the mechanofusion process, W is detected on the top surface of the secondary particle and also inside the grain boundaries, as shown in previous work [30]. In the 1%_Mech_Cycled sample, based on the presence of fluorine and phosphorus-rich areas on the surface of the particle (Figure 3-6(a)), it appears that this W-rich layer on the surface of the secondary particles plays a protective role between LNO and the electrolyte, and limits the side reactions to the very surface. The effect of cycling can also be deduced from the changes in the EELS O K-edge shape in Figure 3-6(b, c). The O K-edge in pure LNO has two main features: 1) the pre-edge peak below 530 eV, which is the transition from O 1s to the hybridized state of O 2p and Ni 3d unoccupied states, and 2) the main peak resulting from the transition between O 1s and the hybridized state of O 2p with the Ni 4sp unoccupied states. Any kind of structural change affecting the hybridization state of the first mentioned transition, such as altering crystal structure or local chemistry, can provoke the suppression of the pre-edge [30,41]. Using this pre-edge peak as a probe of the transformation, the EELS maps show areas where the O K-edge pre-edge is absent and has a broader shape inside the CEI layer. These maps show that the most affected regions are located just near the surface of the secondary particles as well as in areas adjacent to open cracks, Figure 3-9S. Although, the W is not present as a uniform distribution within LNO, the resulting heterogeneous distribution of W appears to be very effective in protecting the integrity of secondary particle by limiting the cyclic effect to the very surface.

On the other hand, the 1%W enriched sample, prepared through the coprecipitation process, with synthesis conditions still generating high levels of porosities, shows significantly more degradation Figure 3-6(d-f). The occurrence of a massive transformation, as evidenced by changes in oxygen K-edge shape, can be seen in Figure 3-6(e,f), further away from the surface, near the core of the secondary particle (Figure 3-10S(b,c)). Because of the significant number of porosities in the particles produced by coprecipitation, side reactions can then occur deeper within the particles via electrolyte infiltration facilitated by porosities. The surface reaction layer in 1%W_Copr_Cycled seems thinner than 1%W_Mech_Cycled. Still, having primary particles covered by W partially reduces the reaction level just near the primary particles' periphery, Figure 3-10S.

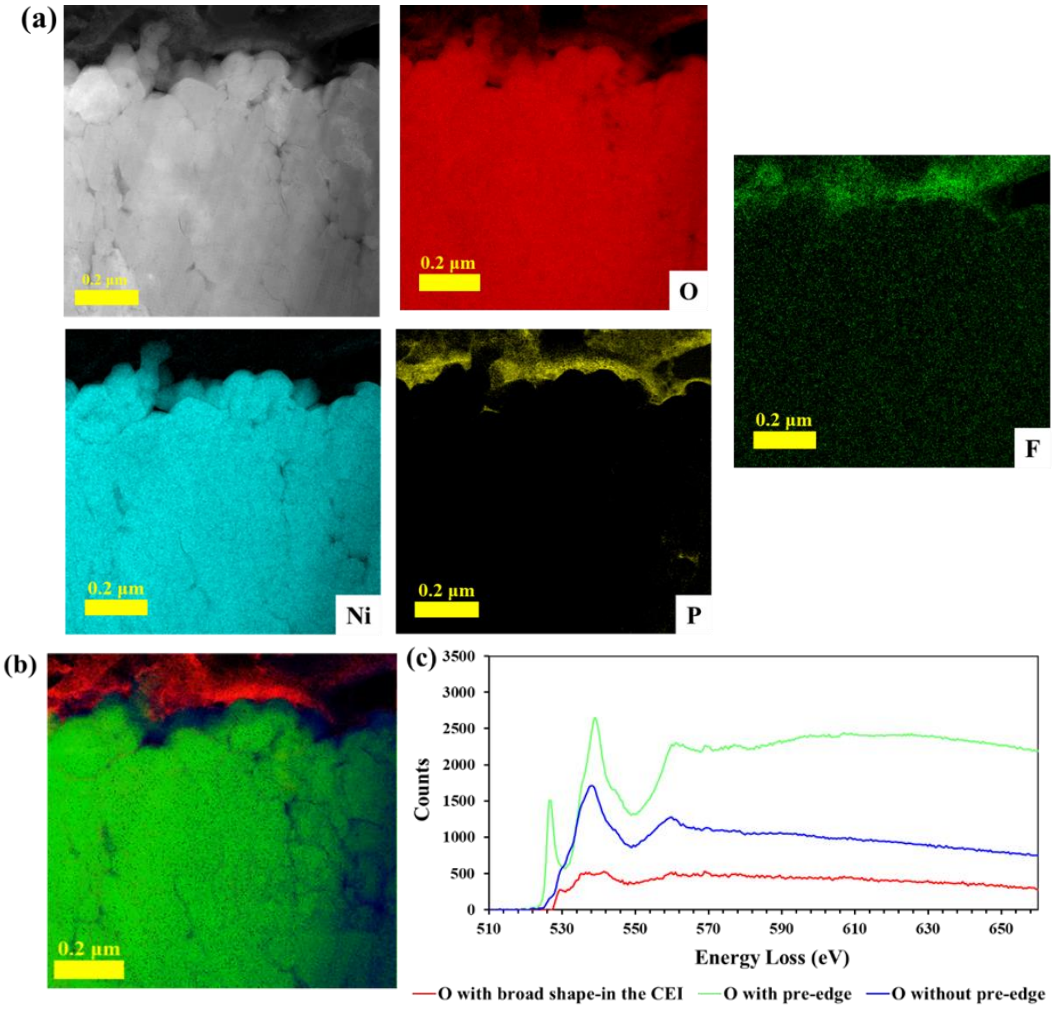

Figure 3-6 The Annular Dark Field (ADF) images, EELS maps and spectra related to different shapes of the O K-edge peak with respected Red Green Blue (RGB) composite images illustrate for (a-c) 1%W_Mech_Cycled's, and (d-f) 1%W_Copr_Cycled's secondary particle. In (a) the EELS maps show the P K-edge peak clearly visible, but it is not clearly detectable in 1%W_Copr_Cycled, due to the noise level, the P map is not shown in (d). For clarity in the F map given the noise level, the spectrum F K edge extracted from the "I" area is also shown in (d). (c) and (f) illustrate three different shapes of the O K-edge peak, with a broad shape peak inside the CEI/reaction layer, in red, without a pre-edge peak in blue, and with a pre-edge peak in green. (b) and (e) illustrate the RGB images based on the color of spectra in (c) and (f), respectively. The red circle inside image (d) identifies the grain selected for more detailed STEM analysis in Figure 3-11S.

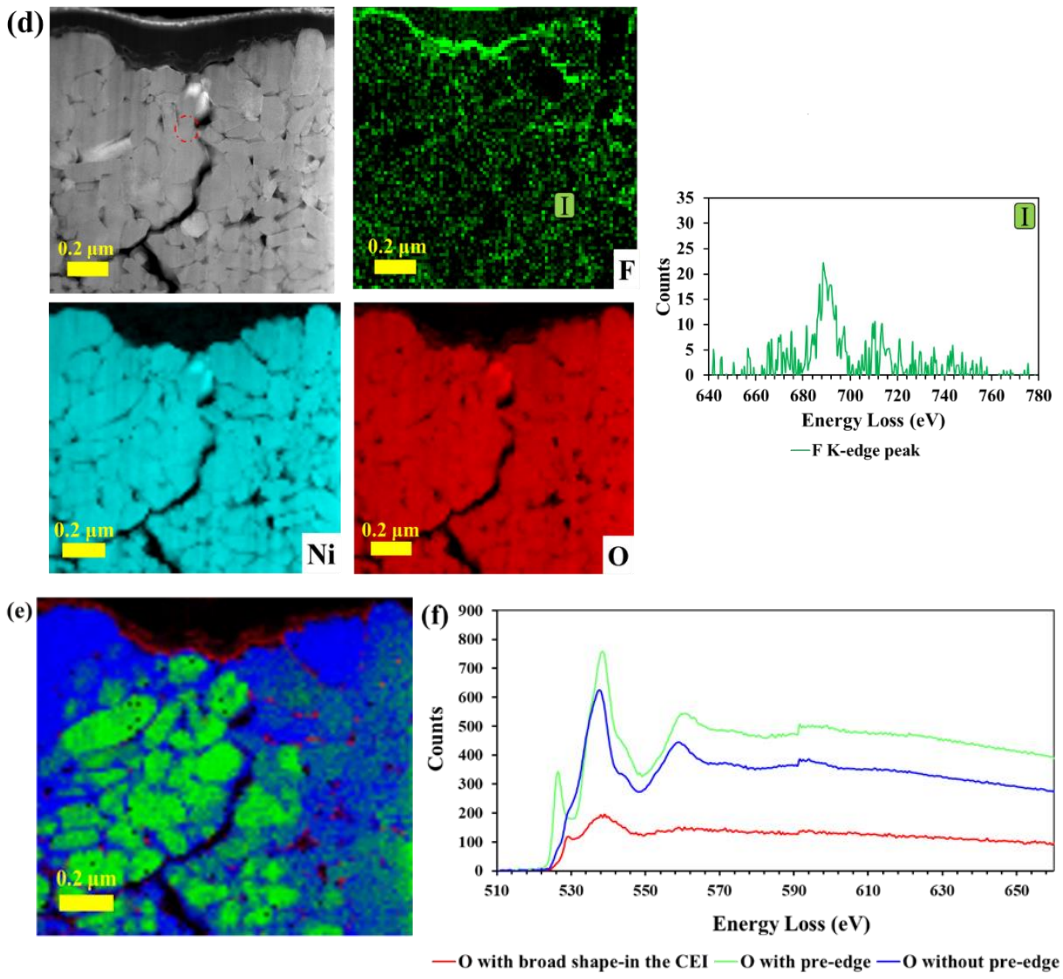

Figure 3-6 Continued.

For a detailed analysis of the cycling impact at the atomic level of cathode materials, high-resolution STEM HAADF imaging was utilized. Figure 3-7 illustrates the cycling effect on 1%W_Mech_Cycled material from two different selected primary particles (their positions are marked in Figure 3-9S(a)). Figure 3-7(a) shows the atomic resolution image and its Fourier Transform (FT) in the inset from a primary particle located just beneath the very surface of the secondary particle (region I in Figure 3-9S(a)). Since the calculated FT has 6-fold symmetry for the orientation of this particular grain, other complementary evidence is needed to identify whether the layered or spinel structure is present. The RGB

image (Figure 3-9S(b,c)) based on the O K-edge peak shapes shows evidence of a pristine structure for area "I", due to the presence of the O K-edge with a strong pre-edge peak (shown with green color). Also, for the pure spinel phase, more reflections would be expected on the <111> zone axis. The FT diffraction pattern also fits well with the <001> zone axis of the layered LNO crystal. Given this combined evidence, it is possible to deduce that close to the surface of the secondary particles in 1%W_Mech_Cycled material, the pristine LNO structure is still present. The presence of superlattice reflections (i.e. the extra spots marked with red circles in the FT patterns) can be interpreted as evidence of ordering, possibly due to the early onset of phase transformation to the spinel phase. The interatomic spacing (Figure 3-7(b)) is also consistent with the LNO crystal on the <001> zone axis in Figure 3-7(a). On the other hand, HAADF imaging of a grain located near the very surface of a secondary particle, Figure 3-7(c), (from region II in Figure 3-9S(a) where the O K-edge pre-peak is absent particularly closest to the surface), shows that cycling alters the crystal structure into the spinel phase, this time viewed on the <001> zone axis. The spacing from the FT pattern is consistent with the expected interplanar spacings from this orientation, also shown in the HAADF intensity line profiles (Figure 3-7(c, d)). The {220} reflections in the FT pattern, expected from a selected area diffraction pattern, however, are not detected, possibly due to the lower sensitivity to ordering in HAADF imaging.

In the porous sample (1%W_Copr_Cycled), regardless of the inner position of the selected primary grain, the cross-section of the sample reveals the spinel structure near the secondary particle's porosity (Figure 3-11S). This result is consistent with the capacity results showing more degradation in samples prepared by coprecipitation, due to the high level of porosities.

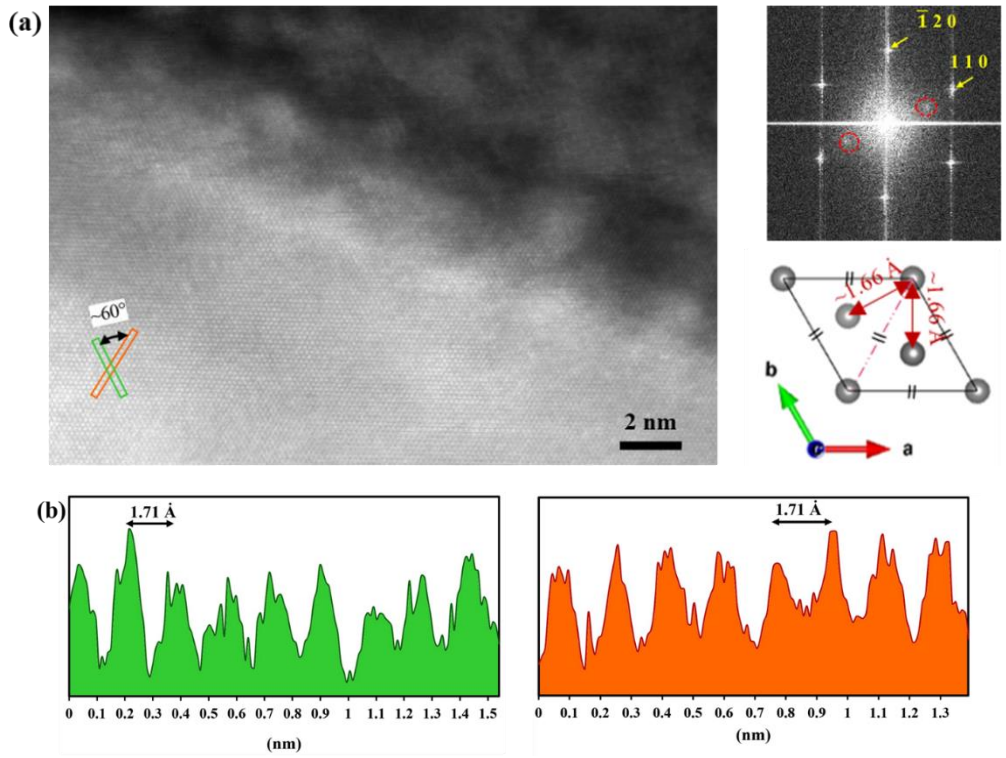

Figure 3-7 Detailed High-Angle Annular Dark-Field (HAADF) imaging of two areas marked I and II in Figure 3-9S(a) from the 1%W_Mech_Cycled sample. (a, b) and (c, d) show HAADF image, FT with fitted indexes and related intensity line profiles with the same colors as marked inside HAADF image, from areas marked I and II, respectively. (a) and (c) also contain the 2D crystals model projections with the related zone axis orientations, layered structure with <001> zone axis displays some orderings marked by red dotty circles and spinel structure with <001> zone axis, respectively. Model structures with Ni and Li atoms in crystal cells are gray and green, respectively.

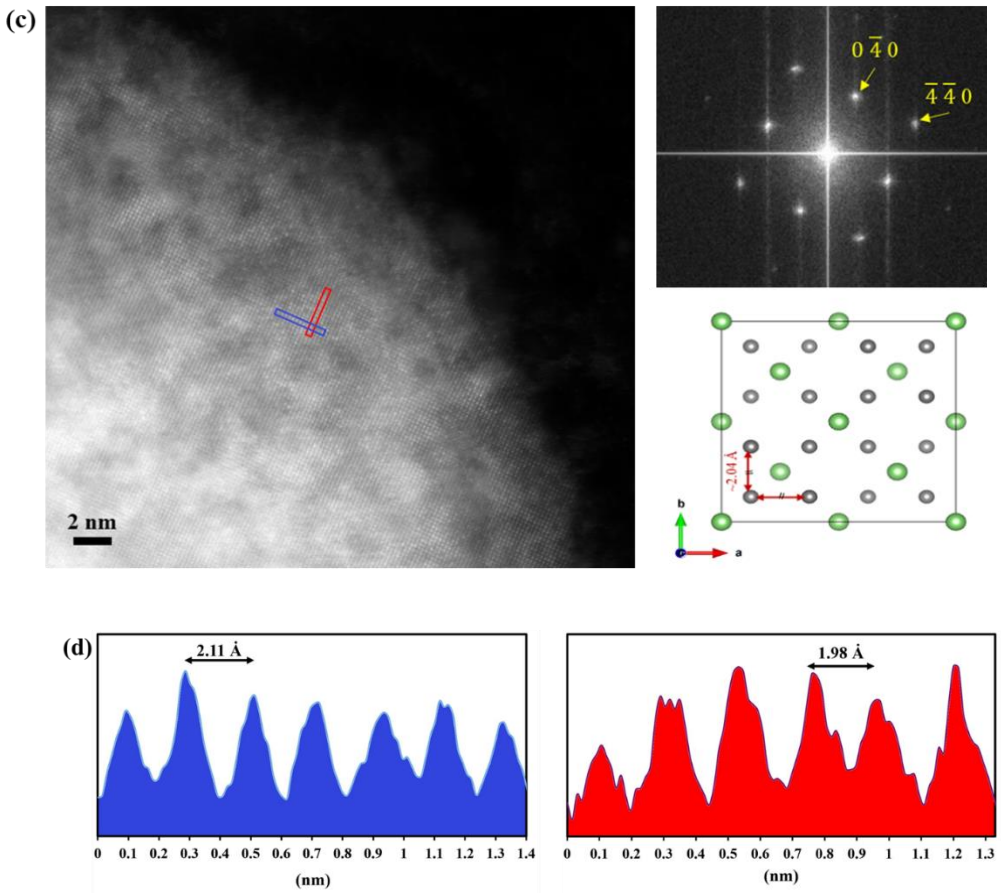

Figure 3-7 Continued.

3.3.5 XANES analysis

For more bulk-sensitive chemical analysis of the cycled materials, XAFS measurements were carried out. The XAFS spectra effectively probe the Ni and W atoms' environment. To better detect evidence of changes in the environment of Ni atoms after cycling, due to the low W-enrichment level compared to the amount of Ni, a sample with a higher level of W concentration (2%W prepared by mechanofusion) was used (note that this sample's performance is marginally lower than 1%W_Mech). The comparison between pristine and cycled states of 2%W_Mech from the Ni atoms environment perspective in Figure 3-8(a) reveals minimal shifts toward lower energy after cycling, which could be due to only very

minor changes in the amount of reduced Ni as a result of cycling. This behavior could be driven by a combination of factors, including slightly more oxygen loss, the onset of phase transformations to cubic phases, and other degradation processes during the cycling.

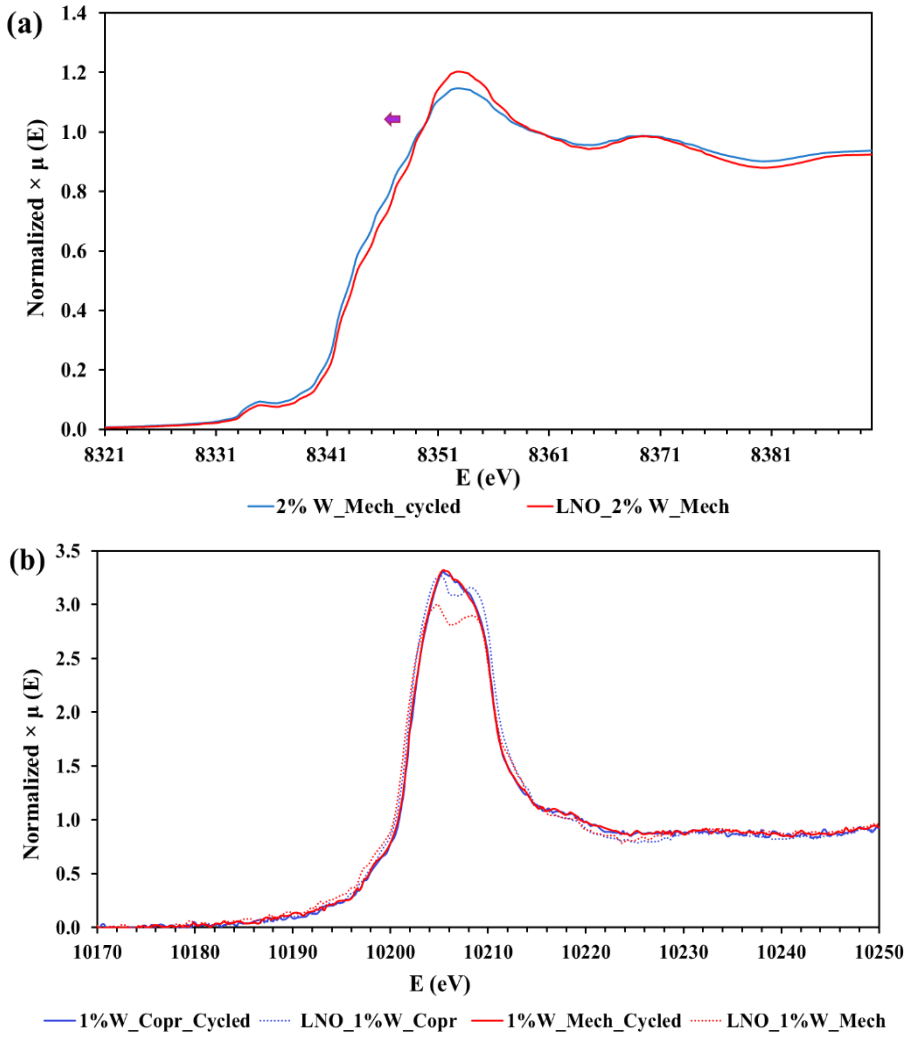

Figure 3-8 (a) The normalized μ (E) comparison of the Ni absorption edge between the 2%W_Mech samples before and after cycling. (b) the comparison of XANES features of the W absorption edge for 1%W_Mech and 1%W_Copr samples in their pristine (with a double peak shape) and cycled states (with more combined peak shape). All the spectra are acquired from the fluorescence mode.

On the other hand, the W L-edge XANES, Figure 3-8(b), only sensitive to the local environment of W atoms, shows that the double peak shape present in the pristine state of the W-enriched materials evolves to a single broader peak in the cycled samples. This change clearly indicates that the W environment is changed. Due to the well-defined distribution of W at the surfaces and inside the grain boundaries, this change could be due to multiple contributions caused by the interaction between the electrolyte and W-compounds. Since our previous investigation on the W L-edge in the pristine samples was not successful in identifying unambiguously the origins of the double-peak structure [30], the reaction with the electrolyte and the presence of F and P reacting with W makes the identification of the changes even more complex.

3.4 Conclusions

The effects of electrochemical cycling on the structure of tungsten-enriched $LiNiO_2$ were investigated with high-resolution photon- and electron-based techniques. Two different sets of samples prepared through two enrichment approaches, namely mechanofusion and coprecipitation, were investigated. In this study, 1%W LNO prepared by mechanofusion showed the best cycling behavior due to a more packed particle structure and the presence of W on the very surface and inside grain boundaries of their secondary particles. This W-rich layer on the surface of the secondary particles appeared to significantly reduce particle degradation from interacting with the electrolyte. In addition, the presence of W-phases located at the grain boundaries between the primary particles in 1%W prepared by mechanofusion, could partially accommodate the cycling stress and reduce the risk of crack initiation and growth. The 1%W samples prepared by coprecipitation, where the sample synthesis conditions generated a high level of porosities, showed a lower resistance to degradation, as evidenced by massive phase transformations detected through electron

energy loss near-edge structures. The porous structure enabled increased penetration of the electrolyte through the cathode structure. In the samples prepared by the coprecipitation process, W was found deeper within the grain boundaries of secondary particles, which should expectedly help reduce the cycling stress due to lattice volume change. However, the W presence in the samples prepared by coprecipitation was ineffective in protecting the primary particle's surface from side reactions with the electrolyte due to the enhanced penetration of the electrolyte through the more porous structure. Overall, due to these porosities generated in our synthesis process, the materials prepared by coprecipitation showed greater structural degradation than the ones prepared by mechanofusion. This result emphasizes the importance of synthesis optimization in designing high performance materials. Based on the comparison of the samples, further tailoring of the mechanofusion protocols and coprecipitation could lead to an increased amount of W within grain boundaries, strengthening the mechanical integrity of the particles, reducing the porosities, and optimizing the thickness of the protective layer on the surface.

3.5 Supplementary information

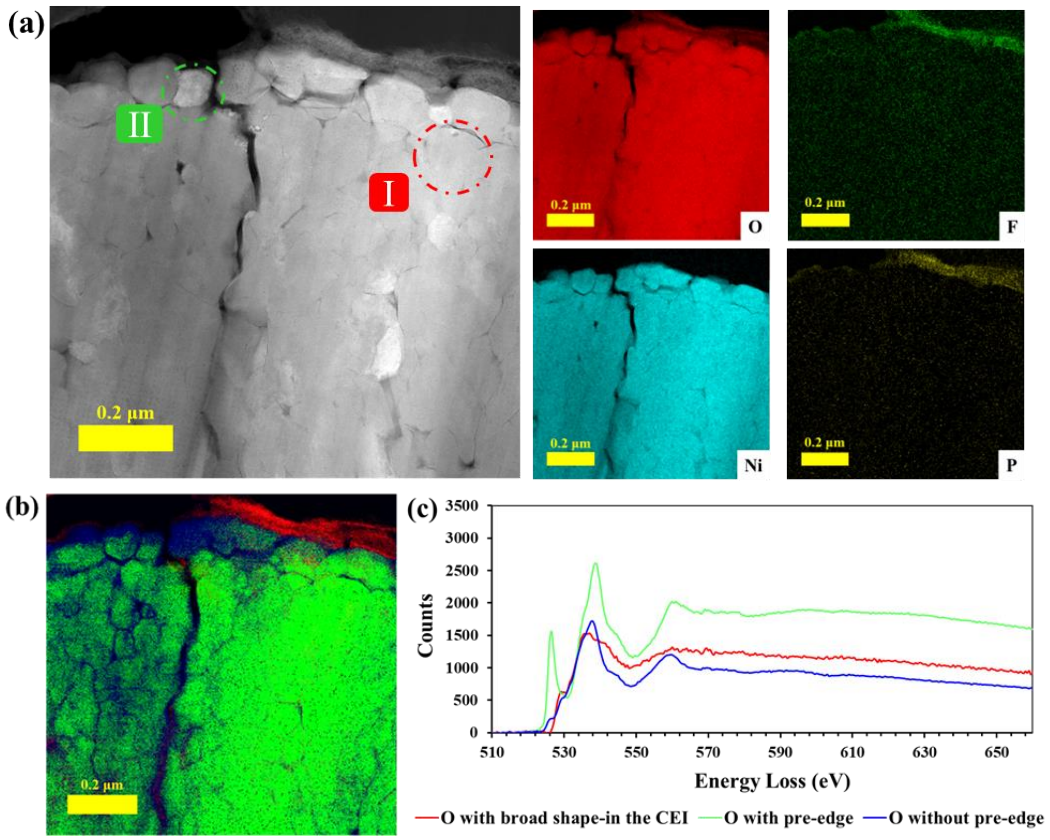

Figure 3-9S (a) The annular dark field (ADF) image and EELS maps show the elemental distribution inside 1%W_Mech_Cycled' secondary particle containing cracks. (b) The Red Green Blue (RGB) image is based on the different shapes of O K-edge peaks in (c), for the 1%W_Mech_Cycled sample. (c) illustrates three different shapes of O K-edge peak, with a broad shape inside the CEI layer, in red, without a pre-edge peak in blue, and with a pre-edge peak in green.

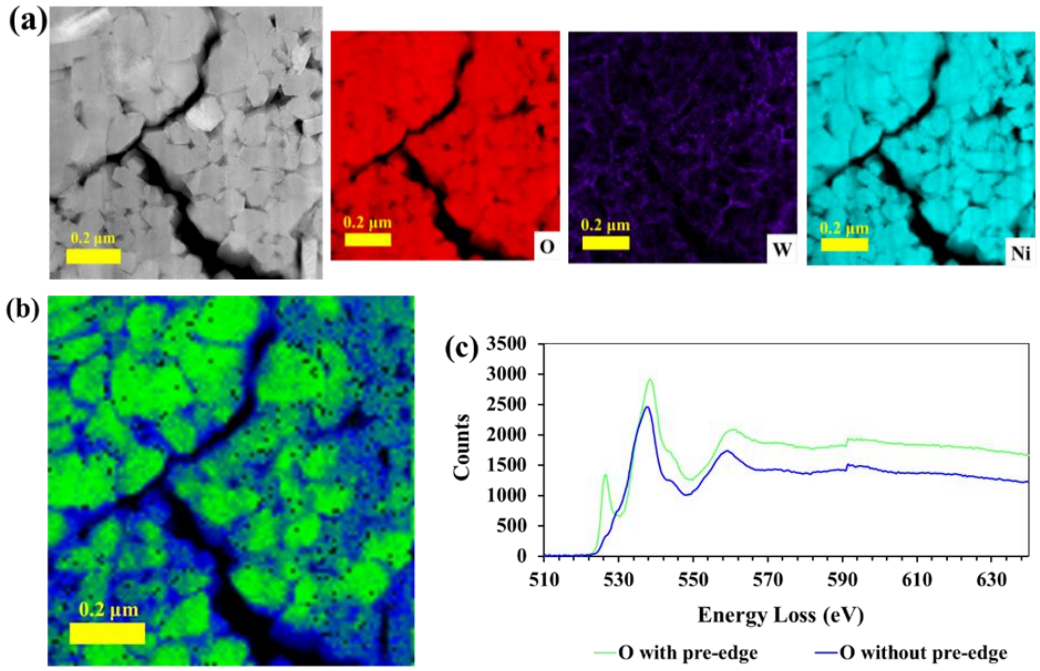

Figure 3-10S (a) The ADF image and EELS maps illustrate the elemental distribution from the inner side of 1%W_Copr_Cycled' secondary particle. In this inner part, the F K-edge peak is too weak, and the P K-edge peak is not clear from the W M-edge peak; therefore, they are not presented here. (b) The RGB image is based on the different shapes of the O K-edge peaks in (c), for the 1%W_Copr_Cycled sample. (c) shows two shapes of O K-edge peak, with and without a pre-edge peak in green and blue, respectively.

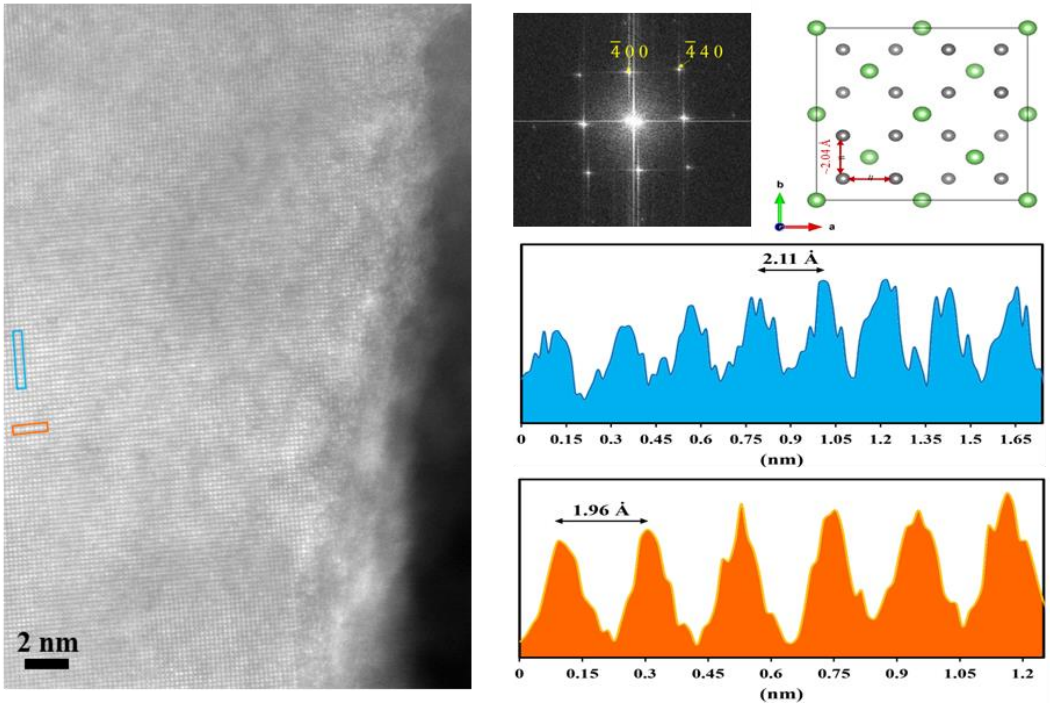

Figure 3-11S The high-resolution High Angle Annular Dark Field (HAADF) image from the right side of the primary particle near a porosity gap (its exact location is shown in Figure 3-6(d)), from 1%W_Copr_Cycled's secondary particle. The spots in the calculated FT image are indexed based on the spinel structure with <001> zone axis. The {220} reflections are not detected in the FT image as discussed more in section 3.3.4. The same zone axis orientation from the crystal cell view with Ni and Li atoms in gray and green, respectively. Two intensity profiles are extracted from the high-resolution HAADF image regarding the orange and blue boxes marked in the picture.

3.6 References

[1] L. Zou, W. Zhao, H. Jia, J. Zheng, L. Li, D.P. Abraham, G. Chen, J.R. Croy, J.-G. Zhang, C. Wang, The Role of Secondary Particle Structures in Surface Phase Transitions of Ni-Rich Cathodes, Chem. Mater. 32 (2020) 2884–2892. https://doi.org/10.1021/acs.chemmater.9b04938.

[2] L. Lu, X. Han, J. Li, J. Hua, M. Ouyang, A review on the key issues for lithium-ion battery management in electric vehicles, J. Power Sources. 226 (2013) 272–288. https://doi.org/10.1016/j.jpowsour.2012.10.060.

[3] J.L.D. Xuebing Han, Minggao Ouyang*, Languang Lu, A comparative study of commercial lithium ion battery cycle life in electric vehicle: Capacity loss estimation, J. Power Sources. 268 (2014) 658–669.

[4] C. Hendricks, N. Williard, S. Mathew, M. Pecht, A failure modes, mechanisms, and effects analysis (FMMEA) of lithium-ion batteries, J. Power Sources. 297 (2015) 113–120. https://doi.org/10.1016/j.jpowsour.2015.07.100.

[5] K.G. Gallagher, S.H. Kang, S.U. Park, S.Y. Han, XLi2MnO3·(1 - X)LiMO2 blended with LiFePO4 to achieve high energy density and pulse power capability, J. Power Sources. 196 (2011) 9702–9707. https://doi.org/10.1016/j.jpowsour.2011.07.054.

[6] J.B. Goodenough, Y. Kim, Challenges for rechargeable Li batteries, Chem. Mater. 22 (2010) 587–603. https://doi.org/10.1021/cm901452z.

[7] M. Okubo, S. Ko, D. Dwibedi, A. Yamada, Designing positive electrodes with high energy density for lithium-ion batteries, J. Mater. Chem. A. 9 (2021) 7407–7421. https://doi.org/10.1039/d0ta10252k.

[8] J. Danet, T. Brousse, K. Rasim, D. Guyomard, P. Moreau, Valence electron energy-loss spectroscopy of silicon negative electrodes for lithium batteries, Phys. Chem. Chem. Phys. 12 (2010) 220–226. https://doi.org/10.1039/b915245h.

[9] J. Li, A. Manthiram, A Comprehensive Analysis of the Interphasial and Structural Evolution over Long-Term Cycling of Ultrahigh-Nickel Cathodes in Lithium-Ion

Batteries, Adv. Energy Mater. 9 (2019) 1–14. https://doi.org/10.1002/aenm.201902731.

[10] W. Li, E.M. Erickson, A. Manthiram, High-nickel layered oxide cathodes for lithium-based automotive batteries, Nat. Energy. 5 (2020) 26–34. https://doi.org/10.1038/s41560-019-0513-0.

[11] W. Liu, P. Oh, X. Liu, M.J. Lee, W. Cho, S. Chae, Y. Kim, J. Cho, Nickel-Rich Layered Lithium Transition-Metal Oxide for High-Energy Lithium-Ion Batteries, Angew. Chemie - Int. Ed. 54 (2015) 4440–4457. https://doi.org/10.1002/anie.201409262.

[12] P. Teichert, G.G. Eshetu, H. Jahnke, E. Figgemeier, Degradation and aging routes of ni-rich cathode based li-ion batteries, Batteries. 6 (2020) 1–26. https://doi.org/10.3390/batteries6010008.

[13] A.O. Kondrakov, A. Schmidt, J. Xu, H. Geßwein, R. Mönig, P. Hartmann, H. Sommer, T. Brezesinski, J. Janek, Anisotropic Lattice Strain and Mechanical Degradation of High- and Low-Nickel NCM Cathode Materials for Li-Ion Batteries, J. Phys. Chem. C. 121 (2017) 3286–3294. https://doi.org/10.1021/acs.jpcc.6b12885.

[14] E.M. Erickson, F. Schipper, T.R. Penki, J.-Y. Shin, C. Erk, F.-F. Chesneau, B. Markovsky, D. Aurbach, Review—Recent Advances and Remaining Challenges for Lithium Ion Battery Cathodes, J. Electrochem. Soc. 164 (2017) A6341–A6348. https://doi.org/10.1149/2.0461701jes.

[15] J. Liu, J. Wang, Y. Ni, K. Zhang, F. Cheng, J. Chen, Recent breakthroughs and perspectives of high-energy layered oxide cathode materials for lithium ion batteries, Mater. Today. 43 (2021) 132–165. https://doi.org/10.1016/j.mattod.2020.10.028.

[16] Y. Bi, J. Tao, Y. Wu, L. Li, Y. Xu, E. Hu, B. Wu, J. Hu, C. Wang, J.G. Zhang, Y. Qi, J. Xiao, Reversible planar gliding and microcracking in a single-crystalline Ni-rich cathode, Science (80-.). 370 (2020) 1313–1318. https://doi.org/10.1126/science.abc3167.

[17] W. Zhu, X. Huang, T. Liu, Z. Xie, Y. Wang, K. Tian, L. Bu, H. Wang, L. Gao, J. Zhao, Ultrathin Al2O3 coating on LiNi0.8Co0.1Mn0.1O2 cathode material for enhanced cycleability at extended voltage ranges, Coatings. 9 (2019) 1–12. https://doi.org/10.3390/COATINGS9020092.

[18] N. Zhang, N. Zaker, H. Li, A. Liu, J. Inglis, L. Jing, J. Li, Y. Li, G.A. Botton, J.R. Dahn, Cobalt-Free Nickel-Rich Positive Electrode Materials with a Core-Shell Structure, Chem. Mater. 31 (2019) 10150–10160. https://doi.org/10.1021/acs.chemmater.9b03515.

[19] F. Schipper, M. Dixit, D. Kovacheva, M. Talianker, O. Haik, J. Grinblat, E.M. Erickson, C. Ghanty, D.T. Major, B. Markovsky, D. Aurbach, Stabilizing nickel-rich layered cathode materials by a high-charge cation doping strategy: Zirconium-doped LiNi0.6Co0.2Mn0.2O2, J. Mater. Chem. A. 4 (2016) 16073–16084. https://doi.org/10.1039/c6ta06740a.

[20] O. Breuer, A. Chakraborty, J. Liu, T. Kravchuk, L. Burstein, J. Grinblat, Y. Kauffman, A. Gladkih, P. Nayak, M. Tsubery, A.I. Frenkel, M. Talianker, D.T. Major, B. Markovsky, D. Aurbach, Understanding the Role of Minor Molybdenum Doping in LiNi0.5Co0.2Mn0.3O2 Electrodes: From Structural and Surface Analyses and Theoretical Modeling to Practical Electrochemical Cells, ACS Appl. Mater. Interfaces. 10 (2018) 29608–29621. https://doi.org/10.1021/acsami.8b09795.

[21] H. Li, P. Zhou, F. Liu, H. Li, F. Cheng, J. Chen, Stabilizing nickel-rich layered oxide cathodes by magnesium doping for rechargeable lithium-ion batteries, Chem. Sci. 10 (2019) 1374–1379. https://doi.org/10.1039/c8sc03385d.

[22] T. Li, X.-Z. Yuan, L. Zhang, D. Song, K. Shi, C. Bock, Degradation Mechanisms and Mitigation Strategies of Nickel-Rich NMC-Based Lithium-Ion Batteries, Springer Singapore, 2019. https://doi.org/10.1007/s41918-019-00053-3.

[23] G.T. Park, H.H. Ryu, N.Y. Park, C.S. Yoon, Y.K. Sun, Tungsten doping for stabilization of Li[Ni0.90Co0.05Mn0.05]O2 cathode for Li-ion battery at high voltage, J. Power Sources. 442 (2019) 227242. https://doi.org/10.1016/j.jpowsour.2019.227242.

[24] U.H. Kim, N.Y. Park, G.T. Park, H. Kim, C.S. Yoon, Y.K. Sun, High-Energy W-Doped Li[Ni0.95Co0.04Al0.01]O2 Cathodes for Next-Generation Electric Vehicles, Energy Storage Mater. 33 (2020) 399–407. https://doi.org/10.1016/j.ensm.2020.08.013.

[25] U.H. Kim, D.W. Jun, K.J. Park, Q. Zhang, P. Kaghazchi, D. Aurbach, D.T. Major, G. Goobes, M. Dixit, N. Leifer, C.M. Wang, P. Yan, D. Ahn, K.H. Kim, C.S. Yoon, Y.K. Sun, Pushing the limit of layered transition metal oxide cathodes for high-energy density rechargeable Li ion batteries, Energy Environ. Sci. 11 (2018) 1271–1279. https://doi.org/10.1039/c8ee00227d.

[26] H.H. Ryu, G.T. Park, C.S. Yoon, Y.K. Sun, Suppressing detrimental phase transitions via tungsten doping of LiNiO2 cathode for next-generation lithium-ion batteries, J. Mater. Chem. A. 7 (2019) 18580–18588. https://doi.org/10.1039/c9ta06402h.

[27] D. Rathore, C. Geng, N. Zaker, I. Hamam, Y. Liu, P. Xiao, G.A. Botton, J. Dahn, C. Yang, Tungsten Infused Grain Boundaries Enabling Universal Performance Enhancement of Co-Free Ni-Rich Cathode Materials, J. Electrochem. Soc. 168 (2021) 120514. https://doi.org/10.1149/1945-7111/ac3c26.

[28] C. Geng, D. Rathore, D. Heino, N. Zhang, I. Hamam, N. Zaker, G.A. Botton, R. Omessi, N. Phattharasupakun, T. Bond, C. Yang, J.R. Dahn, Mechanism of Action of the Tungsten Dopant in LiNiO 2 Positive Electrode Materials, Adv. Energy Mater. 12 (2022) 2103067. https://doi.org/10.1002/aenm.202103067.

[29] I. Hamam, R. Omessi, D. Rathore, C. Geng, R. Cooke, K. Plucknett, D.P. Bishop, N. Zaker, G.A. Botton, C. Yang, J.R. Dahn, Correlating the mechanical strength of positive electrode material particles to their capacity retention, Cell Reports Phys. Sci. 3 (2022) 100714. https://doi.org/10.1016/j.xcrp.2021.100714.

[30] N. Zaker, C. Geng, D. Rathore, I. Hamam, N. Chen, P. Xiao, Probing the Mysterious Behavior of Tungsten as a Dopant Inside Pristine Cobalt-Free Nickel-Rich Cathode Materials, Submitt. to Adv. Funct. Mater. (n.d.) 1–33.

[31] A. van Bommel, J.R. Dahn, Analysis of the Growth Mechanism of Coprecipitated

Spherical and Dense Nickel, Manganese, and Cobalt-Containing Hydroxides in the Presence of Aqueous Ammonia, Chem. Mater. 21 (2009) 1500–1503. https://doi.org/10.1021/cm803144d.

[32] V. Petkov, Pair Distribution Functions Analysis, Charact. Mater. (2012) 1361–1372. https://doi.org/10.1002/0471266965.com159.

[33] J.J. Matteo Bianchini, François Fauth, Pascal Hartmann, Torsten Brezesinski, An in situ structural study on the synthesis and decomposition of LiNiO2, J. Mater. Chem. A. (2020) 121. https://doi.org/10.1039/C9TA12073D.Volume.

[34] L. de Biasi, A. Schiele, M. Roca-Ayats, G. Garcia, T. Brezesinski, P. Hartmann, J. Janek, Phase Transformation Behavior and Stability of LiNiO2 Cathode Material for Li-Ion Batteries Obtained from In Situ Gas Analysis and Operando X-Ray Diffraction, ChemSusChem. 12 (2019) 2240–2250. https://doi.org/10.1002/cssc.201900032.

[35] Q. Lin, W. Guan, J. Zhou, J. Meng, W. Huang, T. Chen, Q. Gao, X. Wei, Y. Zeng, J. Li, Z. Zhang, Ni–Li anti-site defect induced intragranular cracking in Ni-rich layer-structured cathode, Nano Energy. 76 (2020) 105021. https://doi.org/10.1016/j.nanoen.2020.105021.

[36] A. Mukhopadhyay, B.W. Sheldon, Deformation and stress in electrode materials for Li-ion batteries, Prog. Mater. Sci. 63 (2014) 58–116. https://doi.org/10.1016/j.pmatsci.2014.02.001.

[37] Y. Zhu, C. Wang, Strain accommodation and potential hysteresis of LiFePO4 cathodes during lithium ion insertion/extraction, J. Power Sources. 196 (2011) 1442–1448. https://doi.org/10.1016/j.jpowsour.2010.08.008.

[38] S. Kalluri, H. Cha, J. Kim, H. Lee, H. Jang, J. Cho, Building High-Rate Nickel-Rich Cathodes by Self-Organization of Structurally Stable Macrovoid, Adv. Sci. 1902844 (2020) 1–9. https://doi.org/10.1002/advs.201902844.

[39] X. He, J. Wang, R. Kloepsch, S. Krueger, H. Jia, H. Liu, B. Vortmann, J. Li, Enhanced electrochemical performance in lithium ion batteries of a hollow spherical lithium-rich cathode material synthesized by a molten salt method, Nano

Res. 7 (2014) 110–118. https://doi.org/10.1007/s12274-013-0378-7.

[40] V. Pimenta, M. Sathiya, D. Batuk, A.M. Abakumov, D. Giaume, S. Cassaignon, D. Larcher, J.M. Tarascon, Synthesis of Li-Rich NMC: A Comprehensive Study, Chem. Mater. 29 (2017) 9923–9936. https://doi.org/10.1021/acs.chemmater.7b03230.

[41] S. Hwang, D.H. Kim, K.Y. Chung, W. Chang, Understanding local degradation of cycled Ni-rich cathode materials at high operating temperature for Li-ion batteries, Appl. Phys. Lett. 105 (2014). https://doi.org/10.1063/1.4895336.

Chapter 4

Exploring the Effect of Surface Modification on the Coated Nickel-Rich Cathode Materials Structures

Complete Citation:

Zaker, N., Geng, C., Pofelski, A., Dahn, J.R., Botton, G.A.

Acknowledgments

The McMaster authors are grateful for a Discovery Grant supported by the Natural Sciences and Engineering Research Council (NSERC) as well as the Canadian Centre for Electron Microscopy (CCEM), where all the electron microscopy work was performed and is funded by McMaster University, the Canada Foundation for Innovation, and NSERC. The Dalhousie authors are thankful for the financial support of Tesla Canada, the Alliance grant, and NSERC, which facilitated their contribution to the coating process and measurement of cycling performance.

Abstract

$LiNi_{0.8}Co_{0.15}Al_{0.05}O_2$ (NCA) precursors coated with different amounts of Al_2O_3 and $LiFePO_4$ (LFP) through a mechanofusion process are examined with various electron-based characterization methods. The investigation provides insight into the coating structure and uniformity at the microscopic level. The LFP- and Al_2O_3- on NCA-coated structures show the presence of physical intermixing between the NCA and coating layers, which would lead to changes in their transport characteristic features and affect their final electrochemical behavior. With scanning diffraction mapping, we identify nanocrystalline regions on the surface of bare NCA used as a reference material to understand the effect of the mechanofusion coating process. The results show that the mechanofusion process is an effective means of coating NCA particles, although with some damage generated on the surface of coated material and non-uniformities and physical intermixing of the coated particles.

Keywords:

Mechanofusion; Coating; Ni-rich cathode; $LiFePO_4$; Al_2O_3; 4D-STEM.

4.1 Introduction

$LiNi_xCo_yAl_{1-x-y}O_2$ (NCA) cathode material, with a low amount of electrochemical inactive aluminum ions and a more robust layered structure, shows good cyclic performance and is one of the promising layered structured positive electrodes to be used in electric vehicles [1–4]. Among the NCA family of compounds, the most common chemistry that is widely commercialized is $LiNi_{0.8}Co_{0.15}Al_{0.05}O_2$. This material, however, rapidly loses its capacity, especially at higher temperatures and wider operating voltage windows [5,6]. Since most of the cycling degradation in the cathode is triggered on the surface of particles [7–9], surface modification of the solid/liquid interface between the cathode and electrolyte through coating and core-shell structure would be beneficial [10–17]. The main role of coatings is to provide a barrier layer between the electrolyte and active materials at the surface of the Ni-rich cathode's particles. This protective layer would mitigate, or at least delay, the parasitic reactions, surface corrosion caused by HF, cation mixing, transition-metal ions' dissolution, and oxygen release. Nevertheless, since most of the coatings are electrically insulating materials, they lead to lower capacity rates and suffer from microcracking, noticeable in ultra-high Ni cathode materials [13–15,18–20]. Mechanofusion is one of the dry coating methods which exhibits some practical advantages, namely the scaling up capacity to fulfill industrial demands, the environmental benefits due to lack of liquid waste, and the economical nature of the process [10,21–23]. Due to the presence of high levels of applied centrifugal, shear, and compression forces during this coating process, the host or core precursors are coated by other small particles [10,23]. Herein, two different coating materials, alumina (Al_2O_3) and $LiFePO_4$ (LFP), have been applied on the NCA's secondary particles' surface. Among the oxide coating, alumina is one of the most common candidates due to its low cost, strong resistance against acidic

and alkaline attacks, high hardness, and straightforward synthesis [24–26]. On the other hand, LFP has been used due to its low material cost, being environmentally friendly, and having strong covalency bonds between metal ions and the PO_4 polyanion in addition to phosphorus and oxygen double bond, which make them better withstand side reactions [27,28]. Although many investigations have shown improvements in the cycling performance of the coated particles [24,29–31], we focus here on the structural characterization of NCA subjected to the mechanofusion process alone and NCA coated with alumina and LFP through mechanofusion in order to understand the factors that affect the performance of these materials in light of their cycling behavior. To better understand the quality of the coatings and the structural effect of the mechanofusion method on the coating and the core particles, different electron-based characterization techniques have been utilized.

4.2 Experimental procedures

4.2.1 coating process

In this paper, all the used precursors are commercial particles. To start the coating process, 50 g of $LiNi_{0.8}Co_{0.15}Al_{0.05}O_2$ (NCA, powders were purchased from Umicore and Ecopro, Korea) along with different amounts of either Al_2O_3 nanoparticles (with 0.25, 0.5, 1 g from Sigma-Aldrich with particle size <50 nm) or $LiFePO_4$ (with 1, 2, 4, and 5 g purchased from Pulead, China), were loaded inside the rotating bowl of an in-house mechanofusion machine, to reach different weighing percent coatings (leading to NCA+0.5%Al_2O_3, NCA+1%Al_2O_3, and NCA+2%Al_2O_3, respectively). The spinning speed was set to 3600 rpm for 60 minutes. More details regarding this process were published in the author's previous work [21]. To better visualize the effect of mechanofusion on the NCA, the whole

same process was done on 50 g of NCA particles alone. For the sake of brevity, instead of writing coated NCA with different weighing percentages of LFP and alumina, "NCA+wt% of coated material" will be mentioned, for instance, "NCA+2%LFP". The reference NCA before and after the mechanofusion process are named NCA and NCA Fusion, respectively.

4.2.2 Electrochemical measurements

The coated particles were combined with polyvinylidene difluoride (PVDF) and carbon black to reach a 92:4:4 weight ratio, and then all were mixed with N-methyl-2-pyrrolidone (NMP, 99.5%) to obtain a slurry. The slurry was applied on aluminum foil (with 150 μm thickness), dried out (for 3 h inside an oven at 120 °C), and then calendared (under 2000 atm pressure). After that, final electrodes with a 12.75 mm diameter size were punched and dried overnight (16 h) under vacuum. Assembling coin cells was done inside an argon glovebox, containing cathode electrode from previous steps, as well as Li metal, two Celgard #2300 layers, and 1.2 M $LiPF_6$ in FEC (fluoroethylene carbonate)/DMC (dimethyl carbonate) with volume ration of 1:4, as the anode electrode, separator, and electrolyte, correspondingly. An E-one Moli Energy Canada battery test system was utilized to cycle the prepared coin cells between 3.0 and 4.3 V vs. Li^+/Li at 30 °C. For the two first and last cycles, C/20 and C/50 rates were set, respectively. The rest 50 cycles in between had a C/5 rate.

4.2.3 Electron microscopy characterization

All the characterized particles were in their pristine states (i.e., not electrochemically cycled). Scanning electron microscopy (SEM) was used to image and map the distribution of elements in the cross-section samples. Cross-sections of powders were prepared by

embedding a paste (a mixture of carbon paste, propanol, and powder samples) inside a tiny notch of a graphite block. After that, powders within the graphite block were polished with an Ar ion beam with an ion beam cross-section polisher (JEOL IB09010CP). SEM imaging and energy dispersive X-ray spectrometry (EDS) mapping were obtained with a Magellan 400 SEM. To prepare lamellae for transmission electron microscopy (TEM), two plasma/focused ion beam (P/FIB) instruments, a Helios G4 PFIB, and a Zeiss NVision 40 FIB were utilized. TEM analysis along with energy dispersive X-ray spectrometry (EDX) were carried out using either a JEOL 2010F or a ThermoFisher Scientific Talos 200X, both of which were operated at 200kV. For electron energy loss spectroscopy (EELS), experiments were conducted with a JEOL 2010F TEM fitted with a Gatan Tridiem Imaging filter using a convergence and collection semi-angles set to 10 and 30 mrad, respectively. To obtain 4-dimensional scanning transmission electron microscopy (4D-STEM) data (i.e., a full diffraction pattern at every pixel or a 2D rastered area), an FEI Titan 80-300 Cubed equipped with double-aberration correctors was used and operated at 200 kV. Diffraction patterns were acquired with a Gatan US1000 CCD camera synchronized with the Gatan STEM acquisition module.

4.3 Results and discussions

4.3.1 SEM cross-section and EDS

To assess the uniformity of the coatings on the cathode material, high-resolution SEM images, as well as EDS mapping, were used. With increasing content of LFP in the mixture during mechanofusion, the overall trend is that coated areas become thicker (Figure 4-1(a-i,ii)), but detailed mapping over large fields of view shows that these coatings are not completely uniform, as demonstrated by EDS maps in Figure 4-1(b). The maps show that

Fe and P (the elements corresponding to the coating) are on the edge of the surface (the shell area). Based on the SEM images obtained at higher magnification, good physical contact can be observed between NCA and coating materials (Figure 4-1(a-i,ii)). For LFP-coated NCA materials, with lower coating content, at 2% mixture of LFP in NCA, the coating layers are thin, but areas with Fe and P could be detected by the EDS line scans (Figure 4-5S). Therefore, more investigation was required by TEM and EDX mapping on the thin lamellae to better visualize the interface between the coating and core structure.

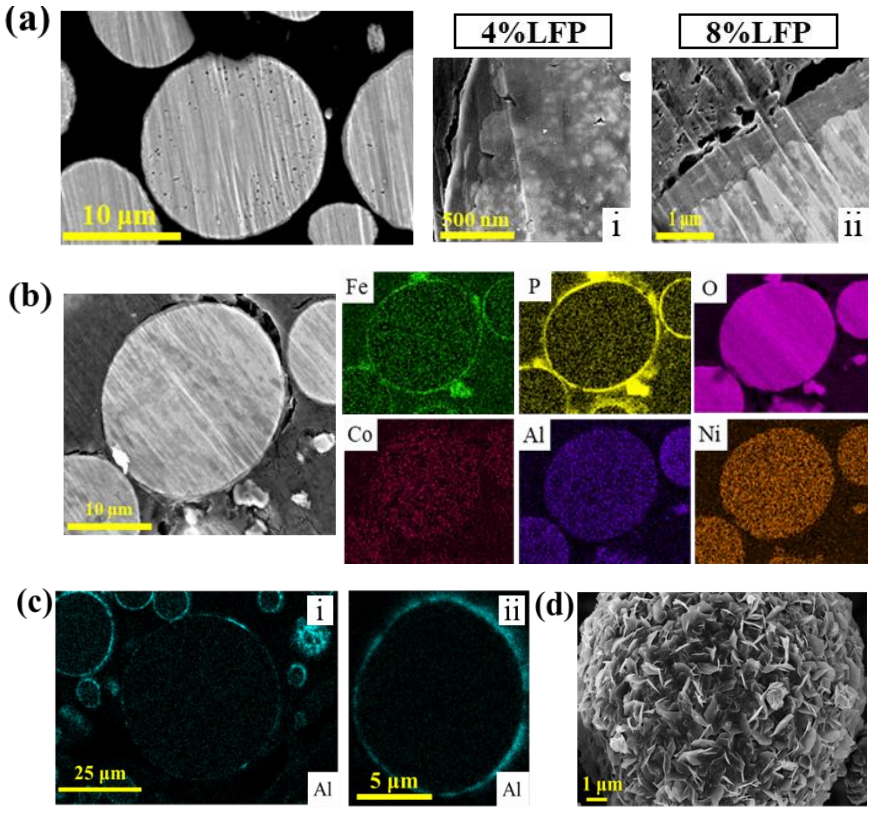

Figure 4-1 (a) SEM cross-section images from NCA+4%LFP in low and high magnification "i" (from backscatter electron and secondary electron, respectively) as well as high mag SEM image from the coating part of NCA+8%LFP "ii" (from secondary electron). (b) SEM and EDS mapping images from NCA+8%LFP. (c) and (d) show the EDS mappings of Al and higher magnification SEM image from the surface morphology of NCA+2%Al_2O_3, respectively.

For the Al_2O_3 coated cathode, a higher concentration of coating material during mechanofusion, Figure 4-1(c), results in a more entirely covered NCA and higher Al levels on the very surface, especially on the small and medium size particles, Figure 4-1(c-ii). These results show that even for very hard materials, such as alumina, coating by mechanofusion is an effective process. However, the higher resolution SEM image from the coated surface of NCA+2%Al_2O_3 (Figure 4-1(d)) illustrates that the morphology of the coated alumina is not smooth, and flake-shaped alumina particles are attached to the surface.

4.3.2 S/TEM and analytical electron microscopy (EDX and EELS)

To better analyze the effect of mechanofusion on the structures of coating and core particles, selected area diffraction patterns (SADPs) were acquired. For the 4%LFP coating on NCA, diffraction patterns from two selected areas (Figure 4-2(a)) are consistent with highly crystalline structures that were indexed with <011> and <$10\bar{1}0$> zone axes of orthorhombic LFP with Cmcm space group and hexagonal NCA with R$\bar{3}$m space group, respectively. Based on these observations, it appears that over a relatively large scale (more than ~50nm thickness), the crystal structure of the precursor phases does not change significantly. At a finer scale, however, a more detailed analysis is shown further below. Additional analysis with STEM and EDX mapping, Figure 4-2(b), reveals that, in NCA+2%LFP, some level of physical intermixing/folding between the coating and NCA materials (which might be separated and rejoin on the surface) can occur on the top surface. This can be visualized from the presence of Ni regions above the Fe-P-rich areas (Figure 4-2(b)). This effect would occur due to the fracture of small NCA particles off the secondary NCA precursors' surface and the subsequent mechanical bonding of these small fragments on top of the LFP during mechanofusion. This top surface intermixing could

affect the electrochemical behavior of these materials since these two materials (NCA and LFP) are different in conductivity and mechanical properties.

In the case of alumina used as a nanoscale powder, as can be seen in Figure 4-2(c), the selected area diffraction pattern of the shell region, is a spotty and relatively diffuse ring pattern with lattice spacings that are consistent with alumina corundum-type trigonal crystal with R -3 c H space group. One set of reflections (the (110) planes) is missing, which is likely due to the orientation of the fine grains. Because of the very small grain size and likely high level of strain induced by the mechanofusion process, the reflections are not perfectly fitting over the relaxed structure rings. Furthermore, the bright-field STEM image in Figure 4-2(c) illustrates the presence of flake-shape alumina (shown in the SEM images) attached on the surface of the NCA secondary particle and an Al layer just below the flakes, which are consistent with the Al maps obtained with EDS (Figure 4-2(d)).

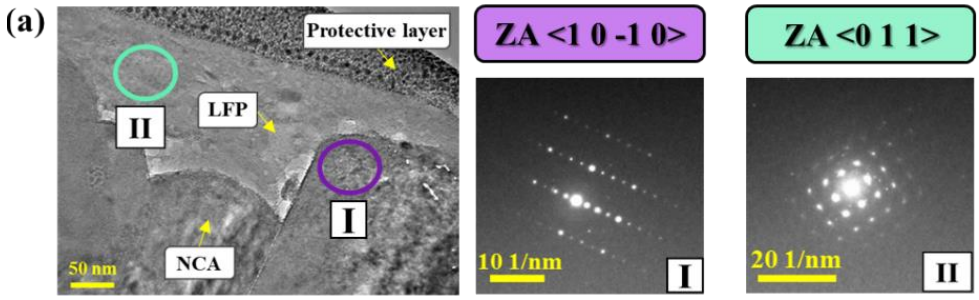

Figure 4-2 (a) TEM image and Selected Area Diffraction (SAD) patterns from coating and core part of NCA+4%LFP, as well as their zone axis directions. (b) STEM image from a High-Angle Annular Dark Field (HAADF) detector, and EDX maps illustrate the mixture of LFP and NCA on the very surface of NCA+2%LFP. (c) STEM Bright Field (BF) image of NCA+2%Al_2O_3 and the DP from the coated area indexing based on the alumina, corundum-type trigonal crystal (without a visible ring for (110) diffraction). The green arrows illustrate the presence of alumina flakes in the TEM lamellae. (d) EDX maps for Ni and Al.

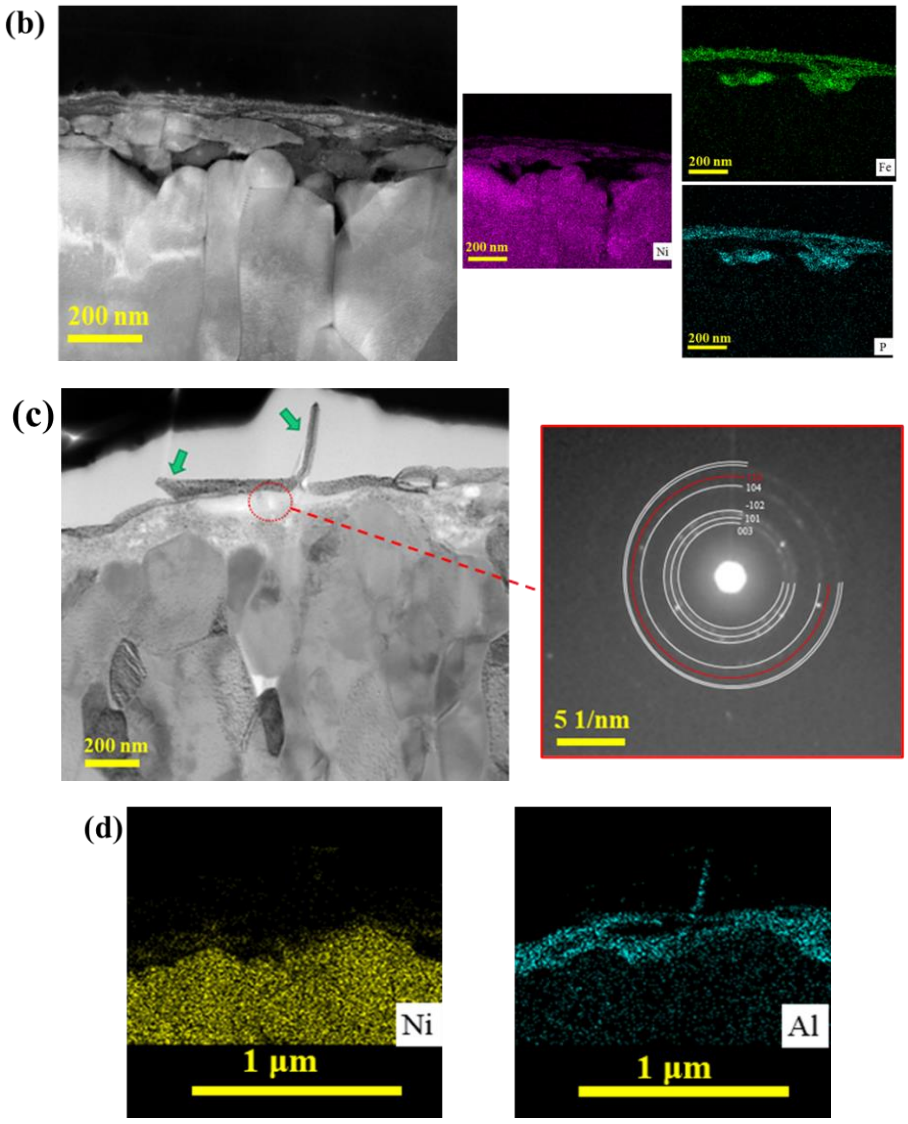

Figure 4-2 Continued.

The physical intermixing visible in the LFP-coated NCA (Figure 4-2(b)) is also demonstrated, here with EELS, in the alumina-coated material (Figure 4-3). Further investigation regarding alumina coating shows that at some locations, EELS can detect the mixing between the alumina and primary particles of NCA on the very surface. Given the presence of Al within the NCA, it is impossible to detect whether there is any chemical interdiffusion of the alumina within the NCA. However, due to the very high melting point

and hardness of alumina, we do not expect to see any interdiffusion between these two materials.

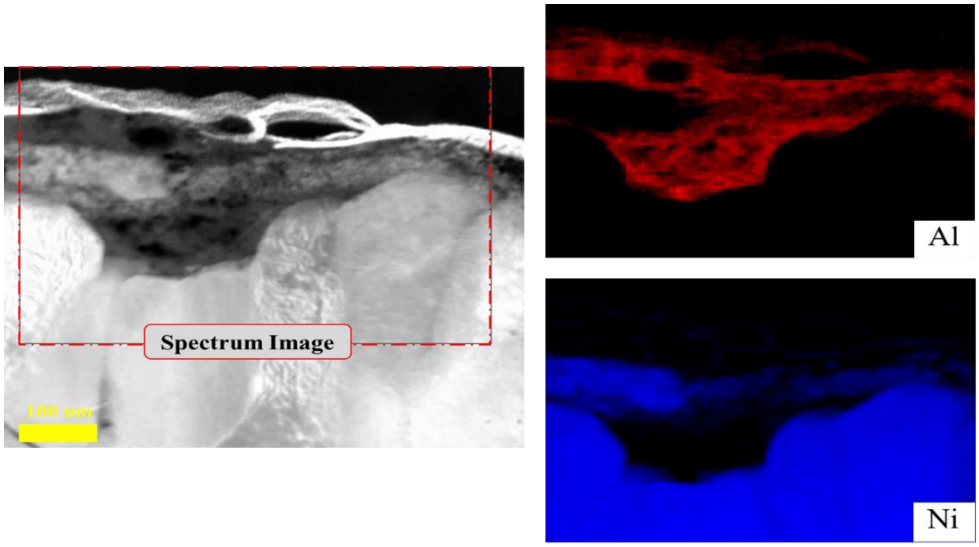

Figure 4-3 STEM image from NCA+2%Al_2O_3 and EELS maps of Al and Ni illustrate the presence of some level of mixing on the top surface of NCA.

Electrochemical cycling experiments of LFP coated materials (Figure 4-6S(a)), regardless of the LFP level (2% and 10%) investigated in this work, demonstrated marginal differences from each other and significant degradation compared to bare NCA subjected to mechanofusion, used as a reference sample from the same processing conditions. The nanoscale structure observed in our work, with the evidence of physical intermixing between NCA and LFP particles, might be the cause for this loss of capacity in LFP-coated NCA particles. However, in the case of alumina-coated material, Figure 4-6S(b), by increasing the amount of coating from 0.5% to 1% alumina, the specific discharge capacity increases. On the other hand, by increasing the amount of alumina to 2%, a decrease in capacity occurs. This suggests that there is an optimal level of coating, whether this is related to uniformity or thickness, to cover the secondary particles' surface. As we illustrated above, the reduction could be induced by a thicker alumina coating on the

surface of NCA particles, which would reduce the conductivity due to the insulating nature of Al_2O_3.

4.3.3 4D-STEM and strain measurement

In order to understand the reduction of capacity in the NCA material resulting from the mechanofusion process alone (Figure 4-6S), detailed structural investigations on bare NCA particles following mechanofusion were carried out. For this work, the 4D-STEM technique was used in order to visualize local diffraction patterns over a large field of view. In this technique, for each pixel of a STEM image, a convergent beam electron diffraction (CBED) pattern is captured [32]. This would enable the extraction of local strain measurements with respect to a reference area by measuring the position of diffraction spots. Based on the diffraction patterns extracted from different fields of view shown in Figure 4-4, it is possible to visualize that the mechanofusion process induces a highly defective/nanocrystalline area at the very surface of the secondary particles, as shown by the diffused and circular shape diffraction patterns (based on the patterns extracted from areas I and II). Just below approximately 80 nm from the surface of secondary particles, the patterns are consistent with a single crystalline grain, such as shown in area III, suggesting that the mechanofusion process appears to induce damage within the few 100's nm of the surface and the areas further away from the surface are either unaffected or partially recrystallized. Within the crystalline areas, the patterns exhibit small fluctuations in the intensities and position of the diffraction spots, which could be caused by the presence of defects in the structure [33], such as dislocations induced by the mechanofusion process. From the changes in the position of diffraction spots in single crystal-like patterns, it is possible to deduce local strain. However, due to the high defect density, the strain calculation was not successful, with strong variance in its parameters. Therefore, the

precession method would be required to enhance the quality of the diffraction patterns and generate more kinematical conditions on the average patterns.

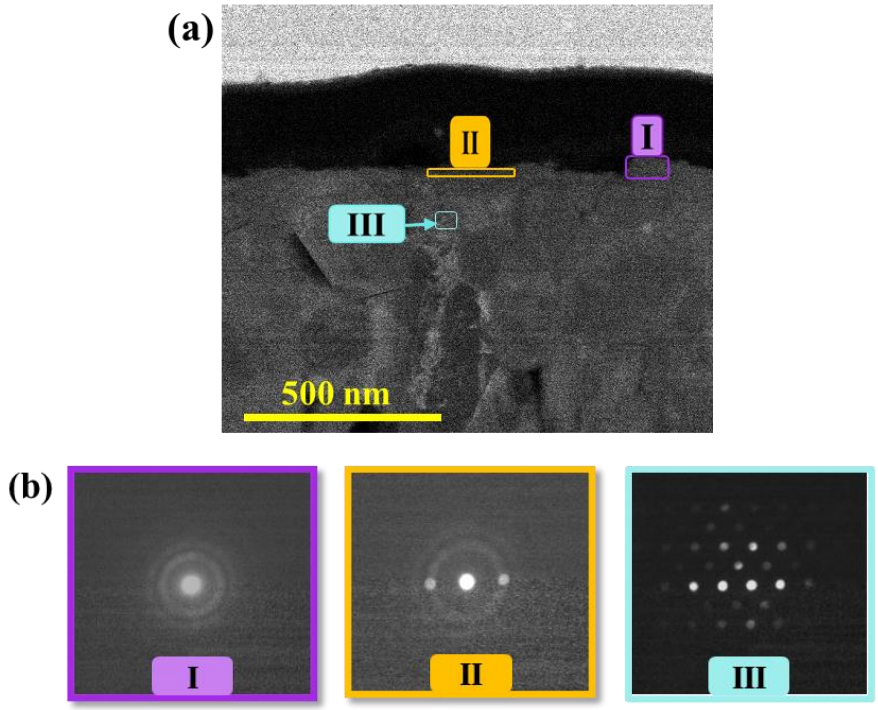

Figure 4-4 Diffraction analysis of areas affected by the mechanofusion process applied on the bare NCA particles. (a) STEM image, including some selected areas I to III, and (b) shows their respective extracted average CBED patterns. Areas I and II show circular patterns, and III contains a single crystalline-like pattern.

4.4 Conclusion

The morphology of NCA cathode materials coated with $LiFePO_4$ and Al_2O_3 using the mechanofusion process was investigated through different electron microscopy analysis techniques. For both LFP and Al_2O_3, the mechanofusion process was effective in producing coatings with good intimate contact with the NCA secondary particles. The observations over large areas, however, demonstrated that the coatings were not uniform in thickness and, at the detailed level, physical intermixing/folding between the coating material and substrate was present. The intermixing was expected to result in changes in transport properties, thus adversely affecting the electrochemical performance of the coated materials. Using a nanoscale diffraction imaging method known as 4D-STEM analysis, our work showed that the mechanofusion process caused the formation of a nanocrystalline and defective areas near the top surface of the secondary particles, negatively affecting the electrochemical cycling performance of the base NCA material, compared to pristine NCA. Overall, given the performance degradation of the mechanofused NCA, different processing conditions would need to be developed to ensure that the electrochemical properties of the coated materials reflect the presence of the coating rather than processing conditions generating high levels of defects in the material.

4.5 Supplementary information

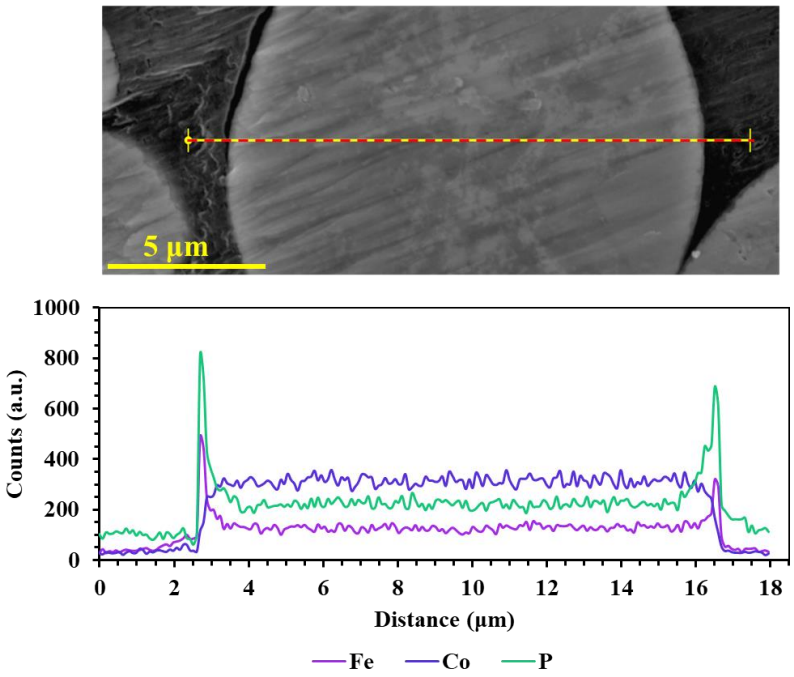

Figure 4-5S The SEM image and EDS line scan profile show the concentration of Fe and P on the shell region.

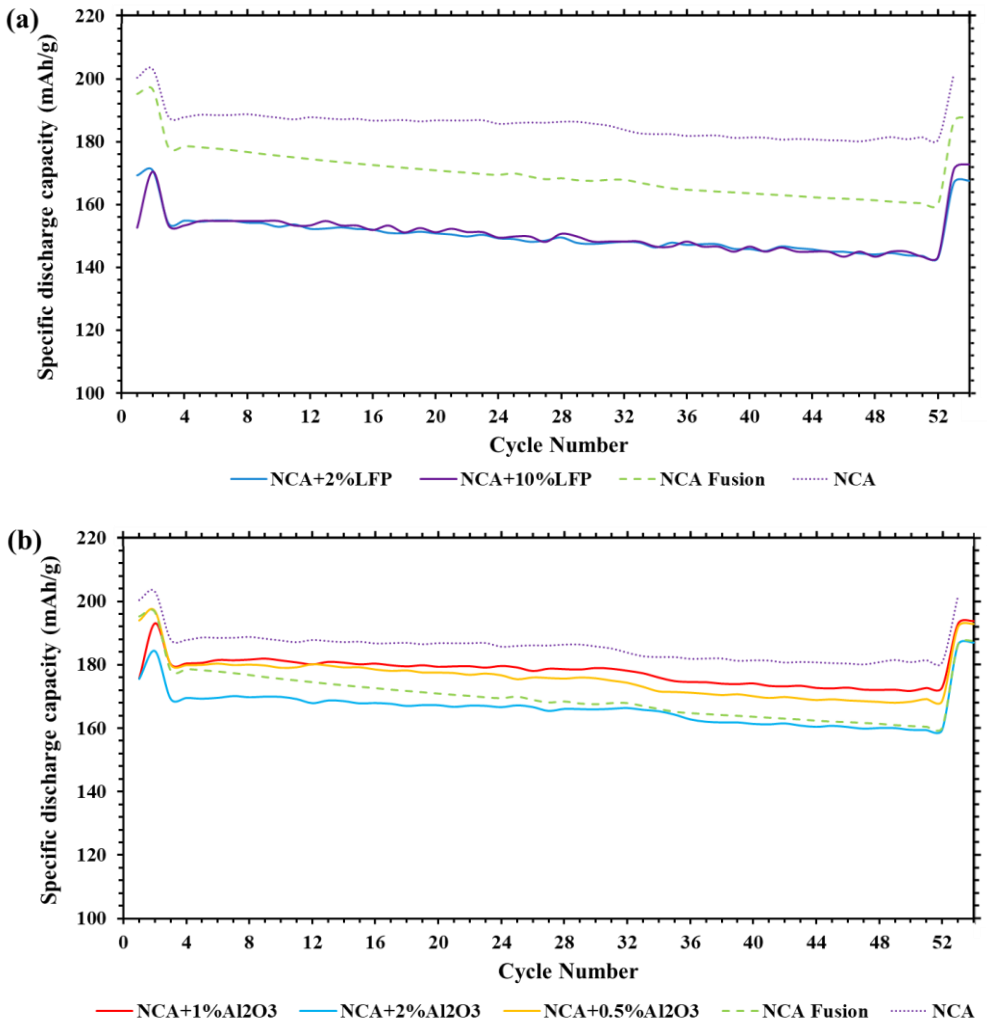

Figure 4-6S (a) and (b) show the cyclic behaviors of NCA before (NCA) and after mechanofusion (NCA Fusion), along with NCA coated with the lowest and highest amount of LFP, and NCA coated with different amounts of alumina, respectively.

4.6 References

[1] S. Hwang, D.H. Kim, K.Y. Chung, W. Chang, Understanding local degradation of cycled Ni-rich cathode materials at high operating temperature for Li-ion batteries, Appl. Phys. Lett. 105 (2014). https://doi.org/10.1063/1.4895336.

[2] M.D. Radin, S. Hy, M. Sina, C. Fang, H. Liu, J. Vinckeviciute, M. Zhang, M.S. Whittingham, Y.S. Meng, A. Van der Ven, Narrowing the Gap between Theoretical and Practical Capacities in Li-Ion Layered Oxide Cathode Materials, Adv. Energy Mater. 7 (2017) 1–33. https://doi.org/10.1002/aenm.201602888.

[3] A. Manthiram, A reflection on lithium-ion battery cathode chemistry, Nat. Commun. 11 (2020) 1–9. https://doi.org/10.1038/s41467-020-15355-0.

[4] C.H. Chen, J. Liu, M.E. Stoll, G. Henriksen, D.R. Vissers, K. Amine, Aluminum-doped lithium nickel cobalt oxide electrodes for high-power lithium-ion batteries, J. Power Sources. 128 (2004) 278–285. https://doi.org/10.1016/j.jpowsour.2003.10.009.

[5] K. Kleiner, J. Melke, M. Merz, P. Jakes, P. Nagel, S. Schuppler, V. Liebau, H. Ehrenberg, Unraveling the Degradation Process of LiNi 0.8 Co 0.15 Al 0.05 O 2 Electrodes in Commercial Lithium Ion Batteries by Electronic Structure Investigations, ACS Appl. Mater. Interfaces. 7 (2015) 19589–19600. https://doi.org/10.1021/acsami.5b03191.

[6] S. Watanabe, M. Kinoshita, K. Nakura, Capacity fade of LiNi(1-x-y)CoxAlyO 2 cathode for lithium-ion batteries during accelerated calendar and cycle life test. I. Comparison analysis between LiNi(1-x-y)Co xAlyO2 and LiCoO2 cathodes in cylindrical lithium-ion cells during long term storage test, J. Power Sources. 247 (2014) 412–422. https://doi.org/10.1016/j.jpowsour.2013.08.079.

[7] F. Lin, I.M. Markus, D. Nordlund, T.C. Weng, M.D. Asta, H.L. Xin, M.M. Doeff, Surface reconstruction and chemical evolution of stoichiometric layered cathode materials for lithium-ion batteries, Nat. Commun. 5 (2014) 3529. https://doi.org/10.1038/ncomms4529.

[8] H.H. Ryu, K.J. Park, C.S. Yoon, Y.K. Sun, Capacity fading of ni-rich

li[NixCoyMn1-x-y]O2 ($0.6 \leq x \leq 0.95$) Cathodes for High-Energy-Density Lithium-Ion Batteries: Bulk or Surface Degradation?, Chem. Mater. 30 (2018) 1155–1163. https://doi.org/10.1021/acs.chemmater.7b05269.

[9] P. Oh, S.M. Oh, W. Li, S. Myeong, J. Cho, A. Manthiram, High-Performance Heterostructured Cathodes for Lithium-Ion Batteries with a Ni-Rich Layered Oxide Core and a Li-Rich Layered Oxide Shell, Adv. Sci. 3 (2016) 1–8. https://doi.org/10.1002/advs.201600184.

[10] L. Zheng, C. Wei, M.D.L. Garayt, J. MacInnis, M.N. Obrovac, Spherically Smooth Cathode Particles by Mechanofusion Processing, J. Electrochem. Soc. 166 (2019) A2924–A2927. https://doi.org/10.1149/2.0681913jes.

[11] K.Y. Park, Y. Zhu, C.G. Torres-Castanedo, H.J. Jung, N.S. Luu, O. Kahvecioglu, Y. Yoo, J.W.T. Seo, J.R. Downing, H.D. Lim, M.J. Bedzyk, C. Wolverton, M.C. Hersam, Elucidating and Mitigating High-Voltage Degradation Cascades in Cobalt-Free LiNiO2 Lithium-Ion Battery Cathodes, Adv. Mater. 34 (2022) 1–11. https://doi.org/10.1002/adma.202106402.

[12] W. Li, E.M. Erickson, A. Manthiram, High-nickel layered oxide cathodes for lithium-based automotive batteries, Nat. Energy. 5 (2020) 26–34. https://doi.org/10.1038/s41560-019-0513-0.

[13] H.H. Sun, H.H. Ryu, U.H. Kim, J.A. Weeks, A. Heller, Y.K. Sun, C.B. Mullins, Beyond Doping and Coating: Prospective Strategies for Stable High-Capacity Layered Ni-Rich Cathodes, ACS Energy Lett. 5 (2020) 1136–1146. https://doi.org/10.1021/acsenergylett.0c00191.

[14] P. Teichert, G.G. Eshetu, H. Jahnke, E. Figgemeier, Degradation and aging routes of ni-rich cathode based li-ion batteries, Batteries. 6 (2020) 1–26. https://doi.org/10.3390/batteries6010008.

[15] A. Chakraborty, S. Kunnikuruvan, S. Kumar, B. Markovsky, D. Aurbach, M. Dixit, D.T. Major, Layered Cathode Materials for Lithium-Ion Batteries: Review of Computational Studies on LiNi1- x- yCoxMnyO2 and LiNi1- x- yCoxAlyO2, Chem. Mater. 32 (2020) 915–952. https://doi.org/10.1021/acs.chemmater.9b04066.

[16] A. Konarov, S.T. Myung, Y.K. Sun, Cathode materials for future electric vehicles and energy storage systems, ACS Energy Lett. 2 (2017) 703–708. https://doi.org/10.1021/acsenergylett.7b00130.

[17] N. Zhang, N. Zaker, H. Li, A. Liu, J. Inglis, L. Jing, J. Li, Y. Li, G.A. Botton, J.R. Dahn, Cobalt-Free Nickel-Rich Positive Electrode Materials with a Core–Shell Structure, Chem. Mater. 31 (2019) 10150–10160. https://doi.org/10.1021/acs.chemmater.9b03515.

[18] N.D. Phillip, B.L. Armstrong, C. Daniel, G.M. Veith, Role of Surface Acidity in the Surface Stabilization of the High-Voltage Cathode LiNi0.6Mn0.2Co0.2O2, ACS Omega. 5 (2020) 14968–14975. https://doi.org/10.1021/acsomega.0c00458.

[19] F. Schipper, E.M. Erickson, C. Erk, J.-Y. Shin, F.F. Chesneau, D. Aurbach, Review—Recent Advances and Remaining Challenges for Lithium Ion Battery Cathodes, J. Electrochem. Soc. 164 (2017) A6220–A6228. https://doi.org/10.1149/2.0351701jes.

[20] K. Du, H. Xie, G. Hu, Z. Peng, Y. Cao, F. Yu, Enhancing the Thermal and Upper Voltage Performance of Ni-Rich Cathode Material by a Homogeneous and Facile Coating Method: Spray-Drying Coating with Nano-Al2O3, ACS Appl. Mater. Interfaces. 8 (2016) 17713–17720. https://doi.org/10.1021/acsami.6b05629.

[21] C. Geng, S. Trussler, M. Johnson, N. Zaker, B. Scott, G. Botton, J.R. Dahn, A low-cost instrument for dry particle fusion coating of advanced electrode material particles at the laboratory scale., J. Electrochem. Soc. (2020). https://doi.org/10.1149/1945-7111/aba00e.

[22] W. Chen, R.N. Dave, R. Pfeffer, O. Walton, Numerical simulation of Mechanofusion system, Powder Technol. 146 (2004) 121–136. https://doi.org/10.1016/j.powtec.2004.07.014.

[23] L. Zheng, T.D. Hatchard, M.N. Obrovac, A high-quality mechanofusion coating for enhancing lithium-ion battery cathode material performance, MRS Commun. 9 (2019) 245–250. https://doi.org/10.1557/mrc.2018.209.

[24] W. Zhu, X. Huang, T. Liu, Z. Xie, Y. Wang, K. Tian, L. Bu, H. Wang, L. Gao, J.

Zhao, Ultrathin Al2O3 coating on LiNi0.8Co0.1Mn0.1O2 cathode material for enhanced cycleability at extended voltage ranges, Coatings. 9 (2019) 1–12. https://doi.org/10.3390/COATINGS9020092.

[25] G. Kaur, B.D. Gates, J.E. Soc, Review — Surface Coatings for Cathodes in Lithium Ion Batteries : From Crystal Structures to Electrochemical Performance Review — Surface Coatings for Cathodes in Lithium Ion Batteries : From Crystal Structures to Electrochemical Performance, (2022). https://doi.org/10.1149/1945-7111/ac60f3.

[26] X. Tan, M. Zhang, J. Li, D. Zhang, Y. Yan, Z. Li, Recent progress in coatings and methods of Ni-rich LiNi0.8Co0.1Mn0.1O2 cathode materials: A short review, Ceram. Int. (2020). https://doi.org/10.1016/j.ceramint.2020.06.091.

[27] X. Liu, H. Li, E. Yoo, M. Ishida, H. Zhou, Fabrication of FePO 4 layer coated LiNi 1/3Co 1/3Mn 1/3O 2: Towards high-performance cathode materials for lithium ion batteries, Electrochim. Acta. 83 (2012) 253–258. https://doi.org/10.1016/j.electacta.2012.07.111.

[28] M.M. Doeff, Encyclopedia of Sustainability Science and Technology, 2012. https://doi.org/10.1007/978-1-4419-0851-3.

[29] Y. Wei, C. Zhou, D. Zhao, G. Wang, Enhanced electrochemical performance and safety of LiNi0.8Co0.15Al0.05O2 by LiFePO4 modification, Chem. Phys. Lett. 751 (2020). https://doi.org/10.1016/j.cplett.2020.137480.

[30] B. Seteni, N. Rapulenyane, J.C. Ngila, S. Mpelane, H. Luo, Coating effect of LiFePO4 and Al2O3 on Li1.2Mn0.54Ni0.13Co0.13O2 cathode surface for lithium ion batteries, J. Power Sources. 353 (2017) 210–220. https://doi.org/10.1016/j.jpowsour.2017.04.008.

[31] J. Chen, L. Zhu, D. Jia, X. Jiang, Y. Wu, Q. Hao, X. Xia, Y. Ouyang, L. Peng, W. Tang, T. Liu, LiNi0.8Co0.15Al0.05O2 cathodes exhibiting improved capacity retention and thermal stability due to a lithium iron phosphate coating, Electrochim. Acta. 312 (2019) 179–187. https://doi.org/10.1016/j.electacta.2019.04.153.

[32] S.E. Zeltmann, A. Müller, K.C. Bustillo, B. Savitzky, L. Hughes, A.M. Minor, C.

Ophus, Patterned probes for high precision 4D-STEM bragg measurements, Ultramicroscopy. 209 (2020). https://doi.org/10.1016/j.ultramic.2019.112890.

[33] D. Viladot, M. Véron, M. Gemmi, F. Peiró, J. Portillo, S. Estradé, J. Mendoza, N. Llorca-Isern, S. Nicolopoulos, Orientation and phase mapping in the transmission electron microscope using precession-assisted diffraction spot recognition: State-of-the-art results, J. Microsc. 252 (2013) 23–34. https://doi.org/10.1111/jmi.12065.

Chapter 5

Conclusions and future works

5.1 Conclusions

In this research, the effect of two main modification methods to reach complex cathode Ni-rich structures has been thoroughly investigated. The results of studying core-shell structures have been addressed elsewhere in the published paper (as a co-author through our collaboration). In this sandwich thesis, the effect of introducing a dopant in the LNO host structure, its electrochemical behavior, and failure analysis has been investigated comprehensively. Additionally, the impact of surface modification through a solid-state coating method (via mechanofusion) has been analyzed in more detail. In the following main conclusions regarding this comprehensive research are listed:

- By adding a high valence cation dopant, W, inside the LNO host structure, heterogeneous distribution of W-rich regions has been obtained. W concentrated mostly on the top surface as well as in between grain boundaries of the LNO's secondary particles. The presence of two W variants $Li_{4+x}Ni_{1-x}WO_6$ (x=0 and 0.1) and the possibility of $Li_xW_yO_z$ compounds have been found through high-resolution electron- and photon-based analysis. W-rich compounds, which have been shown to be in an amorphous state generated from likely melting and

diffusion through the grain boundaries, along with crystalline W-rich nanometer-scale sized regions near the grain boundaries, would be kinetically stabilized (in the case of W-rich compounds containing Ni). Therefore, the W mostly reinforces the grain boundaries rather than being distributed in the whole bulk structure.

- It has been shown that tungsten-enriched $LiNiO_2$, with only 1%W, demonstrated the best electrochemical behavior among other W-doped and tested materials in this study. The main strength points of this complex structure were the presence of a W-rich layer on its top surface which effectively protected the core structure of LNO not only from direct contact with the electrolyte during cycling but also from the synthesis conditions using high temperatures. Furthermore, the presence of tungsten-rich regions in the grain boundaries helped to protect the structure from crack initiation by damping part of the cycling-induced mechanical stress.

  - The effect of structural degradation in the cathode can be probed through electron energy loss near-edge structures. It is worth noting that, regardless of using different methods for structural modification, the synthesis process should be optimized and able to produce well-packed structures. Otherwise, a porous structure enables the infiltration of the electrolyte into the core of cathode particles and causes degradation by affecting active materials as well as reducing the structural integrity. Therefore, in order to obtain the best results from W-enrichment materials, further modifications would be required to not only reinforce the grain boundaries and generate a protective layer on the surface of the particles but also reduce the interconnected porosities in the host structures.

  - Coating via mechanofusion is one of the potential methods that could be easily scalable for industrial production, and it would be beneficial to characterize

its effects on the coating and core materials. Through nanoscale diffraction (using the so-called 4D-STEM analysis), evidence of nanocrystalline areas and structural defects have been detected within regions near approximately a few 100's nm from the particle surface. It has been shown that in this solid-state process, despite reaching a good physical attachment between coating and core particles, the non-uniform thickness of coatings and physical intermixing between the core and coating precursors would negatively affect the electrochemical behavior of final coated cathodes. Therefore, more tailoring would be essential in refining processing parameters to fulfill industrial desired results and reach defect-free materials as much as possible.

5.2 Future works

Regardless of the significant amount of research on developing higher energy density materials in the LIB field, still more efforts would be required to reach desirable metrics for higher energy and power, longer-term and safer use of these batteries, especially in electric vehicles. Besides some research on introducing new materials, it is more effective and realistic to work on improving those materials that are already produced in the industrial lines.

In the case of using more complex structures like doped materials, more development in modeling and using DFT calculations would be helpful to predict the final structure more efficiently and optimize the synthesis parameters.

In all the cathode research, doing in-situ or partial operando analysis, either inside an electron microscope or in synchrotron beamlines, would bring more detailed information

regarding the actual electrochemical behavior of the whole cell in more realistic environments.

To increase the precision in strain measurement through the 4D-STEM technique inside a TEM, using the precession method would be helpful to reduce dynamic diffraction conditions leading to a higher quality of diffraction patterns.

Appendix I

6.1 4D-STEM analysis

Based on the 4D-STEM analysis in chapter 4, some level of changes in spacing between the diffracted spots along with pattern rotation have been detected even by the naked eye through searching in the 2D STEM data. The detailed analysis required adapting the py4DSTEM Python code toolkit [1]. To better recognize the acquired DPs, manual identification was added to the original code to select the most visible diffraction spots for strain calculation. Since our sample has multiple grains and their DPs were not always in a good zone axis, some noise levels are present in the 4D-STEM acquired data (area identified as "Spectrum Image" in Figure 6-1(a)). The reference area is marked with a red rectangle in Figure 6-1(a). It is worth mentioning that since the top layers in the spectrum image had circular DPs consistent with nanocrystalline areas, the measurements only include region I in Figure 6-1(a) for the detailed strain map. Based on the calculated mean and sensitivity (standard deviation) of strain and rotation parameters in the reference area, listed in Table 6-1, the reality of having some level of residual strain inside the particle after mechanofusion is approved. However, since the selected area was too small, a very high variance without a reasonable trend from top to bottom was acquired. The calculated strain maps are shown in Figure 6-1(b) based on the mentioned reference area and the g reference vector calculated from g_1+g_2, which are marked in I area's DP inside Figure 6-1(a).

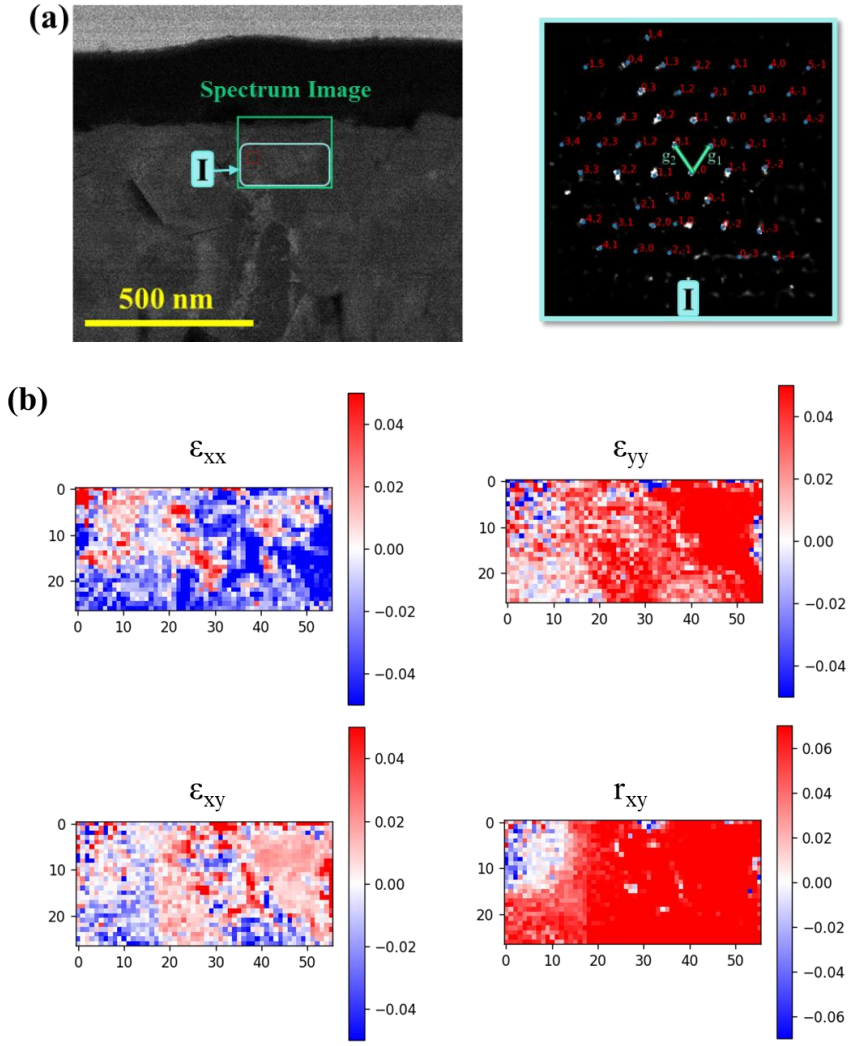

Figure 6-1 (a) STEM image including the location of whole acquired spectrum in green box and "I" selected area with its average diffraction patterns. This diffraction pattern extracted from py4DSTEM code which is indexed based on the two selected vectors g_1 and g_2. (b) illustrates strain maps from the marked I area, based on the reference area, shown by red rectangle in STEM image and the g reference vector equal to g_1+g_2.

Table 6-1 List of calculations regarding the amount of strain and rotation parameters' mean and sensitivity based on the selected reference area in Figure 6-1.

Strain parameter	Mean	Sensitivity (Standard Deviation)
ε_{xx}	0.0028	0.0117
ε_{yy}	-0.0036	0.0209
ε_{xy}	0.00165	0.0098
r_{xy} [rad]	-0.00138	0.0073

6.2 Reference

[1] B.H. Savitzky, L.A. Hughes, S.E. Zeltmann, H.G. Brown, S. Zhao, P.M. Pelz, E.S. Barnard, J. Donohue, L.R. DaCosta, T.C. Pekin, E. Kennedy, M.T. Janish, M.M. Schneider, P. Herring, C. Gopal, A. Anapolsky, P. Ercius, M. Scott, J. Ciston, A.M. Minor, C. Ophus, py4DSTEM: a software package for multimodal analysis of four-dimensional scanning transmission electron microscopy datasets, (2020) 1–32. http://arxiv.org/abs/2003.09523.